DIPLOMARBEIT

Entwicklung eines lasergeführten Messgeräts für große Oberflächen

zur Erlangung des akademischen Grades

Diplom-Ingenieur

im Rahmen des Studiums

Physikalische Energie- und Messtechnik

eingereicht von

Heinz-Georg Stangl

Matrikelnummer 01225334

ausgeführt am Atominstitut
der Fakultät für Physik der Technischen Universität Wien

Betreuung:
Univ.Prof. Dipl.-Phys. Dr.rer.nat. **Hartmut Abele**
Univ.Ass. Mag.rer.nat. Dr.techn. **René Sedmik**

Wien, 11.10.2021

Unterschrift Verfasser

Unterschrift Betreuer

Die approbierte gedruckte Originalversion dieser Diplomarbeit ist an der TU Wien Bibliothek verfügbar
The approved original version of this thesis is available in print at TU Wien Bibliothek.
TU Bibliothek Your knowledge hub WIEN

TECHNISCHE
UNIVERSITÄT
WIEN
Vienna University of Technology

ATOMINSTITUT

DIPLOMARBEIT

Development of a laser-guided large scale surface metrology device

Author:
Heinz-Georg Stangl, BSc

Supervisors:
Hartmut Abele, Univ.Prof. Dipl.-Phys. Dr.rer.nat.

René Sedmik, Univ.Ass. Mag.rer.nat. Dr.techn.

October 11, 2021

Die approbierte gedruckte Originalversion dieser Diplomarbeit ist an der TU Wien Bibliothek verfügbar
The approved original version of this thesis is available in print at TU Wien Bibliothek.
TU Bibliothek Your knowledge hub WIEN

Abstract

The force of gravity is one of the four fundamental interactions in physics. Gravity is part of general relativity, while the remainder (electromagnetism and weak and strong nuclear force) are described by the Standard Model of particle physics. A multitude of hypotheses attempt to reconcile these two distinct models, but remain unproven so far. Meanwhile, indications of the existence of dark matter and dark energy also warrant further investigation. One popular approach for extending the Standard Model is to introduce small modifications to Newtonian gravity at different scales.

In the quest of examining Newton's law from microscopic to cosmological distances, the *q*BOUNCE experiment is in a unique position to observe interactions at the micrometer scale using the novel concept of gravity resonance spectroscopy. In the Ramsey-like setup, state transitions of the probe particles are induced by mechanically vibrating sections of the flight path. Neutrons are used as probe particles due to their vanishingly small electrical charge and low electric susceptibility. In particular, ultra-cold neutrons (UCNs) are used, which undergo total reflection at any angle due to their low kinetic energy, thus "bouncing" through the experimental setup. When exposed to the earth's gravity potential, the UCNs form bound energy states as they pass over the five mirror stages. The eigen energies of the quantum bouncers on the vertical scale are determined by the Fermi potential of the mirror and the linear gravity potential. It is thus critical for the accuracy of the experiment to establish reliable mirror control so as to avoid unwanted state transitions. As such it is necessary to align the edges of the mirrors to each other to minimize vertical gaps and obtain surface maps of the mirrors in order to further improve measurement accuracy.

The main objective of this work is to build and characterize a prototype measurement solution that is capable of resolving mirror surface geometry with nanometer precision. This entails the problem of establishing a stable reference for use as coordinate zero. Existing designs have used a mechanical surface as reference, which results in duplication of any surface defects the reference may have during the measurement process. With the desire to further increase sensitivity of the *q*BOUNCE experiment, the existing solution cannot keep up in terms of accuracy.

The proposed new surface measurement system uses a laser-based position hold system so as to provide a physically perfect reference plane. Using a basic version of this technique in a prototype, an accuracy of 192 nm RMS is reached, with the next iterations of this system aiming to improve this figure to below 10 nm.

In order to increase the performance of the prototype system, external disturbances like seismic and electronic noise, temperature effects and properties of the signal-processing setup are characterized in detail.

As a demonstration, surface elevation maps of a mirror are recorded with two different interferometric measurement devices. In another test, a fiber interferometer is shown as an effective means of calibrating the steps between the mirror stages.

Finally, these characterizations are used to make recommendations for the upcoming iteration of the surface measurement appliance.

Die approbierte gedruckte Originalversion dieser Diplomarbeit ist an der TU Wien Bibliothek verfügbar
The approved original version of this thesis is available in print at TU Wien Bibliothek.
TU Bibliothek Your knowledge hub WIEN

Kurzfassung

Die Gravitationskraft ist eine der vier fundamentalen Wechselwirkungen der Physik. Gravitation ist Teil der allgemeinen Relativitätstheorie, während die verbleibenden (Elektromagnetismus und die schwache und starke Wechselwirkung) vom Standardmodell der Teilchenphysik beschrieben werden. Eine Vielzahl an Hypothesen versuchen (bisher erfolglos) diese zwei verschiedenen Modelle miteinander ein Einklang zu bringen. Währenddessen rechtfertigen Hinweise auf die Existenz von dunkler Materie und dunkler Energie weitere Untersuchungen. Verbreitet ist die Herangehensweise, das Standardmodell durch kleine Modifikationen der Newton'schen Gravitation auf verschiedenen Skalen zu erweitern.

Im Bestreben, Newton's Gesetz auf mikroskopischen bis kosmischen Abständen zu erforschen, ist das qBOUNCE-Experiment in der Lage, Interaktionen im Mikrometer-Bereich mit dem neuartigen Verfahren der Gravitationsresonanzspektroskopie zu beobachten. In dem Ramsey-ähnlichen Aufbau werden Zustandsänderungen der Testteilchen durch mechanische Vibration von Teilen der Flugstrecke induziert. Wegen ihrer verschwindend geringen elektrischen Ladung und niedrigen elektrischen Polarisierbarkeit werden Neutronen als Testteilchen verwendet, im Speziellen ultrakalte Neutronen (UCNs). Diese werden aufgrund ihrer niedrigen kinetischen Energie unter jedem Einfallswinkel total reflektiert, hüpfen also durch das Experiment. Dabei bilden die "quantum bouncers" gebundene Energiezustände, die entlang der vertikalen Achse durch das Fermipotenzial des Spiegels und das lineare Gravitationspotenzial bestimmt sind. Für die Genauigkeit des Experiments ist es daher kritisch die Spiegelpositionen genau unter Kontrolle zu bringen, um ungewollte Zustandsänderungen zu verhindern. So wird es notwendig, die Kanten der Spiegel zueinander auszurichten um vertikale Sprünge zu minimieren. Die Kenntnis der Spiegeloberfläche erhöht zusätzlich die Messgenauigkeit.

Das Hauptziel dieser Arbeit ist es, eine Messlösung zu Bauen und Charakterisieren, die die Oberflächen der Spiegel auf Nanometer genau kartieren kann. Dabei ist das Problem, eine stabile Referenz als Koordinatenursprung zu etablieren. Bisherige Lösungen verwendeten eine mechanische Oberfläche als Referenz, was jedoch deren Oberflächendefekte während des Messdurchlaufs mitschleppt. Mit dem Wunsch, die Sensitivität des qBOUNCE-Experiments weiter zu erhöhen, kann die bisherige Lösung vom Auflösungsvermögen her nicht mithalten.

Das vorgestellte neue Oberflächenmesssystem verwendet ein laserbasiertes Positionshaltesystem um eine physikalisch perfekte Referenzebene bereitzustellen. Mit einer grundlegenden Ausführung dieser Technik wird für großformatige Oberflächenmessungen eine Genauigkeit von 192 nm RMS erreicht, wobei dieser Wert in zukünfigen Versionen des Systems auf unter 10 nm RMS reduziert werden soll.

Im Zuge der Optimierung des Prototyps werden externe Störungen wie seismisches und elektrisches Rauschen, Temperatureffekte und die Eigenschaften des signalverarbeitenden Systems im Detail charakterisiert. Zur Demonstration wird die Oberfläche eines Spiegels mit zwei verschiedenen interferometrischen Messgeräten erfasst. Ein weiterer Test zeigt die Tauglichkeit eines glasfaserbasierten Interferometers zur Kalibrierung der Stufen zwischen den Spiegelabschnitten.

Schließlich werden die gewonnenen Kenntnisse verwendet, um Empfehlungen für die nächste Version des Oberflächenmessgeräts zu geben.

Die approbierte gedruckte Originalversion dieser Diplomarbeit ist an der TU Wien Bibliothek verfügbar
The approved original version of this thesis is available in print at TU Wien Bibliothek.
TU Bibliothek Your knowledge hub WIEN

Contents

Die approbierte gedruckte Originalversion dieser Diplomarbeit ist an der TU Wien Bibliothek verfügbar
The approved original version of this thesis is available in print at TU Wien Bibliothek.
TU Bibliothek Your knowledge hub WIEN

Die approbierte gedruckte Originalversion dieser Diplomarbeit ist an der TU Wien Bibliothek verfügbar
The approved original version of this thesis is available in print at TU Wien Bibliothek.

1 Introduction

There are four fundamental interactions known to present-day physics: electromagnetism, the weak and strong nuclear force, and gravity.

In the Standard Model of particle physics, the former three are characterized as interactions of matter where a "force carrier" particle (some variant of a boson) is used to effectuate the interaction. Gravity, on the other hand, is commonly interpreted as the curvature of space-time as part of Einstein's model of general relativity. Both models have been extensively tested and are successful in numerous applications. However, neither can explain the apparent imbalance of matter and antimatter, or the ever-accelerating expansion of the universe.

In the pursuit of a "theory of everything", there are many attempts to reconcile gravitation with the Standard Model and explain the existence of dark matter and dark energy. A very generic approach is to introduce additional fields to represent specific dark interactions. Such fields could give rise to a fifth fundamental force which can be sought out experimentally. For example, many proposed modifications to Newtonian gravity lead to a Yukawa-like interaction potential of the form:

$$V(r) = -G\frac{m_1 m_2}{r}\left(1 + \alpha e^{-\frac{|r|}{\lambda}}\right), \tag{1}$$

where G is the gravitational constant, and the two masses m_1, m_2 are at a distance r to each other. The Yukawa potential is parametrized by a coefficient α and a limited interaction range λ, such that existing observations on the cosmological scale remain unperturbed.

Another approach is the "quintessence" theory that supposes a dynamic scalar field as the origin of dark energy needed to explain the accelerating expansion of the universe. Likewise, this force needs to be screened at certain interaction ranges (e.g. via self-interaction) to avoid existing constraints from experimental data. In turn, these forces may be mediated by new particles such as chameleons [25, pp. 57 ff.].

It is these hypotheses that warrant investigation of the fundamental interactions at small scales with hitherto unmatched precision.

1.1 The *q*Bounce Experiment

*q*Bounce [1, 2] is an experiment which probes gravity interaction on the micrometer scale. The name derives from the "quantum bouncing ball", where the quantum particle traverses a gravity field. The particle bounces off of a reflective surface, equivalent to the bottom of a potential well. Considering only the vertical direction, the particle is trapped between the linear gravity potential and the mirror surface.

As a probe particle, the neutron is chosen for its electric neutrality and its very low susceptibility to magnetic fields. Thus, the measurement is insensitive to common disturbances. Furthermore, the special properties of ultra-cold neutrons (UCNs) are exploited. Due to their extremely low kinetic energy, they undergo total reflection on many surfaces independent of the incident angle [24, p. 15]. In some *q*Bounce experiments, velocity was chosen as $(6.6 \pm 0.7)\,\mathrm{m\,s^{-1}}$ [1]. The low speed also leads to longer observation times which increases the sensitivity of the experiment.

The *q*Bounce experiment uses Ramsey's method of separated oscillating fields to perform spectroscopy [23]. This method uses five sections along the travel path

Die approbierte gedruckte Originalversion dieser Diplomarbeit ist an der TU Wien Bibliothek verfügbar
The approved original version of this thesis is available in print at TU Wien Bibliothek.
TU Bibliothek Your knowledge hub WIEN

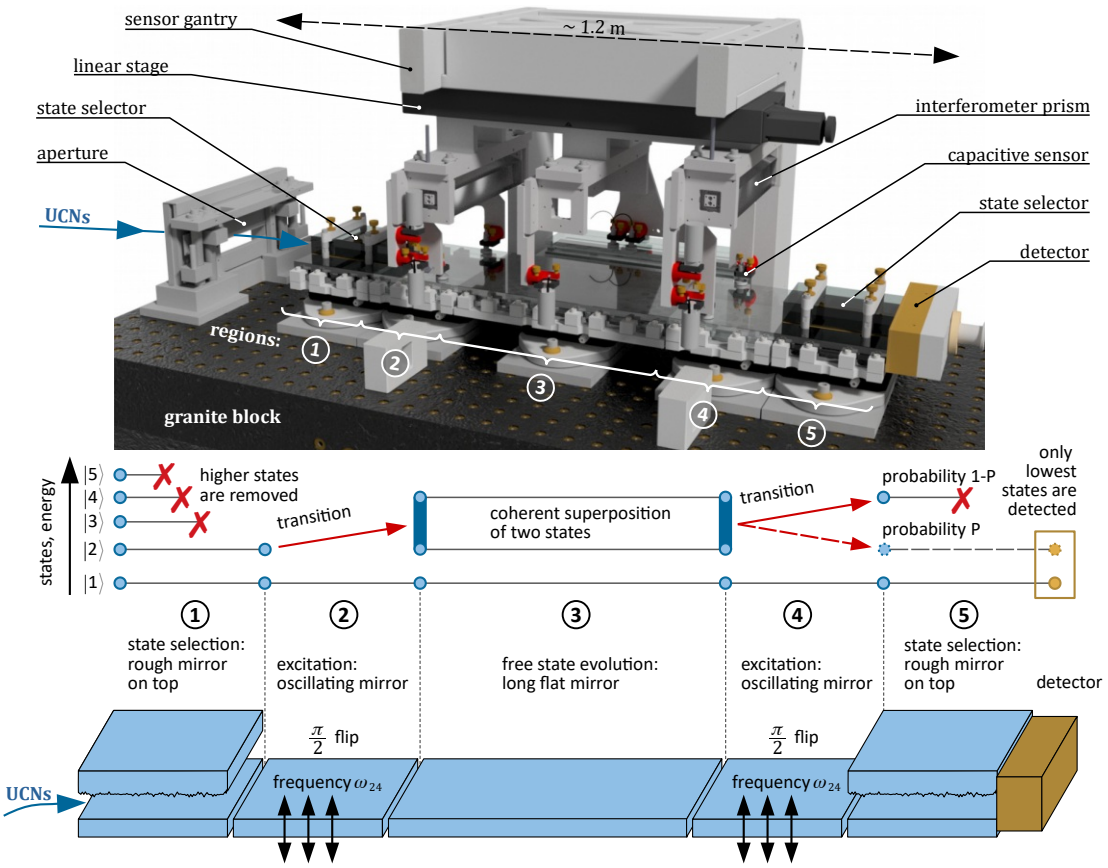

Figure 1: *Schematic of Ramsey gravity resonance spectroscopy setup at* qBounce. *UCNs enter from the left side, traversing to the right. Regions I and V perform state selection by placing an absorber above the mirror, thereby limiting the vertical kinetic energy. Region II and IV oscillate mechanically to induce state transitions, while the states evolve freely during the time spent crossing region III.*

of the UCNs, as shown in figure 1. For more precise alignment, the mirror sections are mounted to piezo actuators which also have the ability to vibrate stages II and IV.

1. First, the lowest energy eigenstate $|1\rangle$ is selected by vertically limiting the flight path with an absorber. After this state preparation, the vertical kinetic energy of the UCNs is in the peV range [2, p. 4].

2. The second region introduces mechanical oscillation of the mirror surface at a predetermined frequency ω_{ex}. In case of resonance with one of the possible state transitions (e.g. $\omega_{|1\rangle\to|2\rangle}$), and when the correct vibration amplitude is chosen, a $\pi/2$-flip occurs.

3. This is followed by an elongated region without vibration, where the particle is in free flight and its state can evolve freely.

4. The fourth region oscillates synchronously with the second. At resonance, another $\pi/2$-flip is induced, so that the particle fully transitions from the base to the higher eigenstate.

Die approbierte gedruckte Originalversion dieser Diplomarbeit ist an der TU Wien Bibliothek verfügbar
The approved original version of this thesis is available in print at TU Wien Bibliothek.
TU Bibliothek Your knowledge hub WIEN

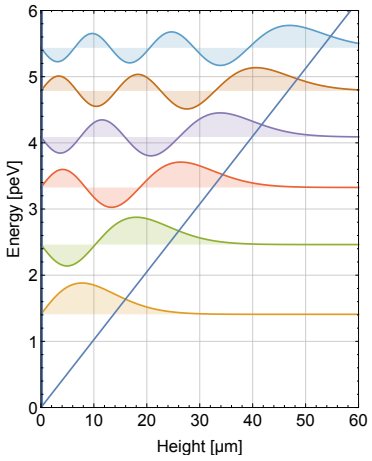

Figure 2: *Wave functions of the quantum bouncer: the UCN is trapped in the vertical direction by the well (shown in blue) created by gravity and the mirror surface. Solution of the time-independent Schrödinger equation yields the Airy functions shown here. Multiple colors represent the wave functions of different UCN eigenstates, shifted by their eigenenergy. [courtesy J. Bosina, 2019]*

5. Finally, in the fifth region, a second absorber is adjusted so that it filters all neutrons that were excited into the target state. Thus, the efficacy of a given vibration frequency and amplitude in exciting the desired energy state is measured by the transmission rate of the particles.

The gravitationally bound state of the particle is described by the non-relativistic Schrödinger equation,

$$\hbar\frac{\partial}{\partial t}\left|\psi(z,t)\right\rangle = \left[\frac{\hbar^2k^2}{2m} + m_n g z + V(z) + V_F\theta\left(-z + a\sin\left[\omega t + \phi\right]\right)\right]\left|\psi(z,t)\right\rangle, \quad (2)$$

where the term $V_F\theta(z,t)$ describes the oscillation of the mirror surfaces. The resulting eigenstates (see figure 2) are non-equidistant and directly dependent on the gravitational force experienced by the probe particle. Any hypothetical forces that interact with the probe particle are represented in the term $V(z)$, directly shifting the energy level depending on the eigenstate n,

$$\Delta E_n = \langle n|V(z)|n\rangle\,. \quad (3)$$

Thus, the impact of any potential $V(z)$ can be precisely measured via the change in transition frequency between specific eigenstates. In the previous experimental setup, an energy resolution of $\Delta E = 2\times10^{-15}\,\mathrm{eV}$ per day of measurement time was achieved using Rabi spectroscopy. Subsequently, new limits for the symmetron theory [8] and chameleon fields [15] were found.

In the experiment, the base particle rate is first established by measuring the output beam without mirror oscillation. Then, the resonances of the quantum system can be measured by observing the variation of throughput while changing the oscillation frequency. At the frequencies corresponding to the state transitions, for example $\omega_{\mathrm{ex}} = \omega_{|1\rangle\to|2\rangle}$, the transmission rate is maximized. So far, the qBOUNCE experiment is able to observe all transitions up to $|1\rangle \to |6\rangle$ or $|2\rangle \to |7\rangle$ [20].

Die approbierte gedruckte Originalversion dieser Diplomarbeit ist an der TU Wien Bibliothek verfügbar
The approved original version of this thesis is available in print at TU Wien Bibliothek.
TU Bibliothek Your knowledge hub WIEN

The measurement works most precisely and efficiently when the mirrors are aligned to the gravitational field, the surfaces are precisely flat, and there is no height difference (steps) between the stages. The latter is especially important, because any step between two adjacent sections translates to a change of the UCN's energy. This leads to unwanted inter-mixing of eigenstates which worsens the measurement accuracy.

A step of 5 µm between region I and II leads to significant mixing of the populated energy levels [7, p. 28]. Later calculations show that a step size of less than 1 µm is desirable [26, p. 53]. This motivates the desire to find tools for the precise alignment and control of the steps and mirror surfaces within the experiment.

1.2 Comparison to Previous Work, Goals

When it comes to the problem of mirror leveling, multiple strategies have been applied over the years. In an early setup based on Rabi spectroscopy, laser interferometry was used to monitor the mirror oscillation [18]. With later iterations and introduction of the Ramsey setup, it was necessary to calibrate the relative position of the five regions to optimize the neutron count rate and accuracy of the measurement.

Each stage consists of a mirror mounted to a piezo table for computer-aided fine-tuning of their alignment. First, the stages are coarsely adjusted with fine-thread screws using manual measurement. It is necessary that the movement range of all piezos has sufficient overlap to allow for later tuning. At this step, the mirror alignment is checked using linear gauges, which offer an accuracy of up to 0.5 µm when manipulated by a skilled operator.

Further fine-tuning is done electronically. For this, a capacitance based surface measurement system was conceived [26, pp. 51 ff.]. An array of four capacitive probes mounted to a linear rail is used to scan the metallic mirror surface. Additionally, three secondary probes are placed over a reference mirror to be able to simultaneously compensate for mechanical imperfections in the rail. Since the horizontal gaps between the mirrors are far smaller than the sensitive diameter of the probe, calculation of the vertical steps is done by linear interpolation of the measured surface data. The piezos are then iteratively adjusted to minimize the height difference between the mirrors. With this approach, an average step height (linear interpolation) of (0.56 ± 0.09) µm is achieved [26, p. 71]. Frequent realignment is required because thermal expansion and drift in the piezo positions causes the stages to shift over time.

Further, an analysis of the problem of mirror leveling yields insight about the linear rail, mirrors and step calculation:

- When the measurement gantry of the capacitive sensor array moves in the Z-direction, it follows the shape of the linear rail, which is not perfect. This causes displacement compared to the ideally straight trajectory with a parabolic shape on the height axis. Also, there are constant changes in pitch, which result in a wobbling motion about the travel axis of the linear rail. The wobble has a periodicity of about 20 mm, which coincides with the distance between mounting screws on the body of the linear rail (see section 4.3). Such behavior has been observed before, in similar measurements [11, pp. 13 ff.].

Die approbierte gedruckte Originalversion dieser Diplomarbeit ist an der TU Wien Bibliothek verfügbar
The approved original version of this thesis is available in print at TU Wien Bibliothek.
TU Bibliothek Your knowledge hub WIEN

- With the capacitive sensor array, surfaces can only be measured relative to the linear rail (which we can safely presume to be warped) or the reference. A map of the "reference flat" is needed to correct the data towards an absolute coordinate system. Data of the reference mirror indicates that higher-order polynomials may be needed to describe its surface [21, p. 12]. This further opens up the methods for step calculation to cubic interpolation and even higher orders [16]. Comparison of interpolation results with manual linear gauge measurements is difficult, since the latter yield very different results depending on the skills of the operator.

- The capacitive probes do not work along the ends of the surface-under-test (SUT) and above the gaps between the mirror surfaces. Some sort of interpolation is therefore inevitable. In order to find a build a good interpolation function, accurate information about the geometric surface of the mirrors is required.

- The comparison of surface profiles captured with the capacitive sensor array [21] indicates another failure mode: the SUT may be "twisted", meaning that the right- and left-hand side of the surface have different curvature. This could make it impossible to eliminate the steps on both ends of the mirror region.

In short, it proves difficult to get a stable, flat reference as a basis for levelling the mirrors.

The prototype presented in this work proposes to use a laser beam running parallel to the mirror surface as the coordinate origin (as described in section 2). This makes the reference independent from mechanical deformations, weight distribution along the movement rail, temperature variation, and many other factors that would disturb any purely mechanical solution. The deflection of mechanical axes would still have the measurement gantry twisting and turning as it glides along them. However, an optical sensor can be used in conjunction with mechanical actuators to counter this movement in accordance with the laser beam reference. The height of the gantry is, in effect, stabilized over the SUT. In an ideal case, the surface measurement data does not need to be corrected, since all adjustments are made before the data acquisition.

The prototype is built to explore the following goals:

1. Measure the height across the mirror surfaces while the experiment does not operate, covering an area of 600×250 mm^2, within an absolute coordinate system.

2. Provide a measurement readout for the vertical steps between the mirrors, so that they can be aligned more reliably than with the previous manual measurement methods.

3. Provide a readout to check phase and amplitude of the oscillating stages while the experiment operates.

4. Reach an accuracy of $\sigma \leq 10\,\text{nm}$ when the mirror is static, within reasonable time of measurement (the shorter the better).

Die approbierte gedruckte Originalversion dieser Diplomarbeit ist an der TU Wien Bibliothek verfügbar
The approved original version of this thesis is available in print at TU Wien Bibliothek.
TU Bibliothek Your knowledge hub WIEN

These specifications are tailored to match and extend upon the performance of the previous surface measurement and control system. The combination of having absolute reference on large-area measurements with nanometer accuracy makes this setup rather unique. We might therefore expect interest in applying this solution in scientific as well as industrial applications.

1.3 Analysis of Commercially Available Solutions

This work presents a novel way of measuring mirror elevation profiles on a nanometer scale. Precise analysis of (reflective) surfaces is a challenge to many industries, most obviously in optics manufacturing and silicon wafer processing, but also has scientific applications in beam line optics or metrological standards. The main problem lies in providing a reference signal that is stable enough to discern surface deviations of a few nanometers over the course of a macroscopic scan area of several meters. Several measurement methods are considered state-of-the-art in providing such measurements.

Electronic inclinometers [6] use a force sensor to compare the surface slant to the earth's gravitational field. The sensor is placed atop the SUT on multiple well-defined coordinates in order to measure the surface slope. The main drawback is the requirement to physically make contact with the SUT. Once a coordinate grid has been established by the user, the overall resolution (and accuracy) of the resulting surface elevation map depends on the number of measurement points placed on this grid. There is no absolute height reference, but elevation may be inferred through integration of the slopes along the surface. Manual placement of the inclinometers creates a high workload for the end-user.

There is also the possibility of interferometry with extremely larges apertures. The University of Arizona demonstrated the use of a phase shifting Fizeau interferometer with 1 m aperture for examination of a mirror 1.6 m in diameter. To produce a complete picture, multiple scans were stitched together computationally, and an impressive RMS accuracy of 6 nm is achieved [6]. Large aperture interferometry does not work properly when steep slopes or steps occur in the SUT, such as when the surface has been milled but not polished [17]. The stitching algorithm also requires a lot of computation and data overlap between each scan, which makes analysis of larger surfaces increasingly difficult. At the same time, the Fizeau interferometer used for measurements is required to have the same or better surface quality than the SUT, which causes extremely high deployment costs.

Another approach is the use of a scanning pentaprism with a system of autocollimators [19]. One autocollimator is lined up with two pentaprisms on a linear rail. The "reference" prism is affixed to the beginning of a linear rail, and another is attached to a movable gantry. The device alternates the beam between the two prisms and compares the deflections created by the SUT. This makes use of the property of right-angle beam deflection of a pentaprism, which is insensitive to a certain range of tilts when properly aligned. However, the system is still sensitive to yaw and roll motion, which is often introduced by minor defects in bearings and linear rails. Constant feedback and micro-motor control is therefore required to keep the prism aligned to the SUT. Scanning pentaprisms can typically measure surface slopes with an RMS error of 1 µrad (compare [19]).

Using linear rails as a reference for measurement always incurs positional error

Die approbierte gedruckte Originalversion dieser Diplomarbeit ist an der TU Wien Bibliothek verfügbar
The approved original version of this thesis is available in print at TU Wien Bibliothek.
TU Bibliothek Your knowledge hub WIEN

orders of magnitude higher that what is measured. This is due to the manufacturing limits of the rails. One solution is to use even better reference surfaces, such as precision polished granite rails with vacuum-preloaded air pressure bearings. With this, RMS errors of 22 nm can be achieved [17]. Such systems offer very good performance and can even be scaled to larger scan ranges up to 600 mm, but they are inevitably more expensive than simple linear rails. The rail error could alternatively be compensated by scanning a "reference flat" and recording the needed corrections, which would incorporate the imperfections of the reference flat into every measurement. Additionally, thermal expansion and other environmental factors may skew the corrections, rendering the result unusable.

The new *q*BOUNCE mirror scanning prototype uses a system where the height reference is provided by a laser beam. A measurement device, in this case a distance-sensing Fabry-Pérot interferometer, is attached to a carriage which is automatically aligned with the reference using a piezo table. This is similar to the technique used in the scanning pentaprism setup, except that it is possible to correct tilt, yaw, roll and height offset all at once using an appropriate feedback configuration. We can use this to our advantage and use cheaper (lower precision) rails for the movement axes, given that the piezo stage has sufficient range to compensate. Setup and adjustment of the hardware is reduced to setting the reference plane via adjustment of the laser source. When the laser beam is widened to a plane of light, the carriage can be shifted sideways without changing the absolute reference. This way, we can capture the surface elevations in relation to an absolute reference over the whole scan area. The length of the rails is virtually unlimited, however the unavoidable de-focusing of the laser beam will continuously reduce precision the further away the carriage moves.

This prototype solves the problem of high-accuracy height references over large measurement areas. The hardware setup is simplified as the reference plane only has to be set once. Since the laser beam remains perfectly straight (under usual conditions), we do not need to rely on expensive high-precision rails or granite tables, which reduces deployment cost. We can use a combination of passive and active vibration isolation to further improve measurement accuracy. Starting from 192 nm of RMS height error without vibration compensation, we aim to achieve better than 10 nm accuracy over a range of $600 * 250$ mm.

The following section will elaborate on the hardware setup of the prototype, describing the measurement gantry and reference laser setup. We will then continue examining the performance of the prototype and error sources, and present mirror surface maps and step measurements created with the new system. Based on these results, recommendations will be given for the next iteration of the surface measurement system.

2 Description of the Setup

The prototype for laser-based large scale surface measurements consists of two cubes constructed from aluminum extrusions. This allows the user to freely position the two cubes on top of the granite base and align the reference laser to the axis of the translator stage. A schematic overview is shown in figure 3.

Die approbierte gedruckte Originalversion dieser Diplomarbeit ist an der TU Wien Bibliothek verfügbar
The approved original version of this thesis is available in print at TU Wien Bibliothek.
TU Bibliothek Your knowledge hub WIEN

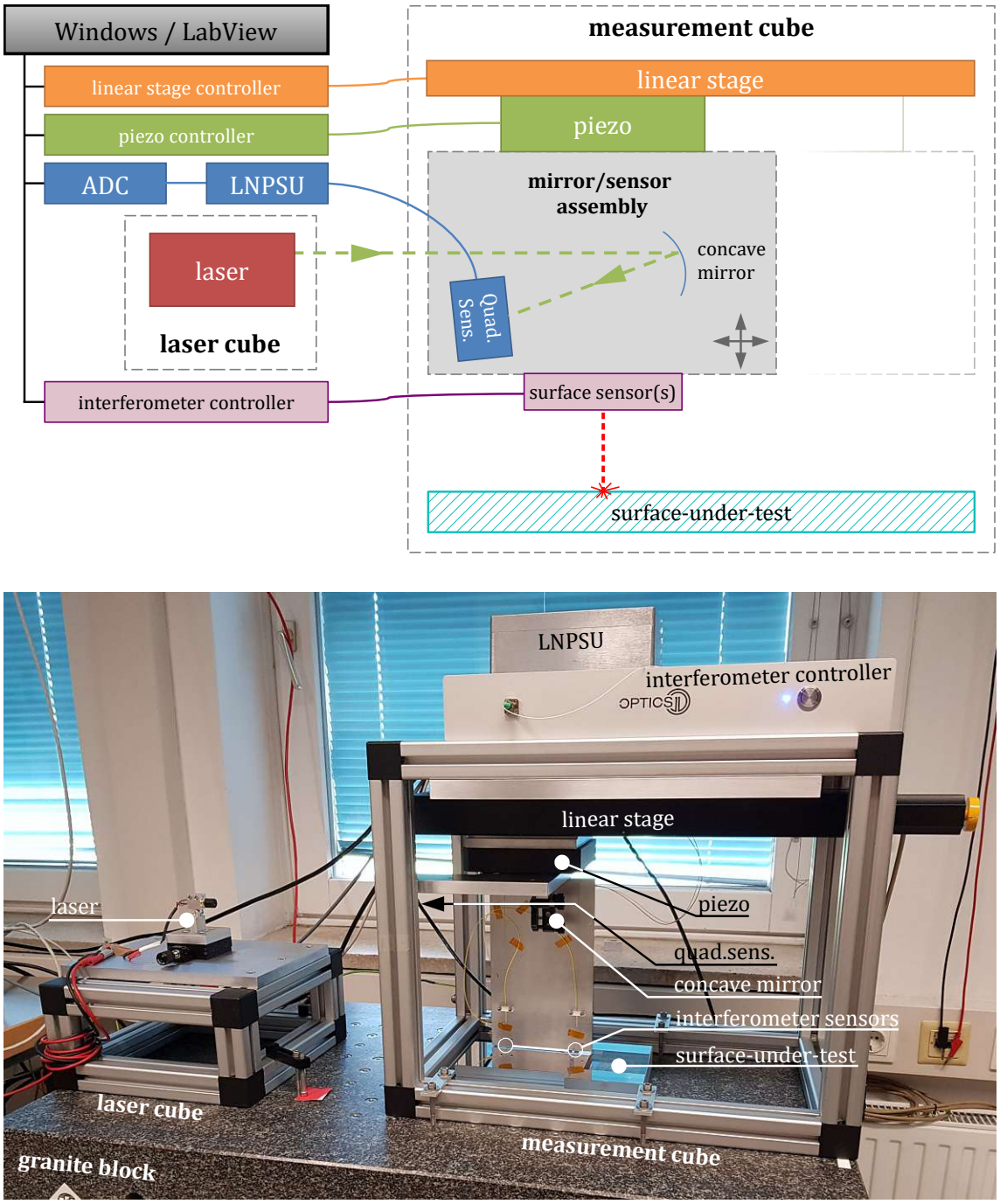

Figure 3: *Schematic overview and block diagram of the prototype. The setup is divided into two main parts, the laser cube (*left*) and the measurement cube (*right*).*
The smaller laser cube is used to position and orient the laser module, which generates the height reference beam. The measurement cube houses a linear stage which can be moved along the laser reference.
An assembly of a concave mirror and quadrant sensor (quad.sens.) is used to control a piezo actuator, which keeps the measurement gantry at the reference height. The quad.sens. is connected by a single cable to the low-noise power supply unit (LNPSU), which is responsible for separating supply voltage and sensor signals.

Die approbierte gedruckte Originalversion dieser Diplomarbeit ist an der TU Wien Bibliothek verfügbar
The approved original version of this thesis is available in print at TU Wien Bibliothek.
TU Bibliothek Your knowledge hub WIEN

2.1 Measurement and Laser Cube

The smaller cube, referred to as **laser cube**, houses the laser diode generating the reference beam that is read by a photodetector on the measurement sled. In the prototype, a laser module with constant-current supply is used (Roithner CW532-001). This simple module is much akin to what can be found inside a laser pointer, with a wavelength of 532 nm, a beam diameter of 1.5 mm and a radiated power of just under 1 mW. A simple mechanism (hinge with locking screw) allows the beam to be tilted on the XZ-plane and shifted along the Y-axis. Bigger adjustments are done by shifting/rotating the whole cube and/or propping it up on precision spacers.

In the prototype, the laser is static and does *not* adjust to external disturbances like temperature expansion or mechanical vibrations. We will later see that mechanical vibrations are the biggest contributor in reducing measurement accuracy (see section 3.1.3).

The larger **measurement cube** contains a linear stage carrying the measurement sled, such that it travels along the length of the reference beam. A piezo actuator is used in conjunction with a photodetector for tracking the position of the sled relative to the reference height and compensate accordingly. This allows the two cubes to measure the surface-under-test (SUT) with an absolute coordinate reference. The feedback and positioning system is controlled by a computer running LabView 16 and Windows 7. The surface data is acquired from the digital interface of the interferometric measurement device mounted on the sled.

2.2 Movement System

The measurement sled moves on a linear rail system in order to gain complete coverage of the SUT. In the prototype, the movement system only allows one travel axis along the length of the SUT, while in future revisions, an additional linear stage will enable sideways movement, as well.

In this case, a Physik Instrumente (P.I.) miCos HP-170 High Precision Linear Stage is attached to the underside of the top of the measurement cube in an upside-down orientation, about 40 cm from the granite surface. The travel range is 277 mm with the zero coordinate at the end farthest from the laser source, next to the yellow hand-wheel (shown on the right in figure 3). The gantry is moved along the rail by a stepper motor driving a lead screw mechanism, an optical encoder wheel offers a resolution of 50 nm. The stepper controller is a P.I. SMC corvus eco, which can be addressed via USB or serial interface and can control up to three axes.

Between the sled of the linear stage and the measurement gantry, a piezo actuator is used for height correction according to the reference beam. The piezo device used is a P.I. P-518.TCD Nanopositioning Stage with a Z range of 100 µm and a tilt range in X and Y direction of 1.4 mrad each. The P-518 itself does not contain any active electrical components, but there are four capacitive sensors (one in each corner), which can be used to measure the position and tilt of the stage. The control voltage for the piezo is generated externally by the P.I. E-712 Digital Piezo Controller, which in our case is connected via Ethernet. The input commands come from the LabView PC which coordinates the measurement process.

Die approbierte gedruckte Originalversion dieser Diplomarbeit ist an der TU Wien Bibliothek verfügbar
The approved original version of this thesis is available in print at TU Wien Bibliothek.
TU Bibliothek Your knowledge hub WIEN

2.3 DeltaSens Interferometer

The Optics11 DeltaSens is an interferometer-based measurement device. Up to 12 sensors can be attached to a single fiberoptic cable and their distance values queried simultaneously. In order to achieve this, DeltaSens continuously modulates the wavelength of its internal laser between $\lambda = 1509 \ldots 1595\,\mathrm{nm}$ (in the infrared spectrum). A signal processor locks onto the individual fringes provided by interference in each distance sensor and actively tracks their positional shift. Through an FFT calculation, it is also possible to determine the absolute distance, albeit this slows down the measurement frequency. In the fast/relative tracking mode, sampling rates of up to 17 kHz can be achieved. The speciality of DeltaSens is that this high sampling rate can be maintained while simultaneously querying all of the distance sensors.

The DeltaSens generates and evaluates the laser signal in a single box, which contains the electrical power input and several user-programmable analog outputs. The laser signal is output via a FC/APC connector. For our measurement setup, a fiber-optic splitter is used to allow the measurement of two different points on the measurement gantry. The signal can be split further in order to connect up to 8–12 sensors. The interferometric cavities ("distance sensors") are established between the cleaved end of a fiber pointing towards the mirror, and the mirror surface itself. Due to signal loss by beam divergence, the distance inside the sensor needs to be smaller than 1 mm. A size difference of at least 100 µm is needed to be able to distinguish clearly between multiple sensors. The sample acquisition rate is set in most measurements presented in this thesis to 10 kHz.

The DeltaSens interferometer has two different modes of operation: relative tracking and measurement of absolute distances. Using **relative mode**, changes in the sensor value are measured by by following the fringe of the interferometric pattern, from which the change in distance is derived. The resulting value is shifted by some arbitrary offset which can be zeroed by the user before starting the measurement. In case of signal interruption by loss of contrast or fast signal transients that exceed the sampling rate, the positional offset is lost. Upon reacquisition of the fringe, the distance measurement may be shifted by a multiple of $\lambda/2$. This effect is referred to as "fringe-skipping".

The **absolute measurement mode** is facilitated by the internal laser source which has tunable wavelength. The procedure is demonstrated the following sections. The absolute mode does not use fringe tracking and is capable of keeping distance information even during loss of signal. This makes it possible to map the position of two discontinuous parts of the SUT with respect to the sensor position.

2.3.1 Basics of Relative Mode Measurements

The working principle of DeltaSens is to read multiple Fabry-Pérot interferometers simultaneously by variation of the laser wavelength. Each of the up to 12 interferometer cavities represents a "sensor" which changes its size according to the physical process in question (e.g. acoustic vibrations, acceleration forces deflecting a cantilever).

In order to be able to perform a relative mode measurement, the change in cavity size is observed by tracking the fringe pattern that results from optical interference. In a system with a single cavity, this would suffice to determine the

Die approbierte gedruckte Originalversion dieser Diplomarbeit ist an der TU Wien Bibliothek verfügbar
The approved original version of this thesis is available in print at TU Wien Bibliothek.
TU Bibliothek Your knowledge hub WIEN

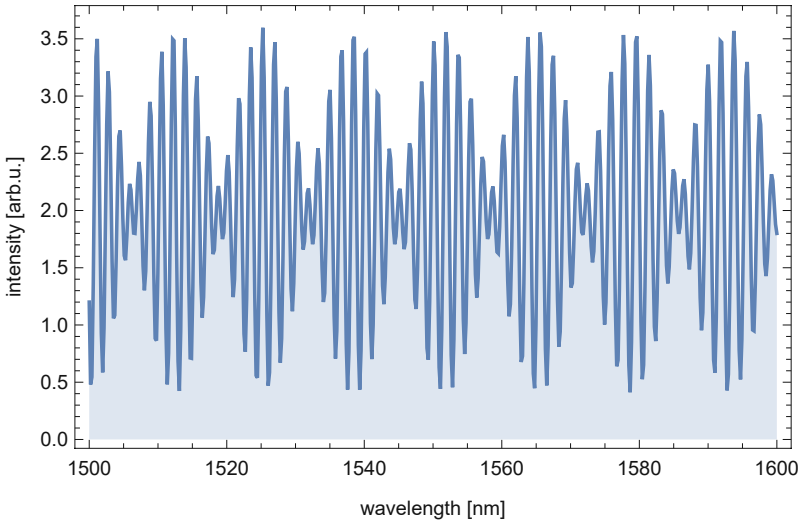

Figure 4: *Result of a DeltaSens wavelength sweep for synthetic input data generated from equation 4 with the coefficients from table 1. The peaks (and/or valleys) seen here can be tracked using a signal processor. Any changes in-between wavelength sweeps are interpreted as changes in cavity size through "phase-unwrapping".*

relative movement of the sensor. In order to observe the movement of multiple sensors quasi-concurrently, DeltaSens modulates the laser wavelength λ rapidly, so that the wavelength sweeps are performed at rates of up to 17 kHz.

The intensity that is measured for each cavity i varies with the optical path length d and the wavelength λ. This is described by the following equations,

$$f_i(d_i, \lambda(t)) = A + B\cos\left(2\pi\frac{2d_i(t)}{\lambda(t)}\right), \tag{4a}$$

$$d_i(t) = d_{i,0} + v_i t, \tag{4b}$$

$$\lambda(t) = \lambda_0 + \Delta\lambda\cos\left(\omega_{\mathrm{m}} t\right), \tag{4c}$$

$$f^{\mathrm{total}} = \sum_i f_i, \tag{4d}$$

where v_i is the change rate of the cavity size. The laser wavelength λ is modulated around the base value λ_0 in the range of $\Delta\lambda$ with a scan frequency of ω_m. When multiple cavities are attached, their interference patterns are superimposed according to equation 4d. The coefficients A, B determine contrast and amplitude measured by the interferometer.

An example of a wavelength sweep can be seen in figure 4, for synthetic data generated from equation 4 and the coefficients from table 1. At this point, the peaks (and/or valleys) of the interference fringes can be tracked using a signal processing algorithm. The different cavity sizes (down to multiples of $\lambda/2$) are the solutions of a numerical fit of equation 4c to the complete wavelength-sweep as shown in figure 4. Further details are beyond the scope of this thesis.

Die approbierte gedruckte Originalversion dieser Diplomarbeit ist an der TU Wien Bibliothek verfügbar
The approved original version of this thesis is available in print at TU Wien Bibliothek.

		cavity 1	cavity 2
cavity size	d	620 nm	710 nm
contrast	A	1	1
amplitude	B	0.7	0.9

Table 1: *Coefficients chosen for demonstration of the DeltaSens measurement principle. Together with equation 4, the interference intensity of a two-cavity system is given by $f^{total}(d_1, d_2, \lambda)$.*

2.3.2 Phase Unwrapping and Fringe-Skip

Starting from equation 4, the terminology of "phase unwrapping" and "fringeskips" can be explained. In both cases the phase change in the cosine term is relevant. The value of sine and cosine functions is identical when their argument is phase shifted by one full period,

$$\cos\varphi = \cos(\varphi + 2\pi n), n \in \mathbb{Z}.$$

In equation 4a, any change in cavity size d causes in a phase change of the cosine argument. As a consequence, the interference fringe is shifted on the wavelength sweep (figure 4). When, through successive relative motion of the cavity, a total phase of 2π is accrued, the resulting wavelength sweep would is identical to that from the starting point of the cavity.

This would result in an erroneous readout as soon as the cavity size exceeds a certain distance. Instead of a continued distance readout, the sensor value would be reset to the starting point. The work-around is to implement **phase unwrapping**, which detects when the accumulated phase reaches the threshold of $2\pi n$ and allows to carry over the full phase for calculating the distance travelled.

Sometimes the cavity size changes rapidly, for example during transients introduced by a seismic shock or steep features on the SUT. In these cases, it is possible that the a phase change in excess of 2π is incurred quasi instantly. When the time resolution of the relative mode measurement is insufficient, this then leads to an effect called **fringe-skipping**. The fast changes in cavity size can no longer be tracked and the algorithm "skips" over one or multiple interference fringes in an attempt to reacquire the position signal. Ultimately, this results in a misrepresentation of cavity size in the measurement results.

We can derive a limit on the change rate v of the cavity size, starting with the cosine argument from equation 4a. For this argument, we will focus on a interferometer setup with only one cavity of size d. In order to avoid ambiguity in the fringe tracking, the phase change during the period Δt between wavelength sweeps must stay below 2π.

$$\frac{\partial}{\partial t}\left(2\pi\frac{2d(t)}{\lambda(t)}\right)\Delta t < 2\pi \tag{5}$$

Inserting the definition of $\lambda(t)$ from equation 4c, using $d(t) = v\Delta t$, and executing the differential, we arrive at the exact condition for avoiding fringe-skips. This can be expressed as a velocity limit as follows:

$$v\Delta t < \frac{-2d_0\Delta\lambda\omega_m \sin(t\omega_m) + \lambda_0^2 + \Delta\lambda^2\cos^2(t\omega_m) + 2\Delta\lambda\lambda_0\cos(t\omega_m)}{2\left(\lambda_0 + \Delta\lambda t\omega_m \sin(t\omega_m) + \Delta\lambda\cos(t\omega_m)\right)} \tag{6}$$

Die approbierte gedruckte Originalversion dieser Diplomarbeit ist an der TU Wien Bibliothek verfügbar
The approved original version of this thesis is available in print at TU Wien Bibliothek.
TU Bibliothek Your knowledge hub WIEN

Considering the typical values of $\lambda_0 = 1500\,\mathrm{nm}$ and $\Delta\lambda = 50\,\mathrm{nm}$, we can assume $\Delta\lambda \ll \lambda_0$ as a rough approximation. The velocity condition then reduces to

$$v\Delta t < \frac{\lambda_0}{2} + \mathcal{O}(\Delta\lambda), \tag{7}$$

which corresponds to what one would expect intuitively. This explains why the error in the reported position is a multiple of $\lambda_0/2$ when fringe-skipping occurs, as the tracking algorithm skips over one or multiple fringes before reacquiring a signal.

2.3.3 Absolute Mode Measurements

The DeltaSens is also capable of measuring **absolute distance** information. First, the intensity of interference is measured under variation of the laser wavelength. The resulting wavelength sweep is identical to what is used in relative mode, so that both types of measurement can be done concurrently. For gathering the absolute distance information, the intensity graph is subjected to FFT analysis. The internal signal processor of the DeltaSens applies a mathematical window function (e.g. the Blackman-Harris window) to the dataset. Then, the windowed data $f^{\mathrm{total}}(d, \lambda(t))$ is subjected to the Fourier transformation

$$\mathcal{F}_{t\omega} = \frac{1}{\sqrt{2\pi}} \int_{-\infty}^{\infty} f^{\mathrm{total}}(d, \lambda(t)) e^{-\mathrm{i}\omega t} \mathrm{d}t, \tag{8}$$

which returns a spectrum of intensities in dependency of absolute cavity sizes. Both of these steps are shown in figure 5 for the synthetic data from figure 4. Two spikes on the distance scale now represent our previously chosen cavity sizes d_i, and can be evaluated with a peak tracking algorithm (implemented in the DeltaSens hardware).

These two modes of measurement shown above, relative and absolute mode, are proposed to be used at different times during the monitoring of the qBOUNCE experiment, in accordance with the goals stated in section 1.2. The relative mode with its high sample rate enables fast acquisition of mirror surface maps, while the absolute mode can be used to calibrate the steps between the mirror stages.

2.4 DeltaSens Measurement Sled

The measurement sled is mounted on the stabilized piezo platform and is is used to mount the surface measurement device. It can either be adapted to hold the sensor head of the SIOS SP 2000 TR triple-beam interferometer or carry the fibers of the DeltaSens interferometer. Both devices are used to measure the relative change in distance between the sensor head and the mirror surface. Meanwhile, the mirror-sensor assembly works together with the piezo actuator to assure that the measurement gantry stays at reference height.

One version of the gantry, adapted towards use with DeltaSens, extends down from the piezo table and has two fibers running parallel to its edge. These two two "pig-tail" optical fibers form the surface sensor array, and are cleaved at a 0° angle. The fiber ends point toward the SUT (see figures 6 and 7) so that an optical cavity is created between the end of the fiber and the mirror. When using multiple fibers, their cavity sizes need to be adjusted such that they are in accordance with the limitations of DeltaSens: smaller than 1 mm, but different from each other by at

Die approbierte gedruckte Originalversion dieser Diplomarbeit ist an der TU Wien Bibliothek verfügbar
The approved original version of this thesis is available in print at TU Wien Bibliothek.
TU Bibliothek Your knowledge hub WIEN

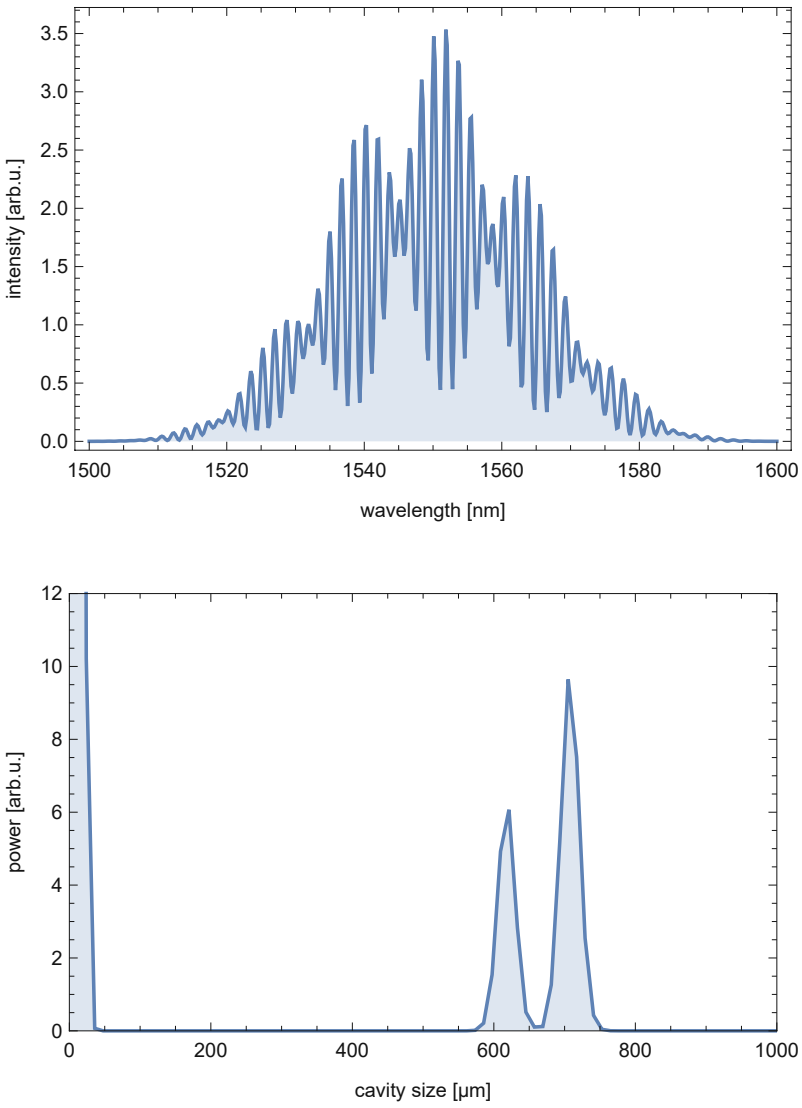

Figure 5: *Principle of DeltaSens absolute distance measurement.* Top: *simulated data from a single wavelength sweep (see figure 4) after multiplication with the Blackman-Harris window.* Bottom: *result of FFT transformation of data shown on top. Two spikes on the distance scale represent the two cavities chosen according to table 1.*

Die approbierte gedruckte Originalversion dieser Diplomarbeit ist an der TU Wien Bibliothek verfügbar
The approved original version of this thesis is available in print at TU Wien Bibliothek.

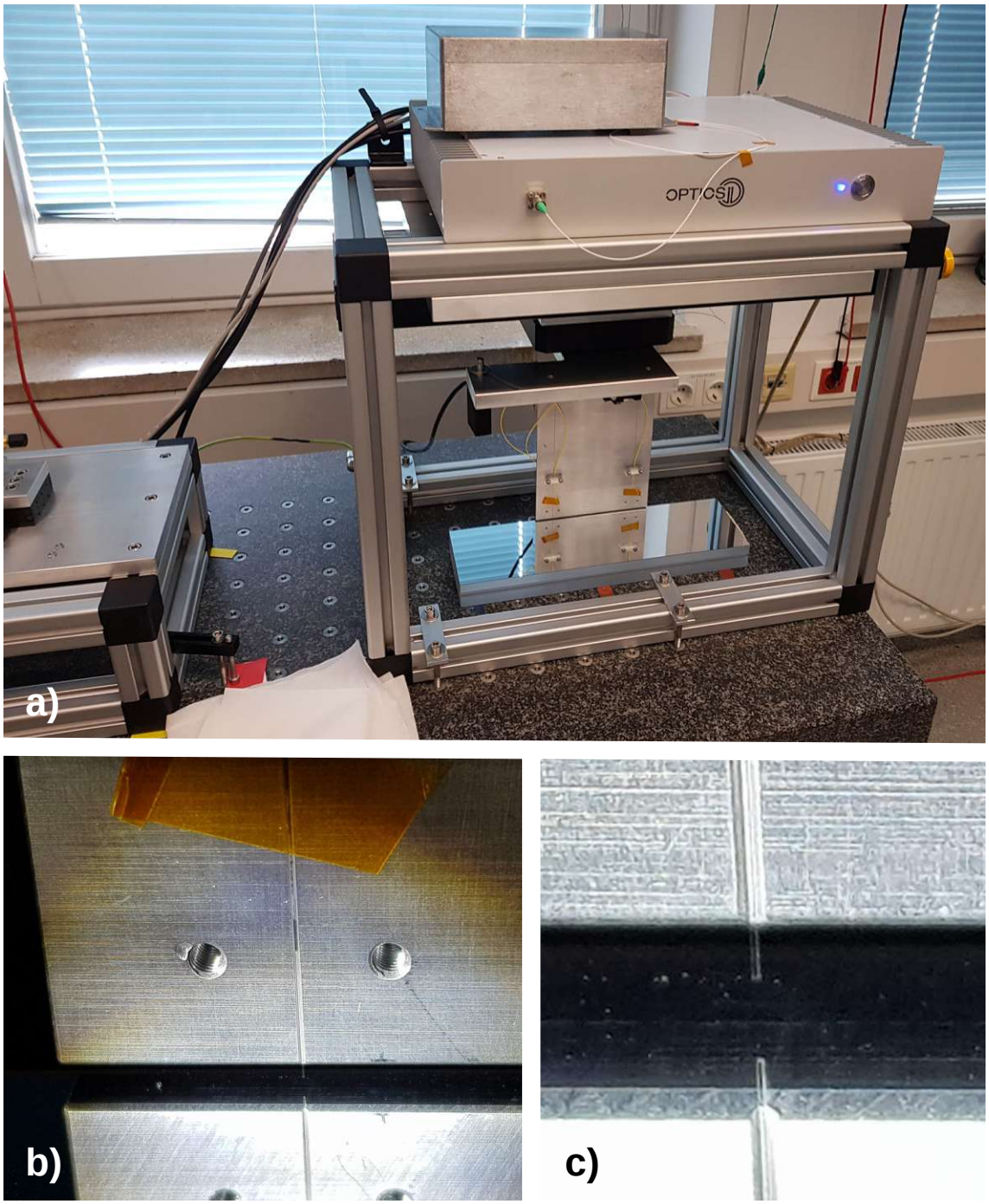

Figure 6: *Configuration for DeltaSens measurements. Two optical fibers are cleaved at a* $0°$ *angle and attached to a movable carrier, pointing straight toward the SUT. This creates an optical cavity that can be read by the interferometer device.* b) *and* c) *show closeups of the optical fiber.*

Die approbierte gedruckte Originalversion dieser Diplomarbeit ist an der TU Wien Bibliothek verfügbar
The approved original version of this thesis is available in print at TU Wien Bibliothek.
TU Bibliothek Your knowledge hub WIEN

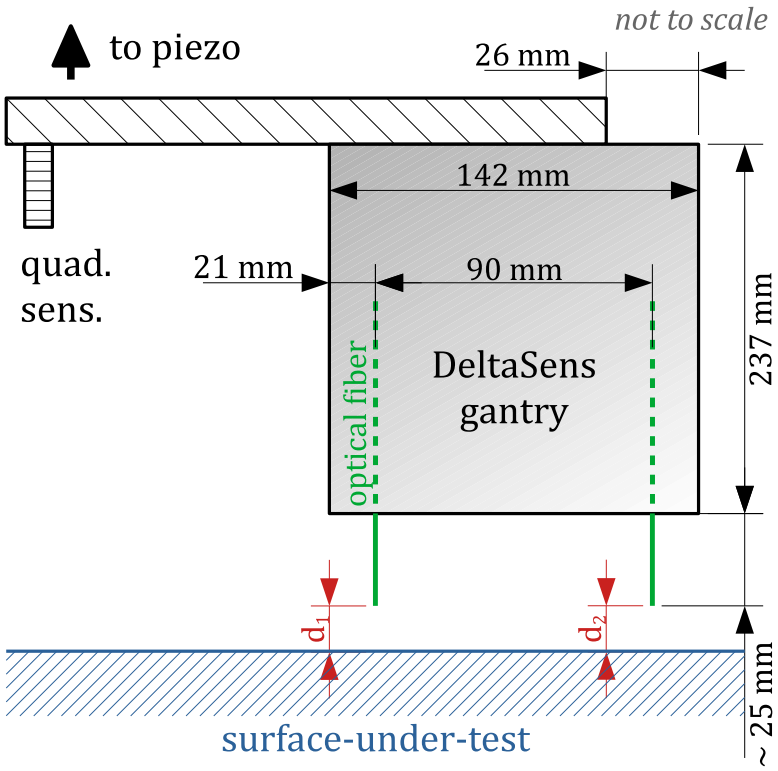

Figure 7: *Schematic side view of the DeltaSens measurement gantry. The gantry plate (shown in gray) is attached to the linear stage and piezo actuator (not shown). Two cleaved glass fibers are pointed toward the SUT for capturing the surface map. The distance of the fiber to the SUT is below* 1 mm.

least 100 µm. Providing for some headroom toward the mirror surface, this allows for the use of 6 to 8 sensors. The measurements shown in figure 7 can be used to calculate the position of the fiber sensors relative to the X coordinate reported by the linear positioning system.

The measurement sled is moved along the axis of the linear stage while the feedback system actuates the piezo and constantly keeps the measurement device at the reference height. In order to avoid fringe-skipping, movement speeds of the linear stage need to be limited to $v_{\max} = 0.1\,\mathrm{mm\,s^{-1}}$ and $a_{\max} = 0.1\,\mathrm{mm\,s^{-2}}$. Practical testing indicates that any faster movement would destabilize the DeltaSens relative mode tracking algorithm due to mechanical vibration in the system.

Using the movement mechanism in conjunction with the DeltaSens measurement device, a map of the SUT can be acquired. Since, in the prototype, the measurement sled can only move along the X direction, the SUT itself needs to be shifted to the side (in Y direction) on the optical granite in order to measure multiple elevation profiles across the mirror surface. Combining several measurement sweeps then results in a three-dimensional grid of coordinates (a surface map).

2.5 SIOS Interferometer

The SIOS SP 2000 TR three-beam interferometer uses a modified Michelson layout to measure distances up to 2 m with a resolution of 0.1 nm. For flat reflectors, the

Die approbierte gedruckte Originalversion dieser Diplomarbeit ist an der TU Wien Bibliothek verfügbar
The approved original version of this thesis is available in print at TU Wien Bibliothek.
TU Bibliothek Your knowledge hub WIEN

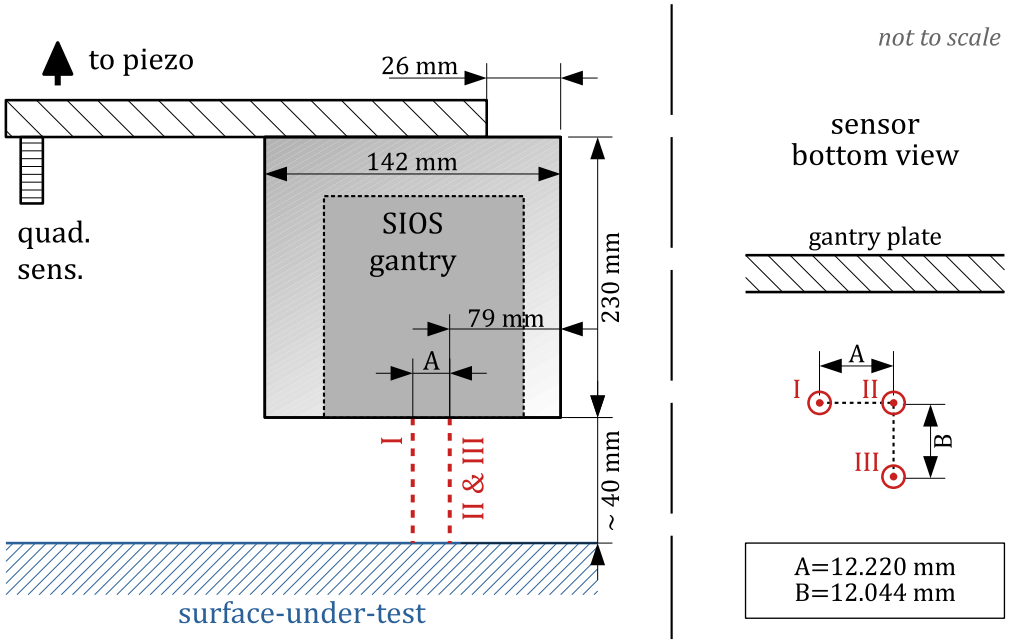

Figure 8: Left: *Schematic side view of the* SIOS *measurement gantry. The* SIOS *sensor box (dotted rectangle) is attached to the back side of the gantry plate. The assembly is connected to the piezo actuator and linear stage (not shown). The sensor box can be tilted to align the lasers orthogonal to the SUT.*
Right: *view of the sensor arrangement from below. Three laser outputs (red: I, II, III) are positioned in an L-shape, pointing towards the viewer. Distance between them (A, B) is precisely measured to be able to compensate for lateral coordinate shifts.*

beam angle needs to be less than 1.5′ (4.36 mrad) [12, p. 17].

Compared to the DeltaSens, it is better suited toward industrial applications and features a more modular rugged design, which also takes up more space. The main box "Versorgungs- und Auswerteeinheit" (VAE) holds the power supply module, a laser frequency stabilizing device, serial I/O, and control modules for each laser beam and sensor. There is also the possibility to monitor ambient values and automatically apply corrections for changes in temperature, humidity and barometric pressure. A He-Ne-laser is housed in the back of the VAE, producing an output power of 2 mW at $\lambda = 632.8$ nm [12, p. 6].

The SP 2000 TR itself is a stainless steel box (seen in figure 9), which weighs 2.5 kg and receives the laser input from the VAE using an E2000 fiber connector [12, p. 7]. The sensor box contains a triple beam splitter and electromechanical components to modulate the laser signal. In contrast to the DeltaSens, where the photodetector sits in the main box, the SP 2000 TR contains a separate detector for each beam directly inside the sensor box [12, p. 17]. This means that there are active electronic components inside the sensor box that communicate with the VAE via three 15-pin cables. An additional box containing the ambient sensors is connected with a 9-pin cable and can be placed at a convenient location.

Figure 8 shows the dimensions of the SIOS gantry. The sensor box is attached to the gantry plate, extending down so that the outlets of the beam splitter are placed some centimeters above the mirror surface.

Die approbierte gedruckte Originalversion dieser Diplomarbeit ist an der TU Wien Bibliothek verfügbar
The approved original version of this thesis is available in print at TU Wien Bibliothek.
TU Bibliothek Your knowledge hub WIEN

There are three sensors (I, II and III) arranged in an L-shape [12, p. 90]. This allows for simultaneous measurement of two lines across the mirror surface with sensors II and III. Sensor I is placed in line with sensor II, but shifted in the direction of the linear rail.

When acquiring measurements with the SIOS gantry, the mirror is moved sideways by a multiple of the distance between sensors II and III after every pass. The resulting overlap causes each line to be measured by sensor II and III during two adjacent measurements, which makes it possible to compare their results later.

2.6 The Quadrant Detector

The mirror-sensor assembly consists of a concave mirror ("reflector", ThorLabs CM254-075-E02) and a position-sensing photo-detector ("quad.sens.", ThorLabs PDQ80A). The reflector is held by a kinetic mirror mount, which allows tilt and yaw to be adjusted with precision screws. The mirror diameter is $d = 25.4\,\text{mm}$, with a curvature of $R = 75\,\text{mm}$. Since the reference beam uses green light (visible spectrum), a dielectric surface coating is used. The reflector is tilted such that the reference beam hits the center of the quad.sens. when the carriage is at the height of the reference beam. This is used in conjunction with the laser cube (see below) to define the height and tilt of the reference plane. The position and angle under which the laser beam hits the mirror are relevant to the overall sensitivity of the system, and dependent on the curvature R of the reflector (see section 3.3.2).

The quad.sens. is a silicon photo-diode detector which is used to determine the position of the gantry relative to the laser beam reference. Its sensitive area is split into four quadrants, $Q_1 - Q_4$, each with an analog voltage output $S_{Q1} - S_{Q4}$ (as shown in figure 10). The sensor provides three analog outputs: two signals depending on the position of the laser beam ("X" and "Y"), and a "SUM" signal which indicates the total signal level. These signals are generated within the detector housing by combining the quadrant signals as follows:

$$\begin{aligned} \text{X} &= (S_{\text{Q2}} + S_{\text{Q3}}) - (S_{\text{Q1}} + S_{\text{Q4}}), \\ \text{Y} &= (S_{\text{Q1}} + S_{\text{Q2}}) - (S_{\text{Q3}} + S_{\text{Q4}}), \\ \text{SUM} &= S_{\text{Q1}} + S_{\text{Q2}} + S_{\text{Q3}} + S_{\text{Q4}} \end{aligned} \tag{9}$$

When the laser is perfectly aligned with the center of the detector, the position signal becomes 0 V, while the SUM signal presents some positive voltage indicating overall signal strength. A laser beam with a circular Gaussian cross-section centered on the detector produces equal signal levels in each of the quadrants, with the voltage balance shifting accordingly if the beam is de-centered from the optical axis. Through simple cross-correlation, the output voltage of the sensor can be converted into a distance measurement (see section 3.3.1).

The analog signals generated by the quad.sens. are passed along a single shielded cable to the LNPSU, which generates the supply voltage for the analog amplifiers and branches out the return signals. The unit is specially constructed at TU Vienna to offer a signal-to-noise ratio of around 100 dB. This ensures that the quad.sens. works with as little electronic noise as possible, as this has a direct effect on the performance of the whole feedback mechanism.

For the positional feedback in the prototype, we exclusively use the Y-channel which corresponds to the height deviation of the gantry towards the reference. A 5 Hz

Die approbierte gedruckte Originalversion dieser Diplomarbeit ist an der TU Wien Bibliothek verfügbar
The approved original version of this thesis is available in print at TU Wien Bibliothek.
TU Bibliothek Your knowledge hub WIEN

Figure 9: *Photo of the measurement gantry for the* SIOS *interferometer. The interferometer laser is split up into three beams inside the sensor box. Each beam is evaluated separately. With* SIOS*, the vertical distance to the mirror surface is much larger (some* cm*) than with the DeltaSens gantry.*

Die approbierte gedruckte Originalversion dieser Diplomarbeit ist an der TU Wien Bibliothek verfügbar
The approved original version of this thesis is available in print at TU Wien Bibliothek.

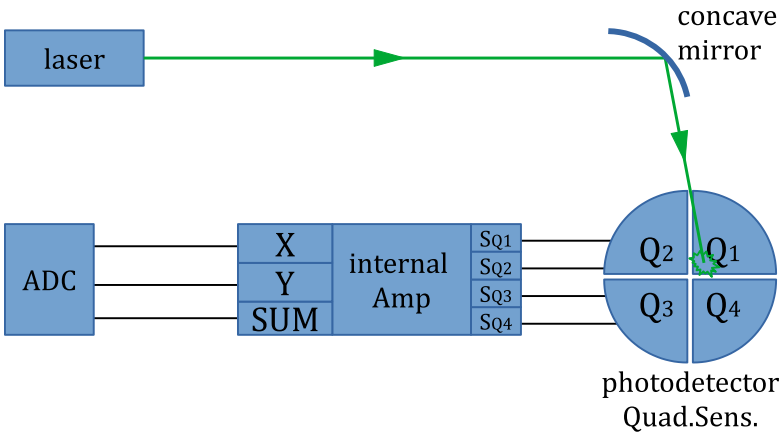

Figure 10: *Schematic view of the quad.sens. signal path. The light from the reference laser is reflected onto the photodetector based on the vertical position of the measurement gantry. This produces a photocurrent for each quadrant according to the observed light intensity. Inside the quad.sens. housing, an amplifier circuit converts the quadrant signals into voltages (see equation 9) that correspond to the X and Y position on the detector plane. The analog signals are then captured by an analog-to-digital converter (ADC).*

first-order low-pass filter is applied to this channel in order to suppress vibrational and electronic noise in the amplifier. The resulting signal is then passed on to the external ADC.

The return signals are passed on to the external ADC (Silicon Systems VI01 Octal Voltage Monitor), where they are digitized. This device uses power-over-Ethernet and offers 8 input channels at a sampling rate of up to 3 kHz. The quad.sens. only generates three signals, so it is advantageous to connect each signal to two channels for the purpose of averaging and reduction of line noise.

In terms of feedback range, the quad.sens. has a nearly linear output characteristic for signal levels of up to 80 % of the SUM signal. It is important to ensure that the SUM signal stays constant over the course of the measurement. Any drastic change would indicate the loss of tracking or unreliability of the signal outputs.

2.7 GAS filter

In order to achieve accurate results at nanometers of depth resolution, it is important to isolate the measurement system (and reference laser) from vibrations. In the prototype under test in this work, some small amount of vibration reduction is provided by a massive optical granite table resting on foam padding. The impact of seismic noise on our measurements is assessed in section 3.1.3.

The upcoming iteration of the setup uses a system of springs to isolate the laser reference and measurement gantry from outside vibrations. In order to provide high attenuation at long observation periods (low frequencies), so-called geometric anti-spring (GAS) filters are used, where the payload is mounted on a set of spring blades and held in balance by gravitational force. This type of filter design has been proven in the field of gravity wave detection [3–5].

The GAS filter prototype (see figure 11) consists of three flat spring steel can-

Die approbierte gedruckte Originalversion dieser Diplomarbeit ist an der TU Wien Bibliothek verfügbar
The approved original version of this thesis is available in print at TU Wien Bibliothek.

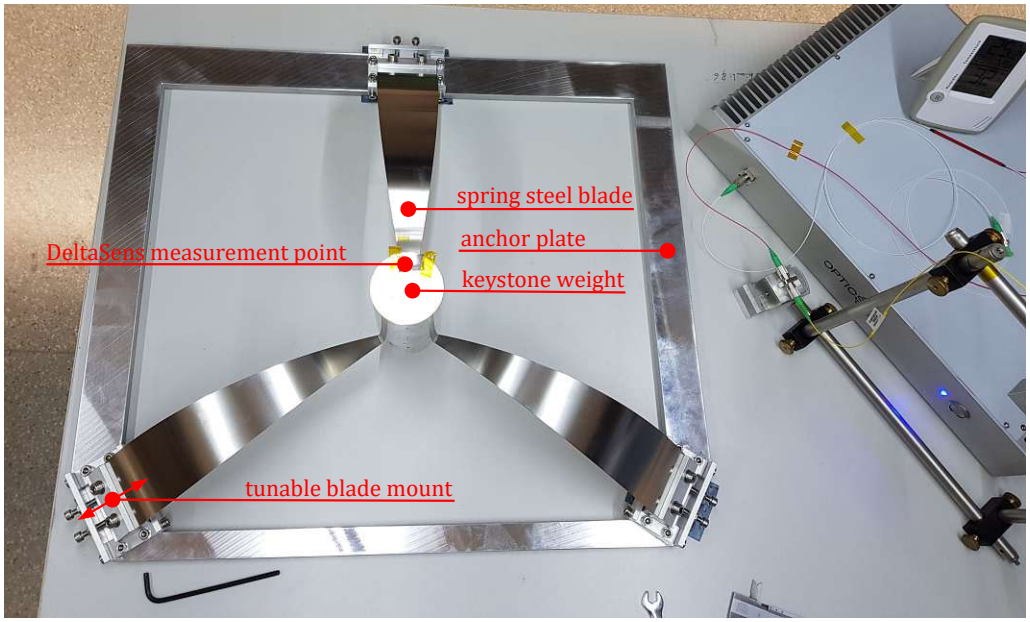

Figure 11: *Prototype GAS filter configuration, viewed from the top. The spring stiffness can be tuned by moving the blade mounts in- or outward, thereby changing the resonance frequency.*

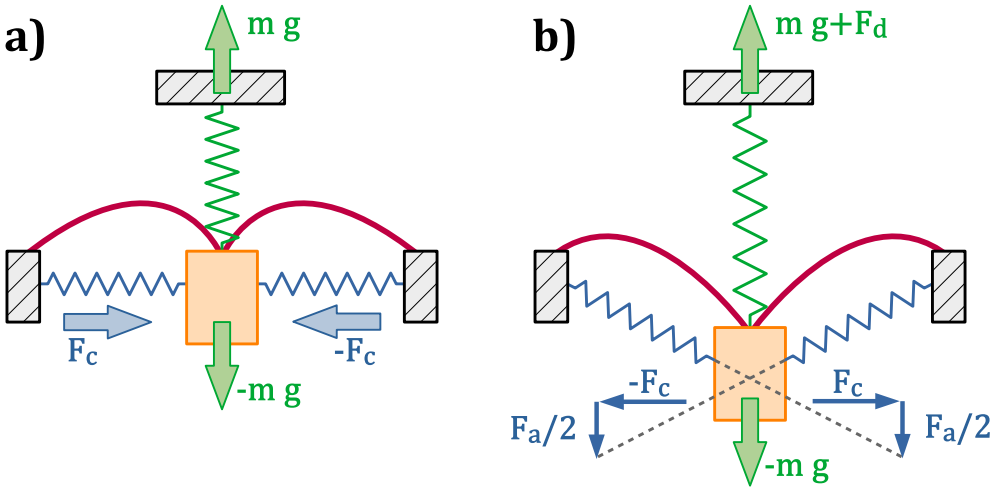

Figure 12: *2-dimensional representation of the forces in a GAS filter. Spring symbols have been added for illustration purposes.* (a) *At the working point, the spring blades (red) create an upward force (green) to compensate the weight of the keystone (orange). The forces of the radially compressed springs F_c (blue) cancel each other out.* (b) *When the keystone is pushed outside the working point, the blade springs create an anti-spring force F_a which partially cancels the primary spring force F_d.*

Die approbierte gedruckte Originalversion dieser Diplomarbeit ist an der TU Wien Bibliothek verfügbar
The approved original version of this thesis is available in print at TU Wien Bibliothek.

tilevers mounted to an anchor plate. The three springs are in radial configuration and point towards a keystone weight in the center. The payload is attached to the keystone, putting force on the spring blades. The keystone remains centered as radial spring forces are canceled out by the symmetric configuration of the springs. The vertical spring force is only canceled by the gravitational pull of the keystone and payload.

The anti-spring effect comes into force when the keystone is pulled away from the working point. Due to the geometric configuration of the spring blades, a non-linear spring force is generated which partially cancels the primary spring force (see figure 12). This leads to an effective spring constant near zero when the keystone is close to the working point. The resulting first order mass-spring system can then be used to isolate low frequencies.

The outer mounting points of the springs can be shifted in- or outward to alter the spring tension. Due to the anti-spring design, there are two points of equilibrium for the GAS filter. The working point can be manually switched between the "lower" and "upper" equilibrium. Modifying either spring tension or the weight of the payload also shifts the working point of the filter. As far as small amplitudes are concerned, the behavior of the filter can be linearized around the working point [5, p. 85].

Optimizing the vibration isolation requires setting the resonance frequency of the filter as low as possible. This occurs when the two points of equilibrium overlap fully. With careful tuning, described in section 3.1.4, resonance frequencies of 390 mHz have been reached [5, p. 89].

Both the vertical position of the keystone as well as the resonance frequency depend critically on the spring tension. The aluminum anchor frame and steel spring blades have different expansion coefficients, which makes the GAS filter sensitive to temperature changes. Additionally, spring stiffness can change depending on temperature. Real-world values from the GAS filters used in the Advanced Virgo experiment suggest a position change of $-415\,\mu\mathrm{m\,K^{-1}}$ [5, p. 89]. The thermal response of the prototype GAS filter is investigated in section 3.4.2. These findings indicate that temperature stabilisation will be necessary to achieve the target accuracy, which is discussed in section 3.4.3.

Keeping in mind the goals set in section 1.2, the following sections examine the performance we can expect with the hardware described previously.

3 Performance

The accuracy and repeatability of the measurements taken by the prototype surface measurement device are referred to as its "performance". The results depend critically on multiple factors. Electronic noise, the sensitivity of the detector system, and a number of external factors, such as seismic disturbances and ambient temperature, deteriorate the quality of the measurement. The following sections will give an overview and quantitative analysis of these challenges.

3.1 Position Hold Accuracy

The feedback algorithm used for keeping the measurement gantry at a constant height is based on a proportional-integral-derivative (PID) controller. In the proto-

Die approbierte gedruckte Originalversion dieser Diplomarbeit ist an der TU Wien Bibliothek verfügbar
The approved original version of this thesis is available in print at TU Wien Bibliothek.
TU Bibliothek Your knowledge hub WIEN

type, the reference beam is received by the quadrant sensor (quad.sens.), digitized, and transferred to the PID controller in a virtual LabView environment. Mathematically speaking, the PID controller uses a transfer function of first order to calculate a response to the input waveform recorded by the quad.sens.. The transfer function coefficients must be adjusted to change the system response to the desired effect.

The accuracy with which the measurement gantry can track the reference laser is called the "position hold accuracy". It determines to great extent the precision of the surface measurements. At almost every step along the way, several factors deteriorate the input and response signals of the position hold system.

- Acoustic and seismic noise is picked up by the opto-mechanical components in the signal chain (laser, quad.sens., measurement gantry, etc.). See section 3.1.3 for a detailed characterization.
- Electronic noise is introduced in the analog signal path between sensor and analog-to-digital converter (ADC). The quality of conversion is limited, as expressed by the signal-to-noise ratio (SNR). See section 3.1.2 for a detailed characterization.
- The PID coefficients need to be tuned to avoid intrinsic resonances that would destabilize the system (amplification at resonance), but still need to be aggressive enough to counteract external vibrations.

In our testing, accuracy of the position hold is recorded as an RMS error during normal operation of the LabView program. At each coordinate over the surface-under-test (SUT), the measurement gantry is kept stationary while the feedback mechanism actively maintains the reference height. To calculate the RMS error in the height feedback, the changes in gantry height generated by the PID controller are compared to the mean height.

The PID coefficients can be set using a variety of tuning algorithms. In this case, they are set by the human operator through trial and error and best judgment. Using these optimized coefficients for the feedback, an average RMS accuracy of 192 nm is reached for the position hold.

Any of the deteriorating factors mentioned above may show up in the surface measurements acquired by the interferometer, thereby decreasing precision of the measurement. Compared to the original goal of sub-10 nm precision, it must be noted that this prototype works without any seismic attenuation and using a low-cost quad.sens. and laser source. It is expected that responsiveness, and therefore position hold accuracy, will be further improved with an increase of feedback frequency.

Nevertheless, it is already possible to reliably measure the step between two adjacent mirrors with an accuracy on the order of 20 nm (see section 4.4). These step measurements can be made without relying on the feedback mechanism, as the deformation of the translator stage can be neglected over short distances.

The following sections describe various sources of noise within the measurement setup.

Die approbierte gedruckte Originalversion dieser Diplomarbeit ist an der TU Wien Bibliothek verfügbar
The approved original version of this thesis is available in print at TU Wien Bibliothek.
TU Bibliothek Your knowledge hub WIEN

3.1.1 Relevant Frequency Band (RFB)

In order to obtain a comparative figure for the influence of noise sources, we must first define the band of frequencies that are important to the operation of the experiment. Several amplitude spectra can then be compared by summarizing the displacement over this relevant frequency band (RFB).

According to the preliminary specifications for the upcoming iterations of the measurement device, one data point will be taken each second (1 Hz). This data point derives from averaging the ADC values, which has an acquisition rate of 3000 samples per second (3000 Hz). The position hold algorithm operates at some frequency in between, with a target rate of 1000 Hz.

Therefore, the RFB is limited at 1 to 3000 Hz for the following calculations concerning noise amplitude. The total noise amplitude g^{tot} is calculated by integrating over noise spectrum $g(f)$ within the bounds of the RFB:

$$g^{\text{RFB}} = \sqrt{\int_1^{3000} g^2(f)\mathrm{d}f} \tag{10}$$

3.1.2 Electronic Noise

Even when the measurement setup is most proficiently protected from seismic disturbances, electronic noise in the analog part of the feedback loop still impacts the position hold accuracy.

For purposes of comparison, the spectral distribution of electronic noise (see figure 13) is acquired with the internal ADC (see also figure 3). An additional measurement is made with an external low-noise ADC ("HINF DAQ", with in-device Fourier transformation) while the internal ADC is disconnected, only showing the noise from the analog outputs of the quadrant sensor and its low-noise power supply unit (LNPSU).

The overall level of noise after the ADC stage is critical in the prototype, as it must be supplied by Power over Ethernet (PoE). In this schema, the PoE compatible network switch is receiving power from a switching-mode 48 V AC-to-DC converter, which is then transferred along the data lines to the ADC. Multiple voltage conversions in the power chain, each with its own switch-mode transformer, lead to multiple spikes in the frequency spectrum.

In order to reduce noise in the ADC, ferrite chokes are used on the CAT5 network cables. This does not conform to spec for 10Base-T ethernet, as the ferrites not only suppress unwanted noise but also part of the data signal, which is clocked at 10 MHz. However, data transmission is unaffected in our application, even when using two chokes on the cable (one on each terminal). A much more desirable solution would be to eliminate PoE from the setup. Additionally, critical equipment should be limited to linear power converters, avoiding any switch-mode frequency disturbances – as was done in the design of the LNPSU.

The resulting frequency spectrum is shown in figure 13. The quad.sens. is powered but does not receive any light from the reference beam. Thermal noise which results from line impedance is limited to approximately $5 \times 10^{-8}\,\mathrm{m\,Hz^{-1/2}}$.

The input data is recorded in units of $\mathrm{V\,Hz^{-1/2}}$ and then converted to $\mathrm{m\,Hz^{-1/2}}$. This happens in accordance with the calibration method described in section 3.3.1,

Die approbierte gedruckte Originalversion dieser Diplomarbeit ist an der TU Wien Bibliothek verfügbar
The approved original version of this thesis is available in print at TU Wien Bibliothek.
TU Bibliothek Your knowledge hub WIEN

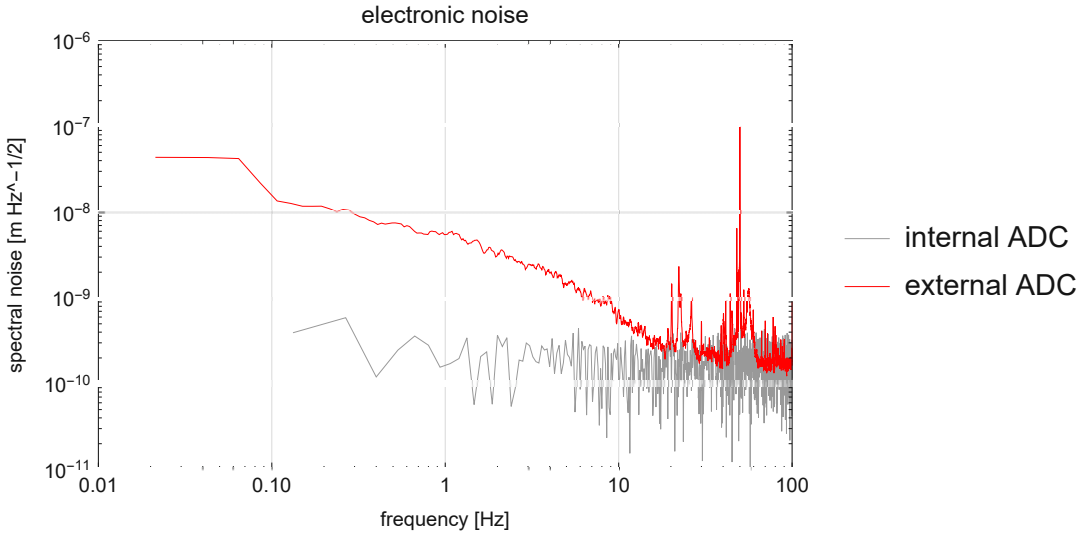

Figure 13: *Electronic noise spectrum of the feedback system in units of* $\mathrm{m\,Hz^{-1/2}}$*, measured with and without connection of the internal ADC. This data includes analog noise from the quad.sens. and LNPSU, and mostly consists of thermal noise resulting from line impedance. When the internal ADC is connected, overall noise is reduced, probably due to better grounding conditions.*

where we find an average conversion factor of $7.5\,\mathrm{mV\,\mu m^{-1}}$. The total error amplitude contributed by the analog electronic circuit is calculated by integrating the noise spectrum inside the RFB. With this, we arrive at a figure of 167 nm RMS for the noise introduced by the quad.sens. and LNPSU. This shows that a majority of the position hold uncertainty is contributed by electronic noise.

3.1.3 Seismic Noise

Seismic noise originates both from inside and outside the experimental setup. For example, cooling compressors, vacuum pumps, or even maintenance work in adjacent floors may cause low-frequency vibrations, which are especially suited to transmission in modern concrete architecture. Even though the lab conditions may be well known, it is difficult to avoid external sources without interfering with regular operation of the surrounding facilities. Other environmental sources, like tidal waves, seismic activity and public transport vehicles, cannot be "turned off" at all. Inside the experiment itself, actuators and motors add disturbances with shorter wavelengths.

In our case the motor of the translator stage only operates between measurements. Thus, external factors contribute the vast majority of seismic noise in the experiment. We are attempting to repeatably produce measurements at nanometer-scale resolution. It becomes clear that any disturbances caused by seismic noise should be minimized to a level below the target accuracy of 10 nm (see section 1.2).

Naturally, the spectrum and total amplitude of seismic noise will be different for different geographic sites. While the current prototype is situated at the Atominstitut (ATI) in Vienna, the next iteration of the surface measurement device is set to be deployed as part of the *q*Bounce experimental setup. There, it will operate under the environmental conditions of the "Niveau D" at the Institut

Die approbierte gedruckte Originalversion dieser Diplomarbeit ist an der TU Wien Bibliothek verfügbar
The approved original version of this thesis is available in print at TU Wien Bibliothek.
TU Bibliothek Your knowledge hub WIEN

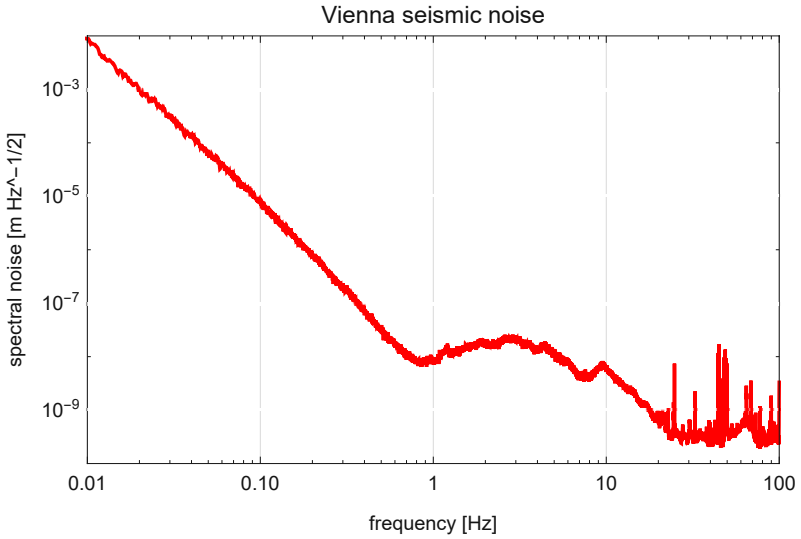

Figure 14: *The spectrum of seismic noise in Vienna is measured using a geophone, in units of* $\mathrm{m\,Hz^{-1/2}}$*. This profile is characteristic for the lab site at ATI.*

Laue-Langevin (ILL) research reactor. As the upcoming vibration compensation system is required to cope with these different situations, we will compare the noise profiles of the two sites in the following sections.

The current prototype at the ATI is decoupled from vibrations in the surrounding building by placing it on top of an optical granite table. Seismic damping is provided by the rubber pads and foam isolators underneath the granite, and by the large weight of the optical table itself. A geophone measurement recorded with a low-noise ADC shows the spectral noise distribution in the Vienna laboratory without considering the noise attenuation of the granite table (see figure 14). From 0.8 to 20 Hz, the spectrum is characteristic of the seismic environment at ATI. In the range above 20 Hz, the background provides a better estimation of the base noise level. Spikes in the frequency spectrum are caused by intermittently operated local machinery, such as vacuum pumps and compressors or the ever-present hum of mains electricity (50 Hz). The spectrum below 0.8 Hz is dominated by "pink" $(1/f)$ noise, generated by integrated electronics and not seismic in origin. The contribution of seismic noise to the measurement error is calculated by integrating the raw amplitude spectrum over the RFB, resulting in a figure of 45.8 nm RMS.

Reaching the goal for position hold accuracy of 10 nm will necessitate passive damping (foam pads, springs, and geometric anti-spring (GAS) filters) to remove the seismic noise from the measurement. The PID feedback mechanism can then be used to further compensate for errors in the translator stage.

In order to predict the level of vibrations that will be encountered at the ILL research reactor, the New High-Noise Model (NHNM) [22] is used as a base estimate. This noise model is based on data from a worldwide network of seismographs and represents the maximum average seismic background activity. Comparing this with spectra recorded in Vienna (see figure 15), the NHNM shows a higher noise level in the range of 5 to 20 Hz. An additional comparison can be made with an earlier on-site measurement in Grenoble [10, p. 17], which stays well below the NHNM and fitted curve, although the sensitivity of the OROS vibrometer is insufficient to cover the full seismic background. Seismic noise at Grenoble is shown to vary over

Die approbierte gedruckte Originalversion dieser Diplomarbeit ist an der TU Wien Bibliothek verfügbar
The approved original version of this thesis is available in print at TU Wien Bibliothek.
TU Bibliothek Your knowledge hub WIEN

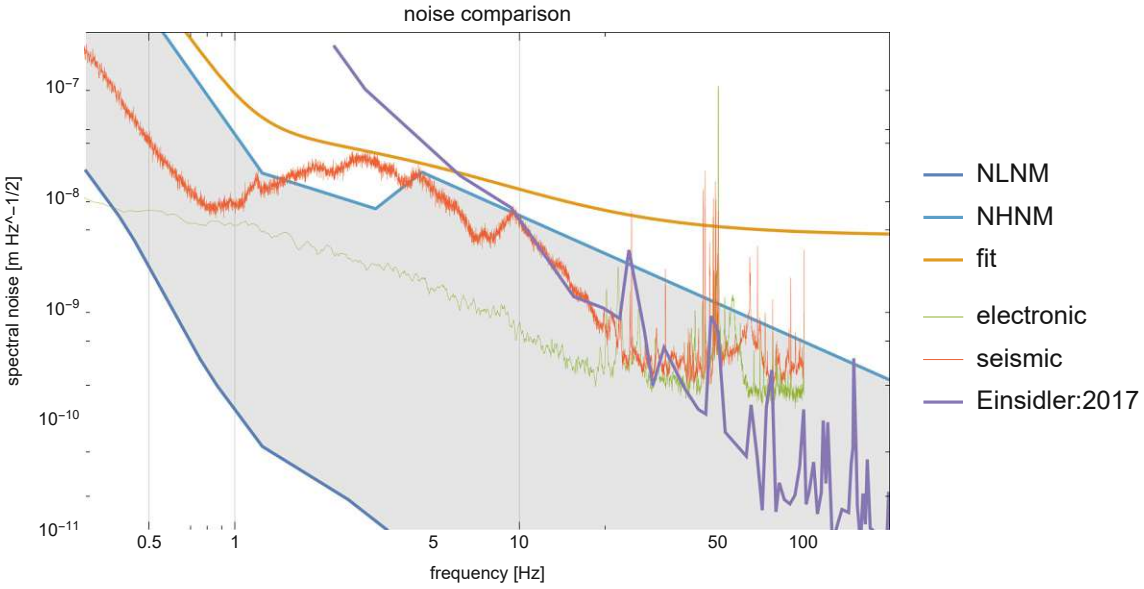

Figure 15: *Electronic (fig. 13) and seismic noise (fig. 14) in the prototype is compared to the global [22] noise models (high noise NHNM and low noise NLNM) and an earlier measurement at the Grenoble site "Einsidler:2017" [10, p. 17]. This is used to construct a fit function representing the worst-case noise at the Grenoble site. All curves in units of* $\mathrm{m\,Hz^{-1/2}}$.

the course of multiple days [10, p. 19]. All of this is taken into consideration when modelling the worst-case fit function (also shown in figure 15), which assumes a noise level even higher than the NHNM. Evaluating this fit function over the RFB, we arrive at an estimated error amplitude of 256 nm RMS for the setup at ILL.

The calculated noise levels for the ATI and ILL are compared in table 2. It becomes evident that the system for seismic isolation needs to provide an attenuation of at least 28.2 dB over the RFB in order to achieve an accuracy below 10 nm. Seeing as common spring suspension would be unwieldy, this provides the most pressing argument for the high-performance passive isolation provided by GAS filters. In the following section, a mathematical model for a GAS filter will be established. It can be shown that with reasonable parameters, the attenuation of the filter is sufficient to reach the target accuracy. For a mechanical description of the GAS filter, see

	noise scenario	fig.	RMS error [nm]	comparison [dB]
	accuracy goal	–	10	0
Grenoble	worst-case model	15	256	28.2
	w/ GAS filter	18	11.4	1.1
Vienna	seismic	14	45.8	13.2
	w/ GAS filter	–	3.85	−8.3
	electronic	13	108	20.7
	DeltaSens	19	0.0493	−46.1

Table 2: *Comparison of noise levels within the RFB (*$1-3000\,\mathrm{Hz}$*) as found in various settings. This represents the error of position hold (RMS)* without *active feedback. The rightmost column shows decibel values compared to the goal for measurement accuracy of* 10 nm *or less.*

Die approbierte gedruckte Originalversion dieser Diplomarbeit ist an der TU Wien Bibliothek verfügbar
The approved original version of this thesis is available in print at TU Wien Bibliothek.
TU Bibliothek Your knowledge hub WIEN

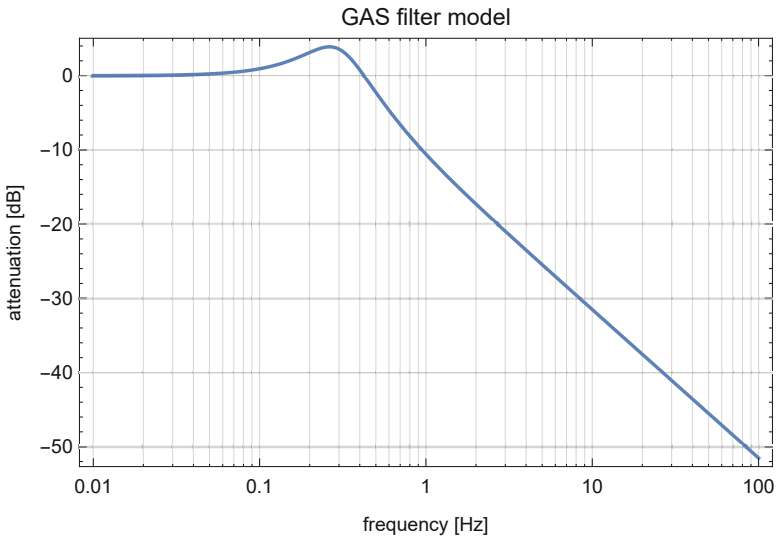

Figure 16: *Bode plot of the transmission model for the GAS filter (equation 11). Signals are attenuated by* 20 dB *per decade, similar to a first order filter. This model has a resonance frequency* $f_0 = 0.3\,\mathrm{Hz}$*, mass of keystone* $m = 0.2\,\mathrm{kg}$*, and damping coefficient* $\gamma = \frac{1}{3}$*.*

section 2.7.

3.1.4 GAS Filter Calibration

The next iteration of the measurement setup aims to reduce mechanical vibrations through passive mechanical isolation. The attenuation system is to be tuned such that its resonance frequency lies outside of the RFB, meaning that the resonance should be well below 1 Hz. In our case, GAS filters are the most sensible choice because they offer very low resonance frequencies at a small form factor (see figure 11). They have proven reliable in a number of gravitational wave experiments [3–5].

For predicting what amount of attenuation can be achieved, we model the transmission function with

$$T_{\mathrm{GAS}}(\omega) = \frac{\omega_0^2 - \frac{i\gamma\omega}{m}}{\omega_0^2 - \omega^2 - \frac{i\gamma\omega}{m}}, \tag{11}$$

where $\omega_0 = 2\pi f_0$ and $\omega = 2\pi f$ and with the resonance frequency $f_0 = 0.3\,\mathrm{Hz}$, mass of keystone $m = 0.2\,\mathrm{kg}$, and damping coefficient $\gamma = \frac{1}{3}$. This equation is similar to [3, p. 125]. Above the resonance peak, disturbances are attenuated with 20 dB per decade, similar to a first order low-pass filter (Butterworth). The resulting Bode plot is shown in figure 16.

The resonance frequency f_0 of the GAS filter is strongly dependent on the stiffness of the spring blades and the mass of the keystone. Spring stiffness is changed by moving the blade mounts in- or outward (see section 2.7), but it also changes with the temperature of the blades (see section 3.4.2). The mass is altered by adding or removing small masses ($< 1\,\mathrm{g}$) on top of the keystone.

Because of the special geometric construction, the GAS spring has two points of equilibrium. The closer (spatially) these two points are to each other, the lower the resonance frequency becomes. The resonance frequency is minimized as follows, using a process of iterative tuning: First, the weight of the keystone is changed

Die approbierte gedruckte Originalversion dieser Diplomarbeit ist an der TU Wien Bibliothek verfügbar
The approved original version of this thesis is available in print at TU Wien Bibliothek.
TU Bibliothek Your knowledge hub WIEN

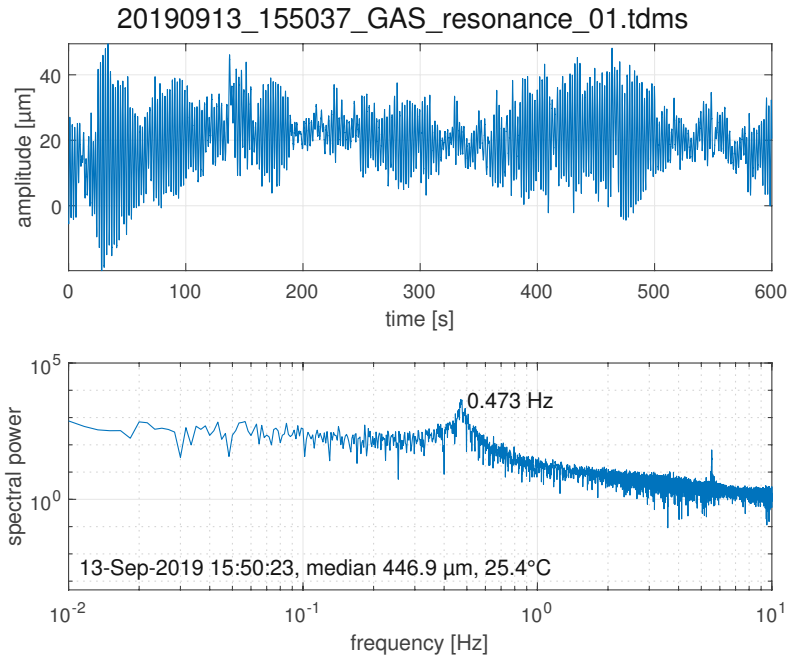

Figure 17: *Results from a sample measurement of GAS filter resonance. The keystone starts oscillating by itself due to external vibrations. The displacement values (shown in the upper plot) are subjected to FFT analysis, yielding a diagram of the spectral oscillation power over each frequency. The resonance frequency is easily recognised as the coordinate of peak spectral power. Note that the amplitude varies in the range of* 50 µm*, whereas target accuracy is* 10 nm*.*

and the resonance frequency is measured. This is repeated until a local minimum frequency is reached. Then, the stiffness of the spring is adjusted by moving the blade mounts, and the process begins anew. The adjustment to the blade tension should become smaller and smaller with each iteration. Great attention should be paid to the temperature of the GAS filter. Even a change of 0.5 °C in the ambient temperature, e.g. caused by the presence of a human experimenter, results in a shift of the resonance frequency (see section 3.4.2).

The resonance frequency of the GAS filter can be most effectively observed through measuring the vertical excursions of the keystone for multiple cycles. Once the resonance is tuned to be in the 500 mHz range, this can take several minutes. Fourier analysis of the measurement will yield a spike in the spectrum which corresponds to the resonance frequency. In practice, the laser interferometer (DeltaSens) is used in absolute (DC) mode with a fiber sensor mounted above the reflective keystone. A recording interval of 600 s is chosen for adequate resolution of the resonance peak. The keystone does not need any additional excitation to start oscillating because air drafts and vibrations in the environment already provide enough of an impulse. In fact, in a test measurement (see figure 17) the amplitude varies in the range of 50 µm, whereas target accuracy is 10 nm. Luckily in the vacuum environment of *q*BOUNCE, air drafts are eliminated.

We can calculate the effect of the GAS filter by convolving the worst-case noise estimate for the Grenoble site with the transfer function of the GAS filter (eq. 11). The Grenoble base model and the attenuated curve are compared in figure 18. The

Die approbierte gedruckte Originalversion dieser Diplomarbeit ist an der TU Wien Bibliothek verfügbar
The approved original version of this thesis is available in print at TU Wien Bibliothek.
TU Bibliothek Your knowledge hub WIEN

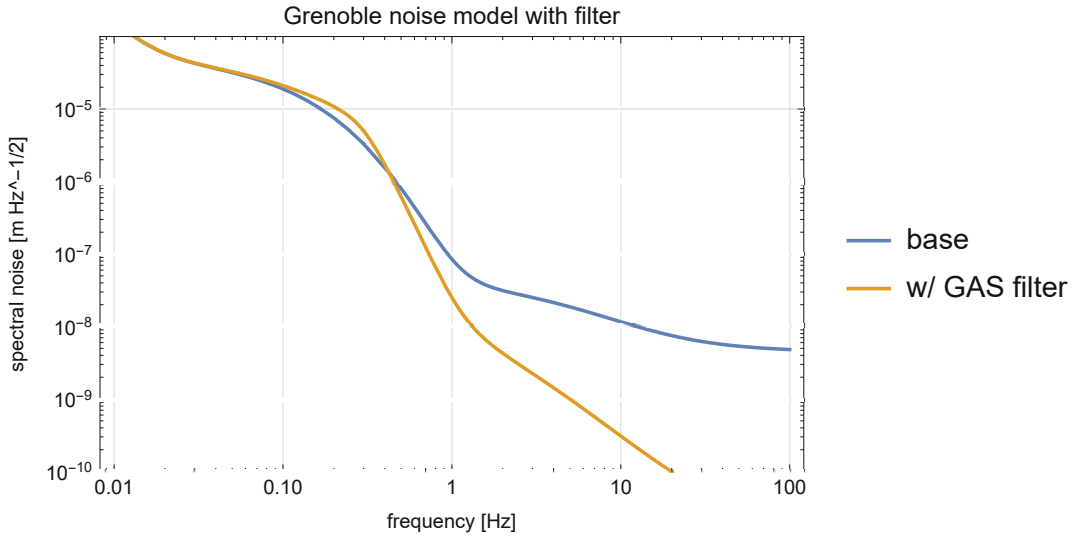

Figure 18: *Comparison of the Grenoble base model and attenuated noise spectrum, in units of* $\mathrm{m\,Hz^{-1/2}}$*. When the GAS filter model (eq. 11) is applied to the Grenoble noise estimate (see ch. 3.1.3), the noise amplitude within the RFB can be reduced from* 256 *to just* 11.4 nm *RMS.*

resonance peak at 0.3 Hz is deliberately chosen to avoid the measurement bandwidth. The noise over the RFB amounts to 11.4 nm RMS, which is an overall 27 dB lower than the base estimate for Grenoble.

3.2 DeltaSens Instrument Noise

In order to determine the signal-to-noise ratio of the DeltaSens interferometric measurement device, the noise floor is measured under static conditions. A cleaved fiber is mounted to an optical post on a granite table. At a distance of approximately 1 mm, a static reflective surface is clamped to the base. The instrument noise is then evaluated by recording the signal fluctuations of the interferometer over a duration of 10 min.

The resulting data is subjected to an FFT analysis in order to retrieve the spectral magnitudes, shown in figure 19.

At a frequency of 100 mHz, DeltaSens shows a spectral noise of $1\,\mathrm{nm\,Hz^{-1/2}}$, which decreases with increasing frequency. Over the RFB the contributed error is just 49.3 pm, or 46 dB below the target accuracy of 10 nm.

3.3 Optical System

The optical system of the prototype consists of a laser pointer with a circular Gaussian beam output, a concave broadband mirror (reflector) and the position-sensitive quadrant detector (quad.sens.).

The latter produces an analog output that is proportional to the amount of vertical deflection, as described in section 2.6. This output can be further amplified electronically, only limited by the noise floor of the electronics. Electronic noise in the prototype is discussed in section 3.1.2. The analog signal is sent to an ADC and can be converted to a length scale by prior calibration.

Die approbierte gedruckte Originalversion dieser Diplomarbeit ist an der TU Wien Bibliothek verfügbar
The approved original version of this thesis is available in print at TU Wien Bibliothek.
TU Bibliothek Your knowledge hub WIEN

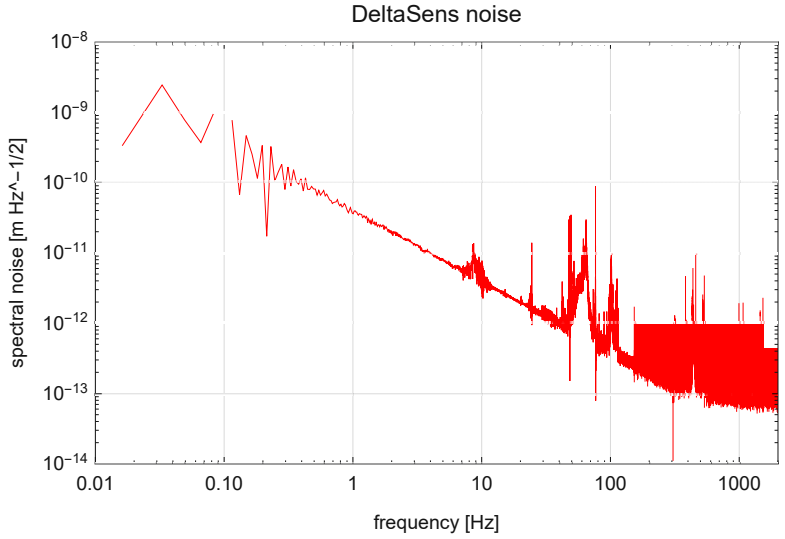

Figure 19: *Spectrum of background noise for the DeltaSens instrument in units of* $\mathrm{m\,Hz^{-1/2}}$*. This was captured with a cleaved optical fiber attached to the laser output, while the setup was situated on top of the optical granite used for testing the prototype. The seismic noise of the mounting post and granite has not been subtracted.*

The concave mirror is responsible for amplifying the Z-offset of the measurement gantry geometrically as part of the optical lever design. As we will see (section 3.3.2), the amplification is dependent on the offset and angle of the incoming reference beam.

3.3.1 Calibration of the Quadrant Detector

The quad.sens. consists of four photodiodes and an internal amplifier (see section 2.6). It produces an analog output voltage that is proportional to the position of the laser beam on its sensitive area, where 0 V represents a perfectly centered beam. We are interested in measuring the offset in the Z-axis, which is derived from the difference of light input on the top and bottom half of the detector. For a given de-centering of the input beam, a certain output voltage is generated on the "X" or "Y" output of the quadrant sensor. The conversion coefficient between the voltage and length scale is given in $\mathrm{V\,m^{-1}}$ (or $\mathrm{mV\,\mu m^{-1}}$) and will be called "sensitivity" hereafter.

Several factors influence the sensitivity of the detector in the test setup:

- When the **laser power** is lowered, sensitivity decreases. This is a result of reduced contrast on the detector and might occur when using a weaker power source or reducing the electrical current to the laser diode. Additionally, the laser diode has a non-linear characteristic.

- Different intensity distributions (beam profiles) of the incoming light change sensitivity, as well. Considering the contrast between the sensor quadrants, there exists an optimal **spot diameter** for a Gaussian circular beam which maximises the amplitude of the output signal. Since the optics of the reference laser have a focus point, the spot diameter changes constantly when the

Die approbierte gedruckte Originalversion dieser Diplomarbeit ist an der TU Wien Bibliothek verfügbar
The approved original version of this thesis is available in print at TU Wien Bibliothek.
TU Bibliothek Your knowledge hub WIEN

measurement gantry is moved. Thus, the sensitivity changes with the position of the translator stage.

- The concave reflector enlarges the deflection amplitude on the sensor by **geometric amplification** which increases sensitivity. The local surface gradient of the reflector is different depending on the point of incidence of the reference beam, thus Z-axis deflection affects geometric amplification. Sensitivity also changes for different tilts of the reflector (or the incoming beam, respectively). These phenomena are discussed in section 3.3.2.

  In the one-dimensional feedback mechanism of the prototype, any off-axis tilts cause erroneous shifts in the height of the measurement gantry, thus changing the geometric amplification factor (see section 4.2). This can be easily remedied by introducing a three-dimensional feedback system, as proposed for the next version of the prototype.

As a result, the calibration procedure needs to measure the sensitivity of the quad.sens. at multiple positions along the rail of the translator stage: first, the measurement gantry is moved to the X-coordinate in question. The piezo table is then raised and lowered to two Z-coordinates using its internal capacitive sensors as a reference. The change in piezo position Δz is then compared to the analog output values of the quad.sens. ΔV, and the sensitivity is calculated as $s = \frac{\Delta V}{\Delta z}$. This works well as long as the reference beam does not leave the active region of the sensor, which is defined as the X, Y outputs staying below $\pm 80\,\%$ of the SUM signal level.

For the configuration found in the prototype, typical values are in the range of 5 to $10\,\mathrm{mV\,\mu m^{-1}}$. For further calculations, a value of $7.5\,\mathrm{mV\,\mu m^{-1}}$ is used. The table resulting from the calibration measurement allows for interpolation or fitting of the sensitivity at every point along the linear stage, as long as the original data points are reasonably dense. The conversion between voltage and distance directly enters into the P-coefficient of the PID feedback algorithm. Additionally, these figures can later be used to make predictions about the accuracy and stability of the system. The voltage-distance conversion is also used to determine the tilt and offset of the translator stage, as discussed in section 4.2.

3.3.2 Sensitivity Change of the Curved Mirror Under Tilt and Offset

Both the position of the laser beam as well as the angle of incidence on the concave reflector have an impact on the overall sensitivity of the system. Take for example the situation depicted in figure 20. A concave spherical mirror with a radius of $R = 75\,\mathrm{mm}$ is placed at a distance of $L = 120\,\mathrm{mm}$ from the quadrant detector. In the mirror coordinate system, the X-axis is identical to the optical axis of the mirror, and the Z-coordinate describes the distance to the optical axis in the observed cross-section. Equations 12a–12c describe the surface and gradient of the mirror in this X-Z-plane. The laser beam meets the mirror surface at the distance z_1 from the optical axis under the angle β and is reflected onto the quadrant sensor. The exit angle $2\alpha + \beta$ results from the local gradient of the mirror α and the tilt of the incoming beam β. As α changes with the off-axis distance z_{in}, any deflection or tilt (β) incurs a change in the displacement z_{out} of the reflected beam.

Die approbierte gedruckte Originalversion dieser Diplomarbeit ist an der TU Wien Bibliothek verfügbar
The approved original version of this thesis is available in print at TU Wien Bibliothek.
TU Bibliothek Your knowledge hub WIEN

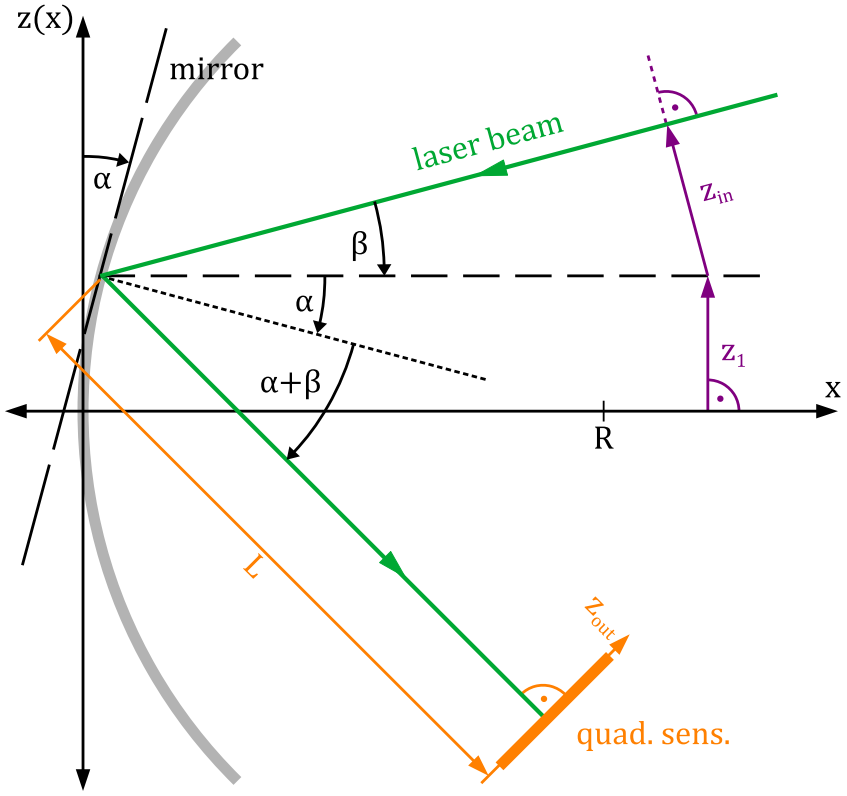

Figure 20: *Geometry for calculating mirror sensitivity under tilt and offset of the reference laser beam. A concave spherical mirror is placed at distance L from the quad.sens.. Eq. 12a and 12c describe the surface and gradient of the mirror. The laser beam (green) meets the mirror surface at the distance z_1 from the optical axis (dashed) under the angle β and is reflected onto the quad.sens..*

Die approbierte gedruckte Originalversion dieser Diplomarbeit ist an der TU Wien Bibliothek verfügbar
The approved original version of this thesis is available in print at TU Wien Bibliothek.

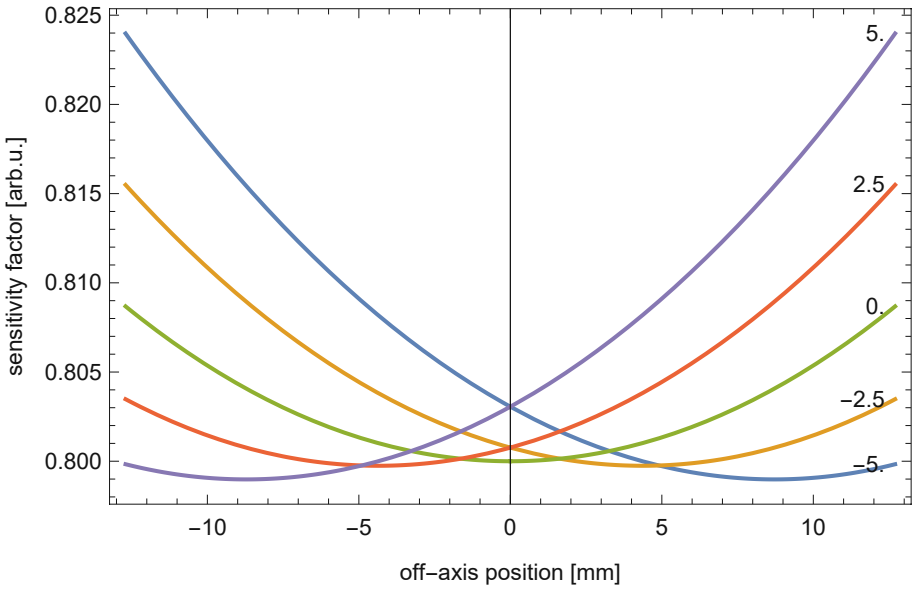

Figure 21: *Sensitivity of the reflector-sensor system changes for different tilts β (labeled on the right side in units of degrees) of the incoming laser beam. The X-axis represents the distance to the optical axis of the reflector mirror.*

$$R^2 = (x(z) - R)^2 + z^2, \tag{12a}$$

$$x(z) = R \pm \sqrt{R^2 - z^2}, \tag{12b}$$

$$\tan\alpha(z_1, \beta) = \frac{\partial}{\partial z} x(z_1 + z_{\text{in}} \cos\beta), \tag{12c}$$

$$z_{\text{out}} = L \tan(\alpha(z_1, \beta) + \beta) \tag{12d}$$

From this simple system of equations, we obtain the geometric magnification factor m_z by forming the derivative of the output displacement z_{out} with respect to the input displacement z_{in}.

$$\begin{aligned} m_z(z_1, \beta; z_{\text{in}}, R, L) = \frac{\partial z_{\text{out}}}{\partial z_{\text{in}}} &= \frac{L}{b} \cos(\beta) \sec^2\left(\beta + \arctan\frac{b}{a}\right), \\ a &= \sqrt{R^2 - b^2}, \\ b &= z_1 + z_{\text{in}} \cos(\beta) \end{aligned} \tag{13}$$

The resulting function m_z depends on the initial offset z_1 and incident angle β. The overall sensitivity primarily depends on the curvature R of the mirror.

The change in the geometric magnification factor (and therefore sensitivity) dependent on the off-axis distance z_1 is shown in figure 21. Any tilt β in the reference beam or reflector itself results in a tilted magnification curve. Tilting the mirror also shifts the point of highest sensitivity outward from the optical center towards the direction of tilt. Increasing the off-axis distance z_1 effectively produces a steeper mirror gradient, thus increasing the magnification factor. However, as can be seen in figure 21, the influence of different tilts β is limited to a few percentage points.

Die approbierte gedruckte Originalversion dieser Diplomarbeit ist an der TU Wien Bibliothek verfügbar
The approved original version of this thesis is available in print at TU Wien Bibliothek.
TU Bibliothek Your knowledge hub WIEN

3.4 Temperature Effects

Any change in ambient temperature has significant impact on the hardware setup. In this section, we will look at the thermal expansion of the measurement and reference cube. We will show that this effect is evident in long-term measurements and reflects in the amount of compensation needed to maintain the reference height. In a later section, the "thermal expansion" of a GAS filter is discussed. Using a simple structural model of the hardware setup, we can propose requirements on temperature stability during measurements.

The equation for thermal expansion of an isotropic material with the length L_0 is [9, p. 260]:

$$L(T) = L_0 + \Delta L(T) = (1 + \alpha_L)\Delta T L_0 \tag{14}$$

We are making the assumption that the material is isotropic and that the coefficient of expansion does not change with temperature, $\alpha_L(T) = \text{const}$.

For this calculation, we are only interested in length expansion (eq. 14) rather than volumetric expansion. The coefficient α_L is different for each material and can be obtained from tabulated sources. Most structural parts of the prototype are built from aluminum (Al), including the mirror holder and gantry, but the translator stage is made from steel (V2A). The coefficient $\alpha_L^{\text{Al}} = 23.5 \times 10^{-6}\,\text{K}^{-1}$ [13, p. 7] is valid at the reference temperature of 20 °C and describes the relative longitudinal expansion of aluminum (Al 99.5, EN AW-1050A). Under the same conditions, the coefficient for V2A grade steel is $\alpha_L^{\text{V2A}} = 16 \times 10^{-6}\,\text{K}^{-1}$ [9, p. 260].

3.4.1 Temperature Drift During Long-Term Measurements

Thermal expansion of the reference cube is not corrected in the current prototype setup. This means that when the feedback loop is active, the measurement gantry will follow the change in reference height. On the other hand, this makes it possible to estimate the temperature change in the laboratory environment through observing the height difference between the two cubes.

The laser cube emits the reference beam at a height of 195 mm above the granite surface (see figure 22). Since it is constructed completely out of aluminum parts, we can easily estimate the thermal expansion as a change in height of the reference beam.

Likewise, the measurement cube, which is also constructed from aluminum extrusions, has a height of 440 mm. The piezo and measurement gantry are attached upside-down to the translator stage inside the top of the cube. All parts are made of aluminum, with the exception of the translator stage which contributes 40 mm in height. We shall assume equal temperature of all parts of the experiment. Using equation 14 and the appropriate coefficients $\alpha_L^{\text{Al}}, \alpha_L^{\text{V2A}}$ results in a thermal expansion of $5.38\,\mu\text{m}\,\text{K}^{-1}$ for this mechanical configuration.

Figure 23 shows the results of an early test of the feedback mechanism. The experiment is configured as shown in figure 3. Then, the piezo is moved in accordance with the voltage output from the quad.sens. in order to keep the gantry at the height referenced by the laser beam. Its internal capacitive sensors (cap.sens.) are used to measure the height correction applied by the feedback.

The measurement gantry is moved to a total of 56 positions along the rail. At each position, the gantry stops and waits for the feedback to stabilize the height,

Die approbierte gedruckte Originalversion dieser Diplomarbeit ist an der TU Wien Bibliothek verfügbar
The approved original version of this thesis is available in print at TU Wien Bibliothek.
TU Bibliothek Your knowledge hub WIEN

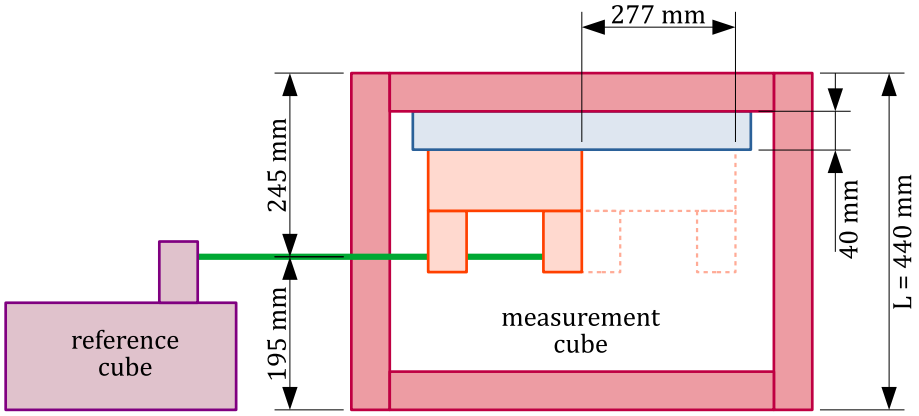

Figure 22: *Schematic view of the model for thermal expansion in the prototype. The reference laser is mounted on the reference cube (left). Both cubes are constructed exclusively out of aluminium, while the translator stage (blue) mounted inside measurement cube (right) is made from V2A steel. Due to the different height of the cubes, ambient temperature changes can be reconstructed by observing the long-term vertical shift in the feedback loop.*

after which an average is taken of the Z-position reported by the cap.sens.. This measurement mode takes 1.5 h to move the entire length of the rail from position 0 to 277 mm. In total, there were 15 measurement passes along the rail, spanning a time of 22.5 h. Although the laboratory is air-conditioned, temperatures are lower during the night hours due to the lack of solar irradiation through the windows.

Figure 23 shows the same data plotted separately for a selection of positions along the length of the translator stage. The extreme ends of the rail (0, 252 mm) seem to be more susceptible to a temperature shift than the group of middle positions (50, 101, 151, 201 mm). The thermal expansion at position 151 mm covers a range of 23.22 µm, which corresponds to a temperature change of 4.3 K.

As discussed above, a temperature change of 4.3 K can be observed over the course of a day-night cycle in the laboratory. Neither the thermal expansion of the reference cube nor the measurement cube is compensated. This leads to both a loss of absolute reference, and a relative deviation of 23.22 µm due to the different heights of the cubes. The relative deviation is well within the piezo range of 100 µm, however, it is also several orders of magnitude larger than the accuracy goal of the surface measurement ($\sigma \leq 10$ nm). To mitigate the effect of thermal expansion, active and passive temperature stabilization of the reference cube will be necessary. Additionally, speeding up the measurement helps to avoid longer-term temperature fluctuations, but in turn requires vibration isolation to reduce the measurement noise.

3.4.2 Measurement of GAS Filter Temperature Drift

In the next iteration of the mirror measurement, the reference laser and measurement cube will be mounted to separate systems for damping low-frequency vibrations. This is achieved by using a combination of rubber pads (high frequency) and low-frequency GAS filters. One drawback to the use of GAS filters is their high responsiveness to temperature changes.

GAS filters (see section 2.7) are constructed from a combination of different ma-

Die approbierte gedruckte Originalversion dieser Diplomarbeit ist an der TU Wien Bibliothek verfügbar
The approved original version of this thesis is available in print at TU Wien Bibliothek.
TU Bibliothek Your knowledge hub WIEN

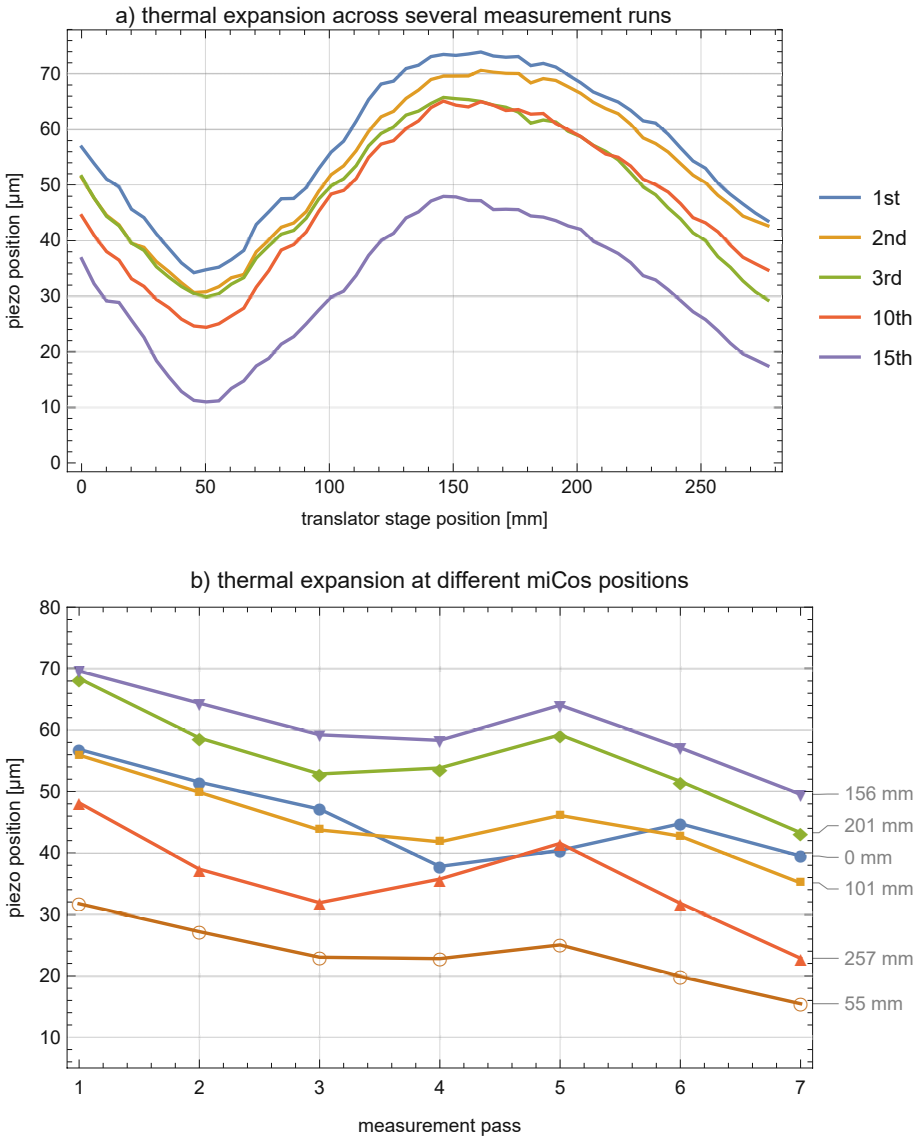

Figure 23: *Thermal expansion is affecting the results of an early test of the feedback mechanism.*
a) *The legend on the right shows the number of each measurement pass. After the height is stabilized via laser feedback, the internal sensors measure the position of the piezo, which equals the correction applied to the translator stage. This is measured across 56 points, repeatedly covering the movement range for a time span of* 22.5 h. *The reference laser shifts through thermal expansion which results in the gantry moving up and down. The continuing temperature changes can be observed by the gradual deviation between measurements.*
b) *The same data is plotted for a selection of positions along the rail. Despite some small outliers, the temperature shift across this group of positions appears uniform. The change in height roughly corresponds to a change of* 4.3 K *in ambient temperature.*

Die approbierte gedruckte Originalversion dieser Diplomarbeit ist an der TU Wien Bibliothek verfügbar
The approved original version of this thesis is available in print at TU Wien Bibliothek.

terials with different thermal coefficients. The main body and keystone are made from aluminum, while the spring blades are cut from spring steel. The different expansion of spring blades and frame lead to a change in blade compression, which affects the stiffness of the filter [5, p. 89]. The equilibrium position is also dependent on the weight of the payload attached to the keystone. Additionally, material properties of the spring may change at different temperatures. To get a sense of the overall effect, it is easiest to represent the thermal expansion of the GAS filter via the distance the keystone is displaced from the original working point. This way, the different expansion coefficients need not be taken into consideration.

We shall provide an exact figure by examining a GAS filter which is representative of the size and configuration used in the upcoming implementation of the measurement system (see figure 11). Using the fiber interferometer (DeltaSens) in absolute distance (DC) mode, it is possible to cross-reference the displacement of the keystone with the room temperature from a datalogger using timestamps.

In the laboratory, a large temperature gradient is induced by shutting off the air-conditioning. According to the temperature log, this increases the ambient temperature by approximately 2 °C over the span of one hour. The resulting change in keystone position and resonance frequency during this period is shown in figure 24a. The data are then subjected to a linear least-squares fit, which shows a temperature coefficient of $\alpha_L^{\mathrm{GAS}} \cdot L^{\mathrm{GAS}} = 0.993 \times 10^{-3}\,\mathrm{m\,K^{-1}}$. For comparison, the thermal expansion of GAS filters used in the Virgo experiment is reported as $\alpha_L^{\mathrm{GAS}} \cdot L^{\mathrm{GAS}} = -0.415 \times 10^{-3}\,\mathrm{m\,K^{-1}}$ [5, p. 89]. For the purposes of our estimations, we assume this coefficient to be linear around the working point, which is established during the fine-tuning of the GAS filter.

Additionally, the same data also shows that the change in equilibrium position slowly shifts the keystone away from the optimal working point. Thus the resonance frequency increases by $\mathrm{d}f/\mathrm{d}T = 31.3 \times 10^{-3}\,\mathrm{Hz\,K^{-1}}$ (see figure 24b).

3.4.3 Limit on Thermal Stability of the Reference Cube

The thermal expansion of the laser gantry causes a loss of absolute reference in any long-term measurements (see section 3.4.1). As mentioned before, time is an important factor as the temperature change becomes insignificant when the duration of the measurement is short enough.

As a rough estimate of the worst-case measurement duration we can assume a mirror size of 600×250 mm^2, according to the goals specified in section 1.2. When taking a measurement every 15 mm, the surface map would contain around 670 points. However, the measurement gantry has sensors at multiple points that can be queried simultaneously, so that the number of measurement is diminished by a factor of 2–3. Assuming that each measurement takes 1 s and the travel time between points is 15 s (at $1\,\mathrm{mm\,s^{-1}}$), acquisition of the whole surface map would take close to $t = 1\,\mathrm{h}$.

$$t = \frac{600 \times 250}{15^2 \times 3} \times (1 + 15) = 3555\ \mathrm{s}$$

We shall require that the drift in measured height during the measurement stays below 100 nm. This limit applies only to the laser reference, since the feedback algorithm will cause the measurement gantry to follow any offset in the reference. Taking into consideration a simple model of the reference cube, we can estimate

Die approbierte gedruckte Originalversion dieser Diplomarbeit ist an der TU Wien Bibliothek verfügbar
The approved original version of this thesis is available in print at TU Wien Bibliothek.
TU Bibliothek Your knowledge hub WIEN

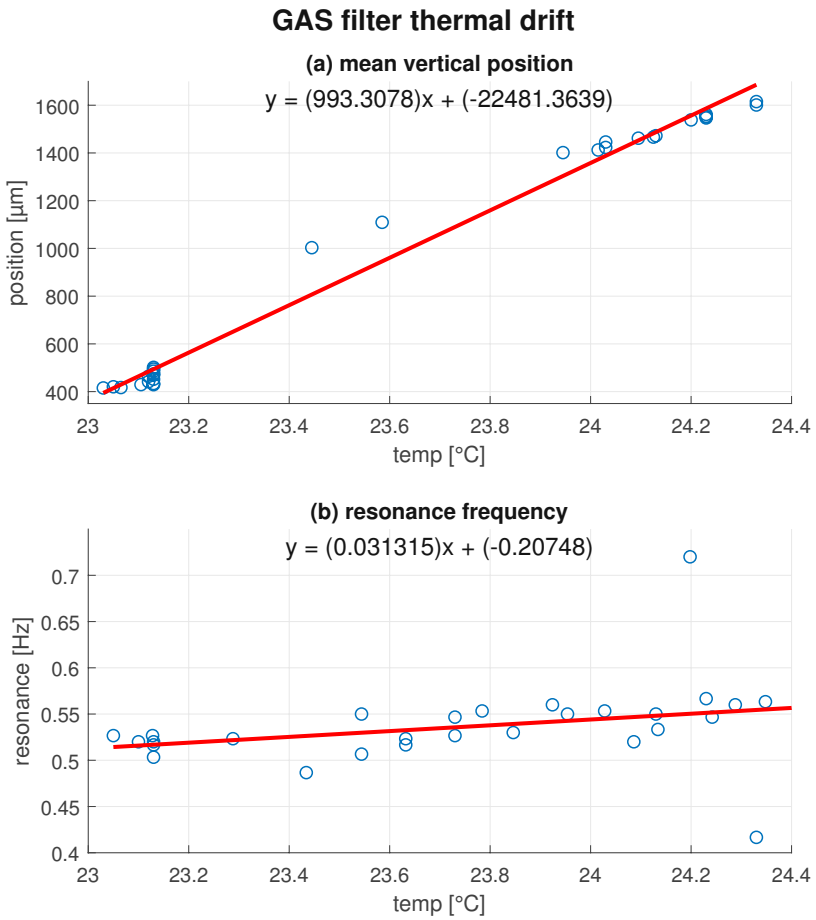

Figure 24: *Thermal expansion of a typical configuration of the GAS filter. The equilibrium position and damping properties depend on the spring stiffness and weight of the payload. The displacement of the keystone is measured by a fiber interferometer capable of capturing absolute distances (DeltaSens in DC mode). The data are then a subjected to a linear fit to extract the temperature coefficient. Due to the keystone shifting away from the optimal working point, the resonance frequency increases as well.*
The data presented in this figure originate from a different measurement than those in figure 17.

Die approbierte gedruckte Originalversion dieser Diplomarbeit ist an der TU Wien Bibliothek verfügbar
The approved original version of this thesis is available in print at TU Wien Bibliothek.

the maximum allowable temperature change per hour. In the estimation, we assume that the laser module to be attached to an aluminum gantry with a height of $L^{\mathrm{Al}} = 300\,\mathrm{mm}$, which in turn is mounted onto a GAS filter for mechanical isolation. Thermal expansion is given by the following simple formula:

$$\Delta z = \left(\alpha_L^{\mathrm{Al}} \cdot L^{\mathrm{Al}} + \alpha_L^{\mathrm{GAS}} \cdot L^{\mathrm{GAS}}\right) \Delta T \tag{15}$$

We shall assume the thermal expansion measured as before (see section 3.4.2, $\alpha_L^{\mathrm{GAS}} \cdot L^{\mathrm{GAS}} = 0.993 \times 10^{-3}\,\mathrm{m\,K^{-1}}$). Solving this for ΔT and using the aforementioned coefficients returns a limit of

$$\Delta z^{\mathrm{laser}} \leq 100\,\mathrm{nm} \longleftrightarrow \Delta T \leq 1.0 \times 10^{-4}\,\mathrm{K\,h^{-1}}$$

This figure applies to the whole of the aluminum structure as well as the GAS filter. However, the considerable size of the experimental apparatus (see figure 3) makes it more difficult to maintain precise and uniform temperature control. As the expansion factor for aluminum is much smaller than the temperature response from the GAS filter, it can be argued that stabilisation of the latter is much more critical. Focusing on the temperature stabilisation of the GAS filter will increase the target range for the temperature of the aluminum structure. This should simplify the overall stabilisation efforts.

Equation 15 can be expanded to represent two different stabilisation limits for the reference cube ΔT^{Al} and GAS filter ΔT^{GAS}:

$$\Delta z = \alpha_L^{\mathrm{Al}} \cdot L^{\mathrm{Al}} \cdot \Delta T^{\mathrm{Al}} + \alpha_L^{\mathrm{GAS}} \cdot L^{\mathrm{GAS}} \cdot \Delta T^{\mathrm{GAS}} \tag{16}$$

Applying the modified temperature stabilisation requirement ΔT^{Al}, we can conclude

$$\Delta z^{\mathrm{laser}} \leq 100\,\mathrm{nm}, \Delta T^{\mathrm{Al}} \leq 1 \times 10^{-3}\,\mathrm{K\,h^{-1}} \longleftrightarrow \Delta T^{\mathrm{GAS}} \leq 9.4 \times 10^{-5}\,\mathrm{K\,h^{-1}}$$

This shows that easing the stabilisation burden for the reference cube by one order of magnitude ($0.1 \rightarrow 1 \times 10^{-3}\,\mathrm{K\,h^{-1}}$) can be counteracted by tightening the stabilisation limits of the GAS filter by only about 6 %.

Any speed-up in measuring the mirror surface directly translates in less stringent requirements for temperature stability. At the moment, the greatest improvements are possible by improving the position hold capability of the feedback loop. The travel time between each measurement point is dictated by the stability of the interferometer signal which in turn depends on a stable measurement gantry. The high-frequency feedback loop in the upcoming iteration of the measurement setup should be able to address this problem.

3.4.4 Limit on Thermal Gradient in the Measurement Gantry

The thermal drift of the measurement gantry is only required to stay within range of the piezo actuator, which results in a considerably larger margin for stability. In order to calculate the upper limit on the allowable temperature drift, we will assume that the two ends of the translator stage are mounted to independent aluminum extrusions, each with a GAS filter. If the two ends of the translator stage have

Die approbierte gedruckte Originalversion dieser Diplomarbeit ist an der TU Wien Bibliothek verfügbar
The approved original version of this thesis is available in print at TU Wien Bibliothek.
TU Bibliothek Your knowledge hub WIEN

a temperature difference of ΔT, a tilt is introduced into the measurement gantry, which needs to be compensated by the piezo.

We will take as an example the current prototype setup described in section 2. The piezo actuator has a Z range of 100 µm and a maximum tilt of 1.4 mrad, and the translator stage has a movement range of 277 mm. When maximum tilt is applied to the piezo, the ends of the translator stage have a height difference equal to 388 µm. This is much larger than the Z range of the actuator, so that the latter applies as the more stringent criterion.

Under practical considerations, the Z range usable for temperature drift correction is reduced by compensation of tilt and offset of the translator stage (see section 4.2). Let us (arbitrarily) assume that the stage corrections only use 75 % of the total available range, leaving us a maximum of 25 µm to compensate for thermal expansion.

Using equation 15 again, we can interpret ΔT as the temperature difference between the two ends of the measurement cube (see figure 22), and Δz as the limit on the height difference. The limit for ΔT then follows, with $L = 300\,\mathrm{mm}$:

$$\Delta z^{\mathrm{gantry}} \leq 25\,\mu\mathrm{m} \longleftrightarrow \Delta T \leq 25.0 \times 10^{-3}\,\mathrm{K}$$

Although this number represents a worst-case scenario, it confirms the need for passive and active temperature control of the measurement setup. A technical solution to equalize the temperatures between all parts of the qBOUNCE vacuum chamber is currently in development with the help of thermoelectric cooling. Still, any gradual temperature changes enter directly into the measurement accuracy, as described in section 3.4.1. It seems advisable to consider thermal expansion when designing the next iteration of the measurement setup.

3.5 Phase Shift Measurements for Software PID

In the prototype, all sensors and actuators are connected to a shared bus (either Ethernet or USB) and digitally transmit data to the PC. The feedback response is then calculated in software using LABVIEW's MATLAB plugin. This both facilitates development of the user interface controlling the PID parameters, and allows fast changes to the mathematical implementation of the PID loop. The response is returned to the piezo controller on the same bus network, which then converts the data packet to an analog voltage driving the individual piezos.

The process of data transmission occurs on a millisecond time scale. As such, the delay between data acquisition and correction of the position can not be neglected. The latency of digital signals is hard to determine in this setup and may vary to great extent.

- For one, this is because a signal bus typically can't offer real-time signalling to any participant as this would block other devices from communicating.
- Second, there is a send/receive queue at each node of the network, which introduces varying wait times based on the current traffic load.
- Third, the operating system's kernel (in our case Windows) may query the final receive buffer infrequently due to the concurrent resource use that is intrinsic to multitasking architectures.

Die approbierte gedruckte Originalversion dieser Diplomarbeit ist an der TU Wien Bibliothek verfügbar
The approved original version of this thesis is available in print at TU Wien Bibliothek.
TU Bibliothek Your knowledge hub WIEN

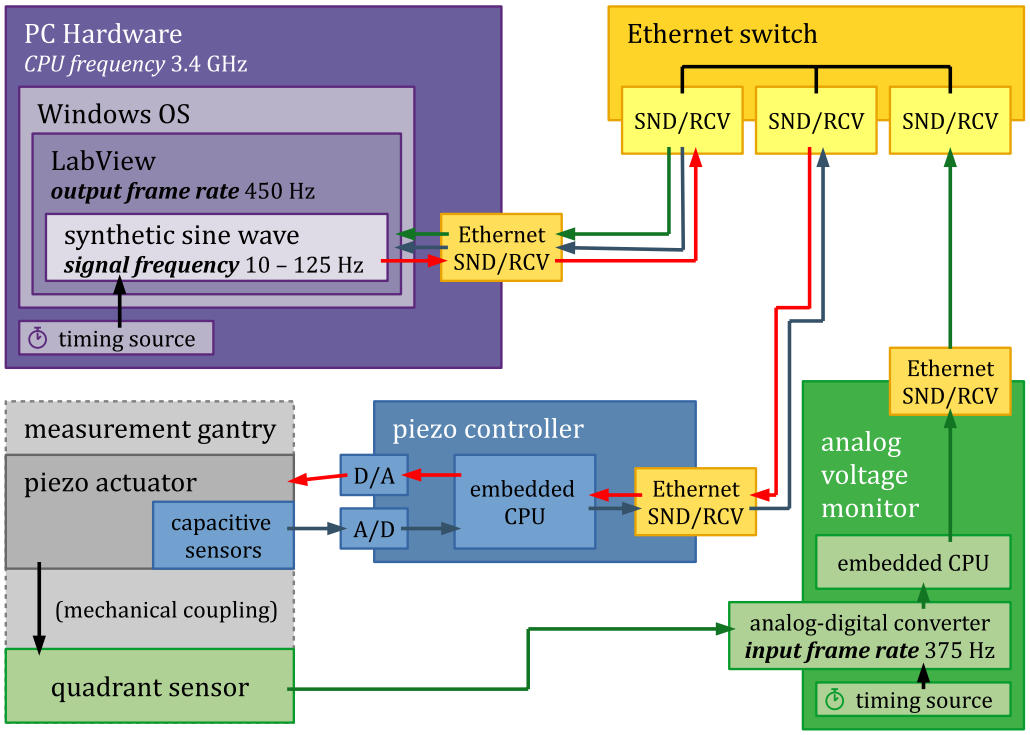

Figure 25: *Schematic of the signal path in the phaseshift measurement.* LabView *generates commands (red) which are sent to the piezo controller. The response of the measurement gantry is measured and reported back by cap.sens. (blue) and via the laser-feedback loop (green). Latency is accumulated at each point in the network.*

As a result, the stream of data packets exhibits a time delay from ADC to LabView software (called "ping"), where packets can also arrive irregularly (called "jitter" [28]).

We are looking to operate the position hold algorithm at a frequency of 1000 Hz, which is impossible to achieve with a multitasking operating system. Rather, it would be more efficient to switch to discrete analog circuits and/or real-time signal processing, as far as responsiveness of the feedback is concerned. Shorter latency will allow setting more aggressive PID coefficients, which increases position hold accuracy. For the next iteration of the position hold algorithm, it is planned to use a real-time digital signal processor (DSP), so that the entire PID algorithm can be handled on a single circuit board. This should markedly increase performance of the feedback loop.

In the following experiment, we measure the latency time on the Ethernet bus. Figure 25 shows the detailed signal path across multiple devices.

1. In the LabView environment, a rectangular approximated sine wave is generated with an **output frame rate** of 450 Hz. A protocol request is generated for each output frame and sent to the piezo controller.

2. The response of the piezo actuator is then sampled using the quad.sens. and laser reference simultaneously with an **input frame rate** determined by the capability of the ADC. The quad.sens. itself need not be calibrated, since the amplitude of the oscillation is of lesser consequence to this observation.

Die approbierte gedruckte Originalversion dieser Diplomarbeit ist an der TU Wien Bibliothek verfügbar
The approved original version of this thesis is available in print at TU Wien Bibliothek.
TU Bibliothek Your knowledge hub WIEN

3. The total latency in the signal chain creates a phase difference between the input and output signals. Due to the inertial mass of the piezo and measurement gantry, the phase shift changes for different frequencies of the sine wave (**signal frequency**).

4. The phase shift can be calculated by comparing the input sine wave with the response using a software lock-in amplifier coded in MATLAB. Any difference in phase between the input and response signal corresponds to a latency time in milliseconds.

A digital lock-in amplifier can be used to isolate the phase and amplitude information of a specific frequency, even if the captured signal sample contains noise. The signal sample is "compared" to two reference waveforms S^0 and S^{90}, where the latter is phase shifted by 90°. For the sake of simplicity, *sin* and *cos* functions are typically used, although some applications use square waves. By multiplication of the signal sample with the reference waveforms ("dual-phase demodulation"), the phase shift φ and radius r can then be calculated. For more extensive information about lock-in amplifiers, please refer to [14].

In our implementation, the frames of the input and output signals are fed into a first-in-first-out (FIFO) buffer. The calculations are carried out according to the following formulas:

$$S_i^0 = A\sin(\omega t_i), \tag{17a}$$
$$S_i^{90} = B\cos(\omega t_i), \tag{17b}$$
$$x_i = S_i^{\text{resp}} \cdot S_i^0, \tag{17c}$$
$$y_i = S_i^{\text{resp}} \cdot S_i^{90}, \tag{17d}$$
$$r = \sqrt{\left(\frac{1}{n}\sum x_i\right)^2 + \left(\frac{1}{n}\sum y_i\right)^2}, \tag{17e}$$
$$\varphi = \arctan\left(\frac{\sum y_i}{\sum x_i}\right)\frac{\pi}{180}, \tag{17f}$$

where the timestamp of each distinct frame is represented by t_i, the output frames by S_i^0, and the input (response) frames by S_i^{resp}. The array S_i^{90} contains the output frames which are phase shifted by 90°. In practice, this is accomplished by simultaneously generating a cosine signal. The averaging period can be chosen by setting the buffer length to an appropriate frame count.

The experiment is repeated for a range of signal frequencies. At higher frequency, the weight of the gantry increasingly deteriorates the system response, which can be observed via the phase shift of the return signal. As an additional parameter, the influence of different output frame rates is investigated. This is to show whether a higher instruction rate overwhelms the piezo controller or leads to saturation on the network bus.

Figure 26 shows the change in phase shift for different output frame rates. The higher the frame rate, the closer the discretized sine wave output approximates the pure sine function. Step size between two single instructions is also decreased, which leads to an overall improvement in the piezo's response. The maximum error of the piezo position compared to the synthetic source signal is equal to the signal change

Die approbierte gedruckte Originalversion dieser Diplomarbeit ist an der TU Wien Bibliothek verfügbar
The approved original version of this thesis is available in print at TU Wien Bibliothek.
TU Bibliothek Your knowledge hub WIEN

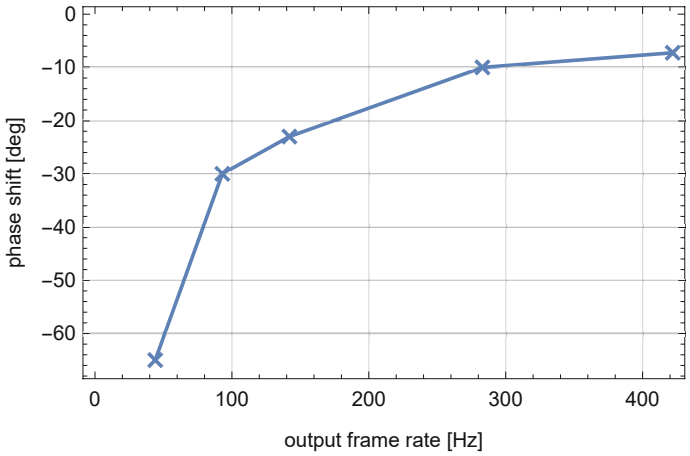

Figure 26: *Effect of the output frame rate on phase shift, tested with a* 10 Hz *sine wave with* 1 µm *amplitude. For higher frame rates, the rectangular sine better approximates the pure sine wave, which improves the response of the piezo actuator and reduces phase shift.*

during one frame of the output signal. For a 10 Hz sinewave at an output frame rate of 60 Hz, this results in a phase shift of $10/60 = 0.0167$ s or 60°. From this perspective, it is desirable to set the output frame rate as high as possible. We are however limited by the computational power of the LabView PC. In this case, the software is proven to run stably at a frequency of 450 Hz without making use of any real-time libraries.

With regards to network saturation, an output frequency rate of 450 Hz would roughly require a 2 ms round-trip latency, provided that the piezo controller operates on a TCP socket. At these rates, the data throughput is far from saturating the 100 Mbps Ethernet connection. As an additional precaution, all devices related to the measurement are connected in a private subnet via an Ethernet switch.

During the test, the signal frequency of the input sine wave is varied from 10 Hz to 125 Hz, in order to stay clear of the Nyquist-Shannon limit of the input frame rate. The amplitude on the piezo actuator is set to 0.25 µm so as to stay below the power limit for the controller and crystal at all frequencies. The ADC is used to acquire the output wave at an input frame rate of 375 Hz. Results are averaged for a duration of 60 s at each signal frequency. The resulting data points are plotted in figure 27, both for the quad.sens. and the cap.sens. built into the piezo actuator itself.

There are several interesting observations to be made from these experimental data:

- The phase shift plot shows a staircase pattern in both quad.sens. and cap.sens.. This is probably due to aliasing between the input or output sampling rate and the frequency of the test signal. Another cause may be that Windows kernel scheduling queries the Ethernet receive queue, which is used to deliver results for both sensors, at inconsistent intervals.

- Negative phase shifts indicate that the phase shift must be greater than one cycle.

- Both quad.sens. and cap.sens. show a spike in amplitudes due to the internal

Die approbierte gedruckte Originalversion dieser Diplomarbeit ist an der TU Wien Bibliothek verfügbar
The approved original version of this thesis is available in print at TU Wien Bibliothek.
TU Bibliothek Your knowledge hub WIEN

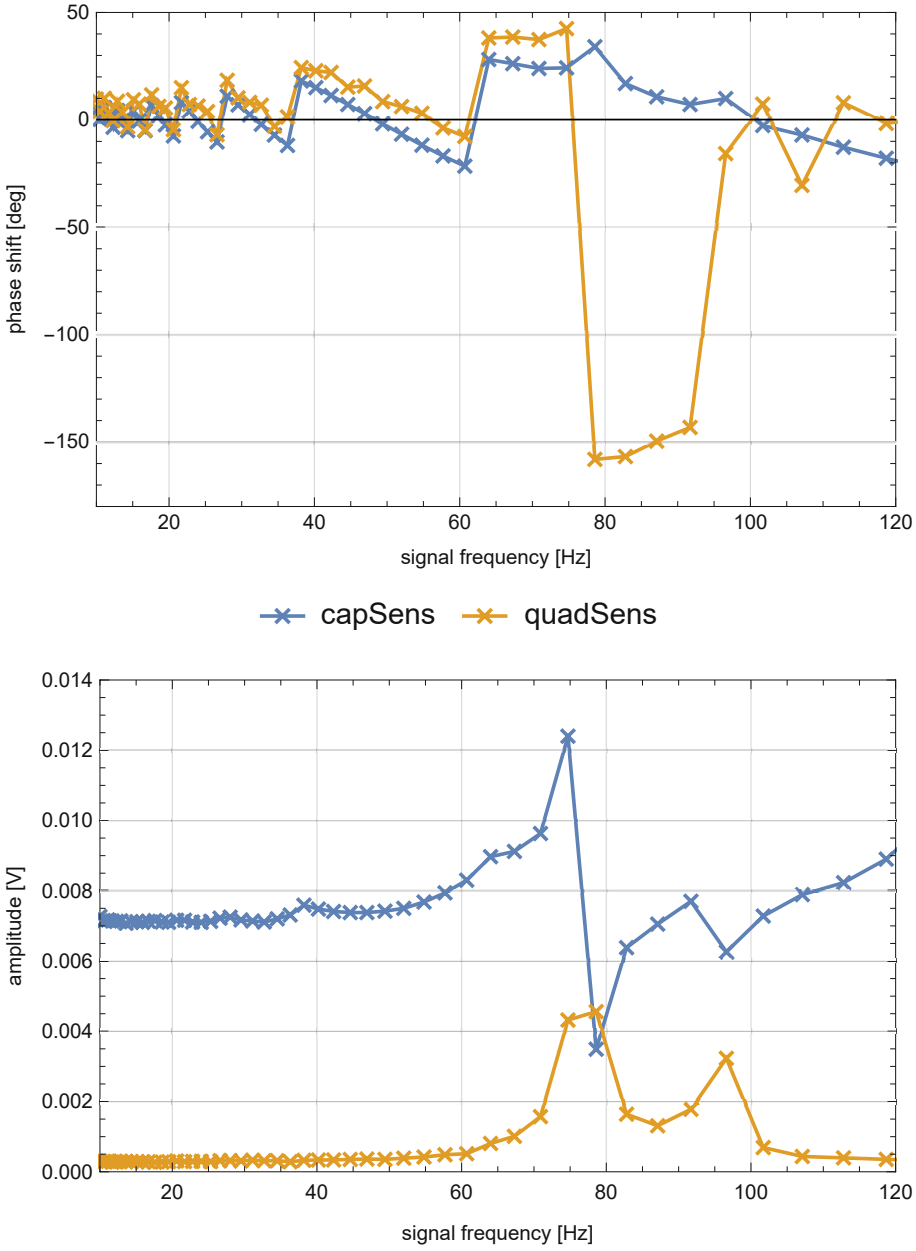

Figure 27: *Phase shift and amplitude of the feedback loop shown in fig. 25, calculated according to eq. 17. The measurements are made with a piezo amplitude of* 0.25 µm*, output frame rate* 450 Hz*, input frame rate* 375 Hz*, and the results are averaged over a period of* 60 s*.*

Die approbierte gedruckte Originalversion dieser Diplomarbeit ist an der TU Wien Bibliothek verfügbar
The approved original version of this thesis is available in print at TU Wien Bibliothek.

resonance of the measurement gantry at around 80 and 95 Hz. In order to avoid stressing the piezo actuator at the resonance peak, a several notch filters are used in the controller to dampen the response at selected frequencies.

In this case, the linear Z-axis notch filter is set to 85.4 Hz, while the notch filters on the X and Y rotational axes are set to around 47 Hz. In response, the phase shift of the quad.sens. changes from 45 to $-155°$ (equivalent to 205°). This behavior is expected for a notch filter and corresponds to a 90° phase shift for the low-pass and high-pass component, respectively. On the other hand, the internal cap.sens. shows no phase change at these frequencies. This might hint at the formation of a standing wave on the measurement gantry, where both ends move in opposite directions, akin to two coupled harmonic oscillators. Due to the differing readout mechanisms, the total latency to each sensor varies, and as a result the phase information can not support such a theory.

- Overall, it seems that the phase shift of the response signal is negligible compared to the aforementioned measurement phenomena. The signal latency must nevertheless be taken into account when designing the position hold mechanism.

In conclusion, some valuable insight is gained by analyzing the latency of the signal chain. One important limitation to the feedback mechanism is the use of a LabView environment together with a software implementation of the PID controller, which limits the processing speed. The responsiveness of the piezo can be boosted by switching to a real-time DSP, thus providing a smoother output waveform. An additional increase in latency comes into effect at higher frequencies due to the necessary avoidance of resonance peaks. This poses limitations both on the hardware design to minimize resonances, as well as on software control in avoiding specific output frequencies. Combining these findings with other results from the performance testing should markedly increase the precision of the measurement system.

4 Proof of Principle Measurements

Using the measurement setup described in section 2, several measurements are made as a proof-of-concept for acquiring mirror surface maps and determining step heights.

As we will see in the following sections, the translator stage introduces not only tilt, but also roll angles to the movement of the measurement gantry. This significantly hampers the use of the laser feedback mechanism for height stabilisation, as the prototype measurement cube is only built to handle angles parallel to the movement axis and deviations in the Z-position. However, it is possible to gather quantitative information about the offset and tilt of the translator stage with the method described in section 4.2. If need be, these results can be used to apply corrections to already recorded data.

Lastly, a step measurement across the edge of two adjacent mirrors is presented. The DeltaSens fiber interferometer allows to record absolute distance of the optical sensors to the surface. This enables measurement of the vertical mirror offset at nanometer-scale accuracy.

Die approbierte gedruckte Originalversion dieser Diplomarbeit ist an der TU Wien Bibliothek verfügbar
The approved original version of this thesis is available in print at TU Wien Bibliothek.
TU Bibliothek Your knowledge hub WIEN

4.1 Mirror Surface Maps

In order to acquire a surface map, the mirror specimen or surface-under-test (SUT) is placed on top of the granite surface on precision spacers. Movement of the measurement gantry along the X-axis is provided by the stepper motor of the translator stage. By moving the mirror sideways under the gantry, multiple surface elevation lines (X-axis) are then measured across its width (Y-axis).

The construction of the measurement cube has limited the amount of surface detail we were able to acquire. Along the length of the mirror (X-axis), a measurement was taken approximately every 20 mm. The measurement duration was set to 10 s for each data point, in which time the DeltaSens interferometer will record 170.000 samples (17 kHz sample rate). In a similar setting, the SUT was measured again with the SIOS interferometer, which calculates a mean of 200.000 samples (20 kHz sample rate) for each point. All of the measurements were made while the laser feedback mechanism was deactivated. This prevents the feedback from negatively affecting the gantry offset due to amplification of the roll angle of the translator stage (confer section 4.2).

When we were using the SIOS gantry, we were limited to three mirror positions / lines. This was due to the large offset of the SIOS beam splitter on the Y-axis. In conjunction with the placement of the measurement cube's ITEM profile bars, positioning of the mirror was limited. Three lines with a spacing of 12 mm were chosen to reflect the distance between the sensors II and III (shown in figure 9). Thus, sensor III of a given line would ideally coincide with sensor II from the previous line. Due to the varying tilt and roll in the translator stage, this did not hold true.

The (much more compact) DeltaSens gantry was used to record another five lines with a spacing of 10 mm. This allows comparison of the two measurement devices with respect to results and overall performance.

The resulting data is evaluated in multiple steps, shown in figures 28 and 29. The evaluation process is detailed below for each subplot (a) to (d). Wherever applicable, Gaussian error propagation was used to calculate the measurement uncertainty.

(a) For DeltaSens, some obvious fringesteps are removed by shifting the remainder of the data by a multiple of $\lambda/2$. The inverted distance scale of the SIOS interferometer is compensated accordingly. In both cases, the arbitrary measurement offset is removed for all lines with respect to the point $X = 100\,\text{mm}$. All other plots are derived from this data source.

(b) One option would be to take the first measurement line as a reference for the translator stage error, and to then subtract that line from all subsequent data. This is suboptimal, as the first measurement is the outermost line and the SUT often shows spherical deviations in both X- and Y-axes. Also, any measurement errors in the "reference" line are transferred to all other lines.

(c) Instead of using the first measurement line as reference, a virtual reference is constructed by coordinate-wise averaging of all lines. This effectively suppresses the propagation of stochastic errors from the first line to all others. As a result, we are able to observe small oscillations with a length of 20 mm which are mentioned in previous studies of the movement system [11, p. 19]. This periodic

Die approbierte gedruckte Originalversion dieser Diplomarbeit ist an der TU Wien Bibliothek verfügbar
The approved original version of this thesis is available in print at TU Wien Bibliothek.
TU Bibliothek Your knowledge hub WIEN

Die approbierte gedruckte Originalversion dieser Diplomarbeit ist an der TU Wien Bibliothek verfügbar
The approved original version of this thesis is available in print at TU Wien Bibliothek.

Figure 28: *Measurements for a mirror surface made using the DeltaSens interferometer. The linear stage is referred to as "micos".*

Figure 29: *Measurements for a mirror surface made using the* SIOS *interferometer. The linear stage is referred to as "micos".*

Die approbierte gedruckte Originalversion dieser Diplomarbeit ist an der TU Wien Bibliothek verfügbar
The approved original version of this thesis is available in print at TU Wien Bibliothek.

tilt/roll motion of the gantry is very likely caused by the mounting of the translator stage. Several mounting screws are placed 20 mm apart to connect the stage to the measurement cube. This is where imperfect mounting conditions then result in deformation of the axis, showing as a "wiggling" motion.

(d) Finally, results from *(c)* are plotted in a three-dimensional view. The XY-coordinates are normalized with respect to an absolute coordinate system, so the two measurements of SIOS and DeltaSens can be directly compared.

For comparison, a surface scan obtained through an external contractor (see figure 30) shows a convex surface with a maximum deflection of approximately 750 nm. It has come into question whether this pertains to the same surface, as both sides of the mirror have a reflective coating and remarks in the documentation remain unclear.

Overall, both SIOS and DeltaSens surface maps agree that the deviation from the horizontal plane is on the order of 20 µm. However, not all of this can be attributed to curvature of the SUT. Any gravitation-related sagging of the mirror was reduced by using precision spacers as supports along its length, which showed negligible effect. This leaves one culprit remaining: the tilt and offset of the translator stage which carries the measurement gantry.

4.2 Measuring Tilt and Offset of the Translator Stage

Because of the one-dimensional nature of the feedback loop in the prototype, it is impossible to detect tilt in the linear rail of the translator stage, and no appropriate correction can be calculated. Instead, the tilt of the measurement sled is erroneously interpreted as an additional offset by the quadrant sensor (quad.sens.), which leads to over-compensation in the feedback algorithm. The lever arm created by the distance between the reflector and quadrant detector further amplifies this error (compare figure 3).

In order to avoid this over-compensation, the feedback was deactivated during the measurements presented in section 4.1. With the positional feedback turned off, the difference between two sensor measurements z_1, z_2 at the same X-position can be used to calculate tilt $\alpha(x)$ and offset $\Delta z(x)$ of the translator stage. The results of this calculation can, in theory, be used to correct for the movement of the measurement gantry in the final analysis. As a plane of reference, either the mirror surface or the laser reference can be chosen. The following section will describe the correction with reference to the mirror surface. When choosing the laser reference as starting point, the procedure is very similar – further details can be found in appendix A.

The tilt and offset of the measurement gantry can be extracted from interferometer measurements according to the geometry shown in figure 31. However, when the mirror surface is used as a plane of reference, any information about surface deflection is lost and will be attributed to tilt and offset of the linear rail. Measurements that are corrected with this data can therefore only capture the deformation of the SUT relative to the original plane of reference. This is effectively the same as declaring the first measurement a calibration curve which sets the height zero. A cleaner approach to this problem is explained in appendix A, where the laser

Die approbierte gedruckte Originalversion dieser Diplomarbeit ist an der TU Wien Bibliothek verfügbar
The approved original version of this thesis is available in print at TU Wien Bibliothek.
TU Bibliothek Your knowledge hub WIEN

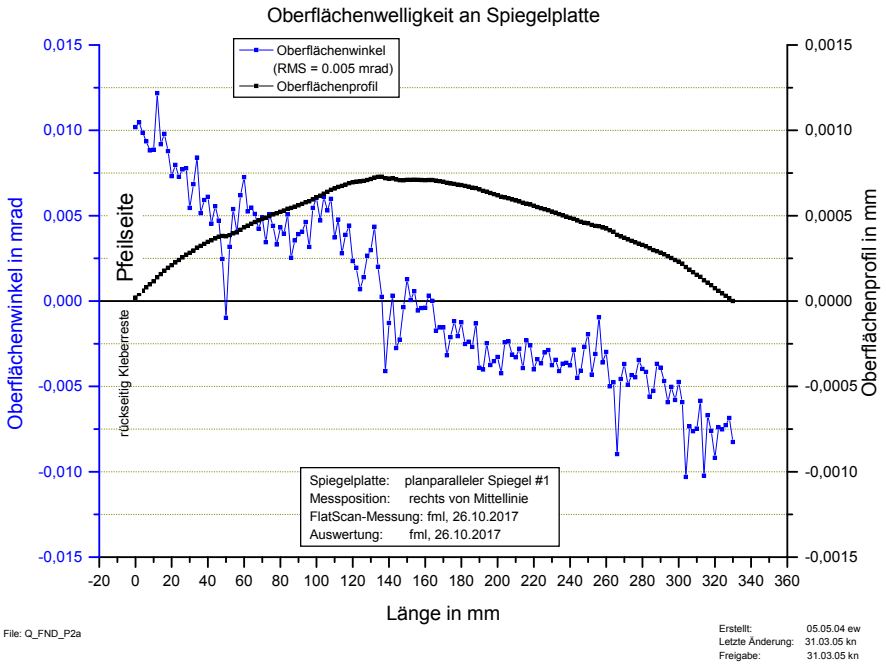

Figure 30: *Measurement of mirror surface by an external contractor. The difference between this measurement and the DeltaSens/*SIOS *results is on the order of* 20 µm. *This is interpreted as tilt and offset error introduced by the translator stage. [S-DH GmbH, 2017]*
The identification number of the mirror cannot be exactly attributed and is one of either: "#1 Lloyd", "planparalleler Spiegel #1", "#502", or "#503".

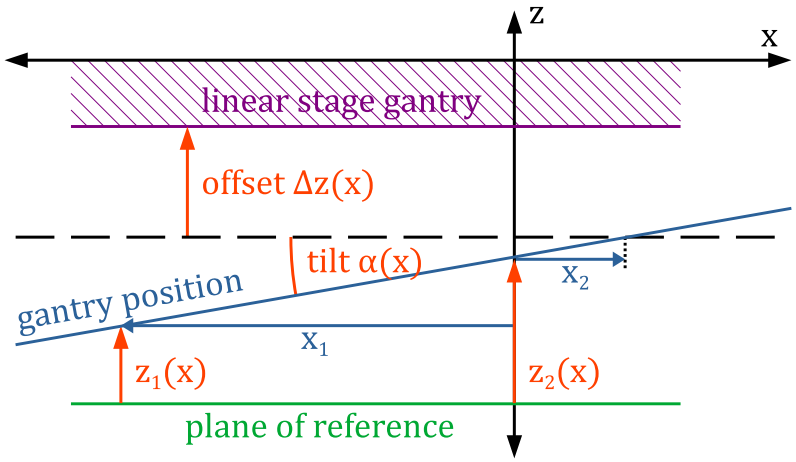

Figure 31: *Geometry for calculating tilt and offset of the linear stage. Two optical fibers (used as sensors for DeltaSens) provide the measurement points* z_1, z_2 *that allow to determine the gantry position.*

Die approbierte gedruckte Originalversion dieser Diplomarbeit ist an der TU Wien Bibliothek verfügbar
The approved original version of this thesis is available in print at TU Wien Bibliothek.
TU Bibliothek Your knowledge hub WIEN

reference is used in conjunction with the detector calibration to measure tilt and offset.

When recording the offset curve, the piezo table is first set to a fixed position (z, tilt and roll held constant by the internal feedback) in an effort to eliminate any additional variables. This specifically stabilizes tilt and offset in the piezo actuator, which may be caused by a shifting load on the gantry. Next, the combined deflection of the mirror surface and linear rail seen by the interferometer $z_i(x)$ is acquired across multiple positions of the translator stage. This step is carried out simultaneously for both sensor fibres $(1, 2)$ on the measurement gantry. The difference of the two measurements is then used to determine Z-offset $\Delta z(x)$ and tilt $\alpha(x)$ about the Y-axis for all recorded positions x. The length x_1 describes the fixed distance between the fiber mounting points, while x_2 refers to the distance between the hindmost fiber and the axis of rotation of the gantry.

The system of equations describing distance measurements z_i on the Z-axis (confer figure 31),

$$z_1(x) = \Delta z(x) + (x_1 - x_2)\tan\alpha(x), \tag{18a}$$
$$z_2(x) = \Delta z(x) - x_2 \tan\alpha(x), \tag{18b}$$

can be solved as follows, when the origin of vertical offset is specified at an arbitrary calibration point x_c along the travel axis of the linear stage.

$$\Delta z(x_c) := 0, \tag{19a}$$
$$x_2 = \frac{z_2}{z_2 - z_1} x_1 \Big|_{x=x_c}, \tag{19b}$$
$$\alpha(x) = \arctan\left(\frac{z_1 - z_2}{x_1}\right), \tag{19c}$$
$$\Delta z(x) = z_2 + \frac{x_2}{x_1}(z_1 - z_2) \tag{19d}$$

Finally, corrections can be calculated from offset and tilt data through appropriate choice of the distances x_i in relation to the original correction measurements. For the DeltaSens gantry, the distance between the two fibers is fixed at $x_1 = 10\,\text{cm}$, while equation 19b assumes that the rotational arm length x_2 is constant for the entire translator stage. This does not necessarily hold true, especially in cases where the radius of curvature changes along the rail. However, this representation was chosen to be able to independently calculate tilt and offset for each point along the translator stage. Alternatively, the choice $x_2 = 0$ can be made, in which case $\Delta z(x)$ and $\alpha(x)$ will both contain parts of the tilt and linear offset, but will directly correspond to the necessary corrections that the piezo table has to perform.

Figure 32 shows the result of the DeltaSens tilt/offset correction measurement. The two fibers, "sens1" and "sens2" have their relative offset compensated at $x = 218\,\text{mm}$. Because of the movement range of the linear stage and the coordinate shift between the two fibers, only a limited range of the mirror (130 to 218 mm) is available for calculating corrections. The resulting tilt and Z-offset curves have an arbitrary offset, which depends on the choice of coordinate zero for the two sensors, and the selection of the calibration point x_c – in this calculation, $x_c = 130\,\text{mm}$.

Die approbierte gedruckte Originalversion dieser Diplomarbeit ist an der TU Wien Bibliothek verfügbar
The approved original version of this thesis is available in print at TU Wien Bibliothek.
TU Bibliothek Your knowledge hub WIEN

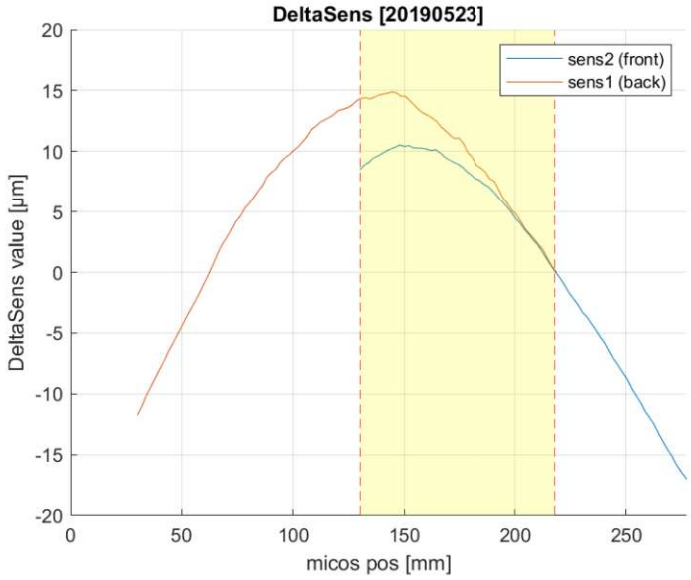

Figure 32: *Result of the DeltaSens tilt/offset correction measurement. The two fibers ("sens1", "sens2") are nulled at* $x = 218\,\text{mm}$*. The movement range of the linear stage limits the correctable range to* 130 *to* 218 mm *(yellow area).*

Within the bounds of travel range that are available for the correction, the tilt is limited to a range of 60 µrad, and the offset along the Z-axis is limited to less than 7 µm (see figures 33 and 34). This is well within the range of the piezo actuator, making it possible to pre-program the necessary corrections into the measurement routine. This is however not desirable for various reasons, for example varying offsets and rail deflections caused by temperature changes. The implementation of a 3-axis system for positional feedback will eventually supersede any necessity for tilt correction.

4.3 Applying Corrections for Tilt and Offset

Given an accurate measurement as a starting point, the previous equations 19 can in theory be rearranged to express the correction for each coordinate x along the linear rail. To obtain the corrected values $z_i^{\text{corr}}(x)$, the measured tilt $\alpha(x)$ and offset $\Delta z(x)$ must be subtracted from the raw measurement z_i:

$$z_1^{\text{corr}}(x) = z_1 - \big(\Delta z(x) + (x_1^* - x_2^*)\tan\alpha(x)\big), \tag{20a}$$
$$z_2^{\text{corr}}(x) = z_2 - \big(\Delta z(x) - x_2^*\tan\alpha(x)\big), \tag{20b}$$
$$x_i^* = x_i + \Delta x_i^* \tag{20c}$$

The tilt/offset correction, once measured, can be adapted to different sensor configurations using equation 20c, allowing to e.g. apply corrections from the DeltaSens gantry to a SIOS measurement. The distance Δx_i^* describes the coordinate shift of each sensor on the gantry relative to its corresponding position x_i during the correction measurement. The different sensor arrangements of the measurement sled are described in section 2, and a summary of all sensor positions is found in figure

Die approbierte gedruckte Originalversion dieser Diplomarbeit ist an der TU Wien Bibliothek verfügbar
The approved original version of this thesis is available in print at TU Wien Bibliothek.
TU Bibliothek Your knowledge hub WIEN

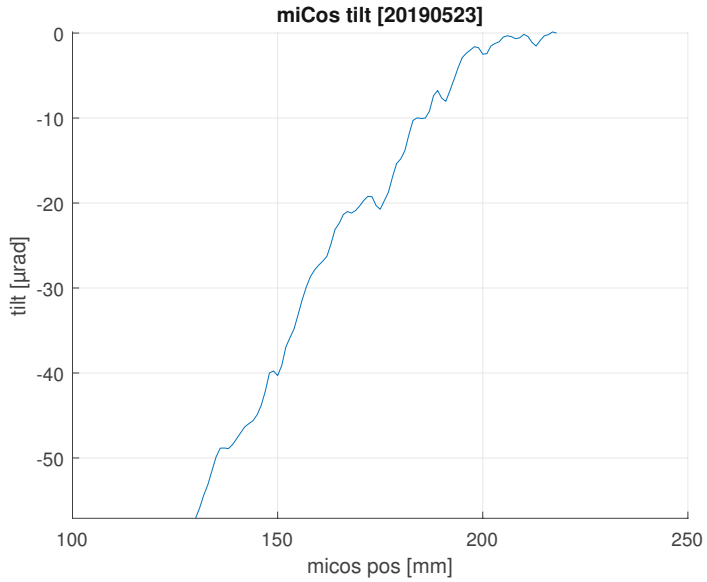

Figure 33: *Localized tilts of the linear stage ("miCos"). The tilts derived from figure 32 with equations 19 are on the order of* $60\,\mu\text{rad}$. *This excludes an arbitrary offset which is dependent on the coordinate zero of the raw data and the chosen calibration point* x_c.

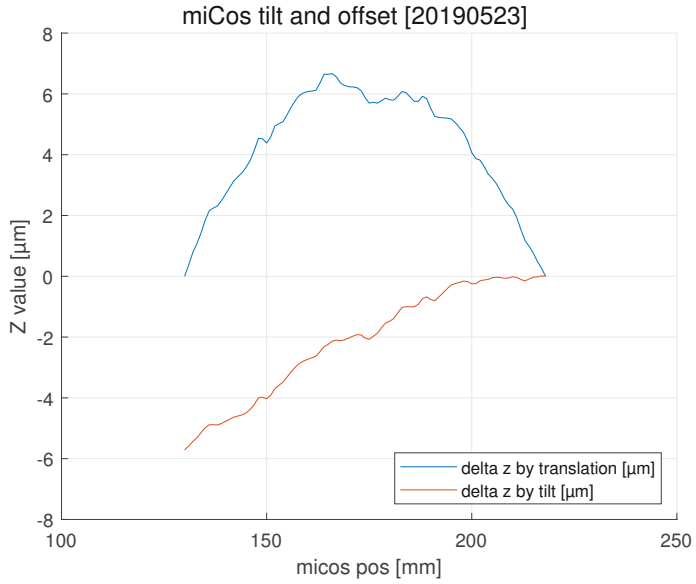

Figure 34: *Localized offset of the linear stage ("miCos"). These offsets are derived from equations 19 together with the tilt data from figure 33. For the observed coordinates, the offset introduced by the linear rail (blue) is in the range of* $7\,\mu\text{m}$. *The red line shows tilts converted into the Z-offset seen by the sensor fiber.*

Die approbierte gedruckte Originalversion dieser Diplomarbeit ist an der TU Wien Bibliothek verfügbar
The approved original version of this thesis is available in print at TU Wien Bibliothek.

$\Delta x_1^{\mathrm{SIOS_I}}$	$\Delta x_2^{\mathrm{SIOS_{II,III}}}$
$-28\,\mathrm{mm}$	$-58\,\mathrm{mm}$

Table 3: *Measurements that allow the correction data acquired with the mirror reference to be translated to other sensor configurations. For an overview of sensor positions, see figure 35.*

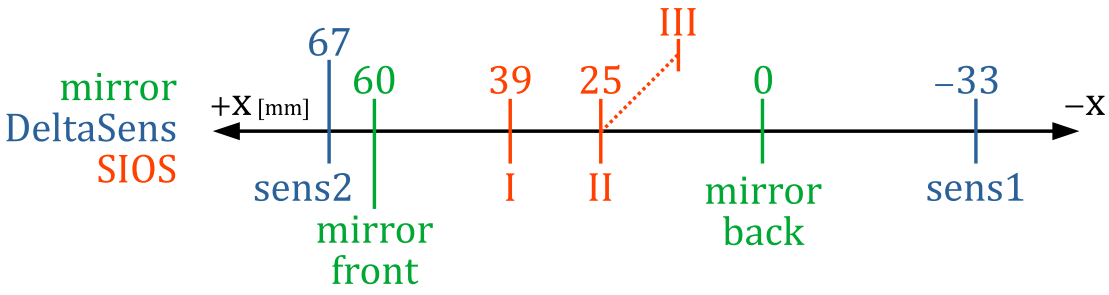

Figure 35: *Schematic showing the relative offset of various sensor configurations for DeltaSens,* SIOS*, and the concave mirror. The variables Δx_i^* can be determined by the relative offset of the sensors to each other. The positions "mirror front" and "mirror back" are explained in appendix A.*

35. In this case, the DeltaSens (DS) gantry configuration is used to measure the tilt and offset of the linear stage (thus $\Delta x_i^{\mathrm{DS}} = 0$). In case that we want to apply the tilt/offset compensation to a SIOS measurement, Δx_i^* must be set as listed in table 3.

As mentioned earlier, when the corrections derived from a "calibration" line are applied any information about the reference surface is lost and its error is incorporated into the measurement results. This process is equivalent to using the first measurement line as a reference (as done in section 4.1).

4.4 Step Measurements

One major advantage of the Optics11 DeltaSens fiber interferometer is the ability to measure absolute distances (cavity sizes) using the method described in section 2.3.1. This is useful in the initial setup of *q*Bounce, where the mirrors stages need to be precisely aligned such that the height difference vanishes to the probe particle. This requires measurement of two adjacent mirrors with an accuracy well below 1 µm.

In order to test these capabilities, two smaller mirrors are set up next to each other (see figure 36). The gap between them is set to a distance of approximately 40 µm by using precision spacers. Each mirror rests on a separate set of precision spacers, such that the vertical drop is easily adjusted to around 30 µm.

The DeltaSens fibers are then slowly moved across the gap in the two mirrors with a speed of $0.1\,\mathrm{mm\,s^{-1}}$, while samples are taken at a rate of 10 kHz. The feedback mechanism for controlling the gantry height is turned off, as any correction can be neglected over this short travel distance. Figure 37 shows the result of the measurement, both for absolute and relative measurement modes. It is evident that the relative measurement mode does not produce usable results, which is due to loss of the relative offset upon crossing the gap between both mirrors. This behavior

Die approbierte gedruckte Originalversion dieser Diplomarbeit ist an der TU Wien Bibliothek verfügbar
The approved original version of this thesis is available in print at TU Wien Bibliothek.
TU Bibliothek Your knowledge hub WIEN

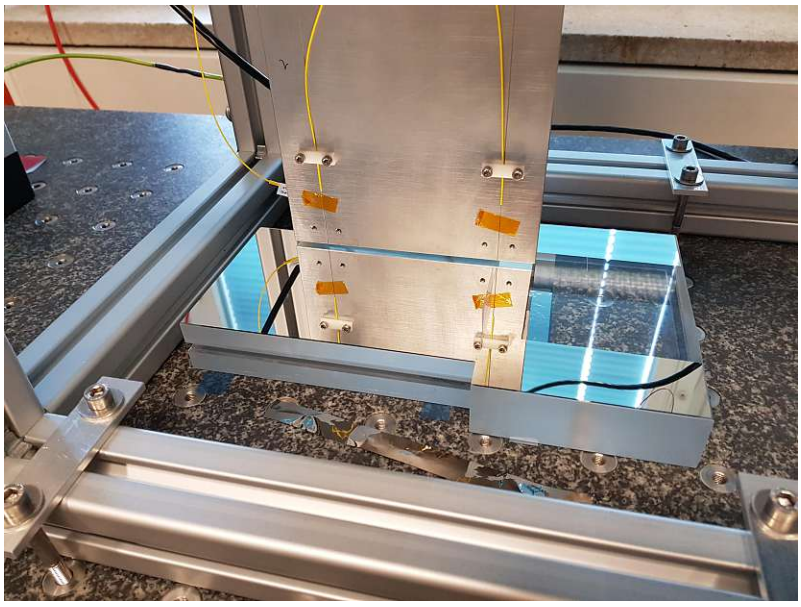

Figure 36: *Overview of the test setup for DeltaSens step measurements. Two mirrors are placed on precision spacers, such that they have a horizontal distance of ca.* 40 µm *and a vertical step of approximately* 30 µm*. The DeltaSens gantry is the moved across the gap, recording the distance information for later statistical evaluation, see figure 37.*

is similar to results produced by the SIOS SP 2000 TR. Meanwhile, the absolute measurement mode (DeltaSens DC mode) does not depend on fringe-tracking and can reliably reproduce the surface geometry, albeit at lower sample rates.

A region of $n = 5000$ samples is statistically evaluated before and after the step. The results are refined by fitting and subtracting the individual tilts of the mirrors. A sinusoidal error with a frequency of 44.5 Hz is removed from the interferometer signal by subtracting a sinusoidal fit function. The equipment manufacturer Optics11 has since commented that this may be an error present in early firmware and software versions that we used to acquire this data (`DeltaSens v0.83, BoxApp 2.0.0-beta3+outoftree IP 1.2.1`). The resulting samples are binned and subjected to a Gaussian fit, which determines the mean and uncertainty of each sample set. The statistical errors from the previous linear and sinusoidal fit are considered via their residuals at this step.

Finally, these figures are compared to a manual measurement with a (Mitutoyo LGH-1010 Laser Hologage, $n = 20$, see table 4). Using DeltaSens's absolute measurement mode proves at least two orders of magnitude more accurate than a measurement by hand.

4.5 Observation of an Oscillating Mirror

One of the goals of this work is to show that the prototype can be used to observe the oscillation of mirror regions in the qBounce experiment. This can be demonstrated by using a setup similar to that from the DeltaSens noise measurement (see section 3.2).

The oscillating surface is provided by a small piezo crystal that is driven via a frequency generator. The DeltaSens interferometer is able to track the oscillation

Die approbierte gedruckte Originalversion dieser Diplomarbeit ist an der TU Wien Bibliothek verfügbar
The approved original version of this thesis is available in print at TU Wien Bibliothek.
TU Bibliothek Your knowledge hub WIEN

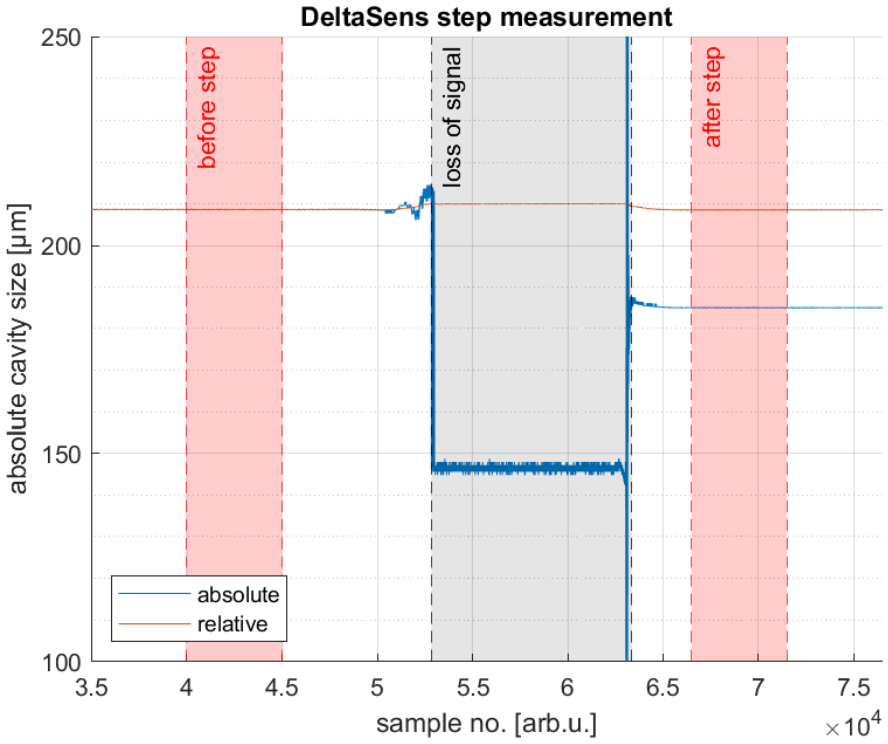

Figure 37: *Plot of a step between two mirrors, recorded with DeltaSens. The sensor is moved across the gap between two mirrors shown in figure 36 while measuring at a sample rate of* 10 kHz*. In relative measurement mode (red line), tracking is lost when crossing the gap between the mirrors. Meanwhile, absolute mode (blue line) does not depend on fringe-tracking and can reliably reproduce the surface geometry. Samples from the colored areas are later evaluated for accuracy (see figure 38 and table 4).*

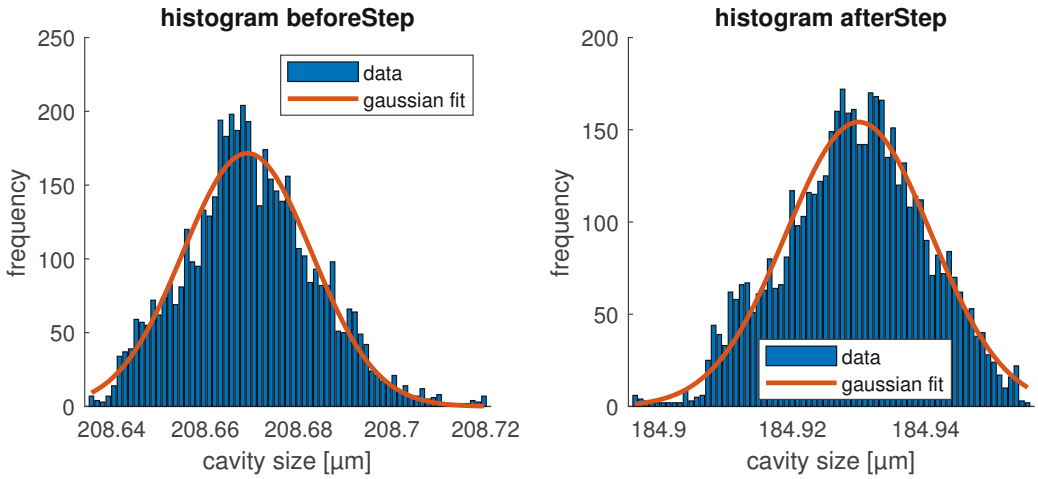

Figure 38: *Gaussian fits of sample regions before and after the step between two mirrors. After compensation of individual mirror tilts and removing a sinusoidal error signal, the samples are binned and fitted. This determines the mean and uncertainty of each sample set.*

Die approbierte gedruckte Originalversion dieser Diplomarbeit ist an der TU Wien Bibliothek verfügbar
The approved original version of this thesis is available in print at TU Wien Bibliothek.

[µm]	DeltaSens (absolute)	Linear Gage (manual)
A	208.67 ± 0.014	-7.11 ± 1.88
B	184.93 ± 0.011	-32.43 ± 1.31
$A - B$	23.74 ± 0.018	25.32 ± 2.29

Table 4: *Comparison of results for the DeltaSens absolute mode step measurement. The DeltaSens data, consisting of $n = 5000$ samples each, are compared to a manual measurement with a* MITUTOYO *LGH-1010 Laser Hologage, where $n = 20$. Automated measurement with DeltaSens proves at least two orders of magnitude more accurate than a measurement by hand.*

at 1 kHz with an amplitude of 298 nm, as shown in figure 39.

The amplitude and frequency of the oscillation are representative of the conditions during operation of the *q*BOUNCE experiment. In practice, multiple fibers can be used in conjunction with DeltaSens to monitor the oscillation of multiple points along the mirror stages. Due to the capability of simultaneous readout, calculating the phase difference can be done in software by comparing multiple sensor outputs.

5 Recommendations for the Next Iteration of the Setup

The prototype measurement system presented in this work was created to evaluate the usefulness and efficacy of using a laser reference during surface mapping. A laser-based feedback mechanism was developed in order to provide an absolute height reference, enabling the acquisicion of high-resolution surface maps. The detailed characterization discussed in the previous sections pointed at several factors which are detrimental to the system performance, such as noise and temperature variations.

Based on this experience and insights gained during the proof-of-principle measurements, the following section will propose improvements for the next iteration of the measurement system.

5.1 Initial Setup and Calibration

During the initial setup of the surface measurement system, the reference plane is established by moving the laser platform into position. As a whole, the *q*BOUNCE experiment chamber is adjusted so that it is perpendicular to the vector of local gravity. In an ideal situation, the reference beam is parallel to the optical granite holding the mirror stages, thus eliminating the need to remove tilt bias from the reference.

In practice, however, it must also be ensured that the movement range of the piezo stage and the error range of the linear stage overlap sufficiently for the height correction to occur. In an extreme case, it may be necessary to tilt the reference laser in order to be able to cover the complete range of vertical deviations of the translator stage. The coverage of the feedback mechanism can be checked by moving the measurement sled between the ends of the rail and verifying that the piezo table can follow the reference beam at all times. It may be necessary to repeatedly adjust

Die approbierte gedruckte Originalversion dieser Diplomarbeit ist an der TU Wien Bibliothek verfügbar
The approved original version of this thesis is available in print at TU Wien Bibliothek.
TU Bibliothek Your knowledge hub WIEN

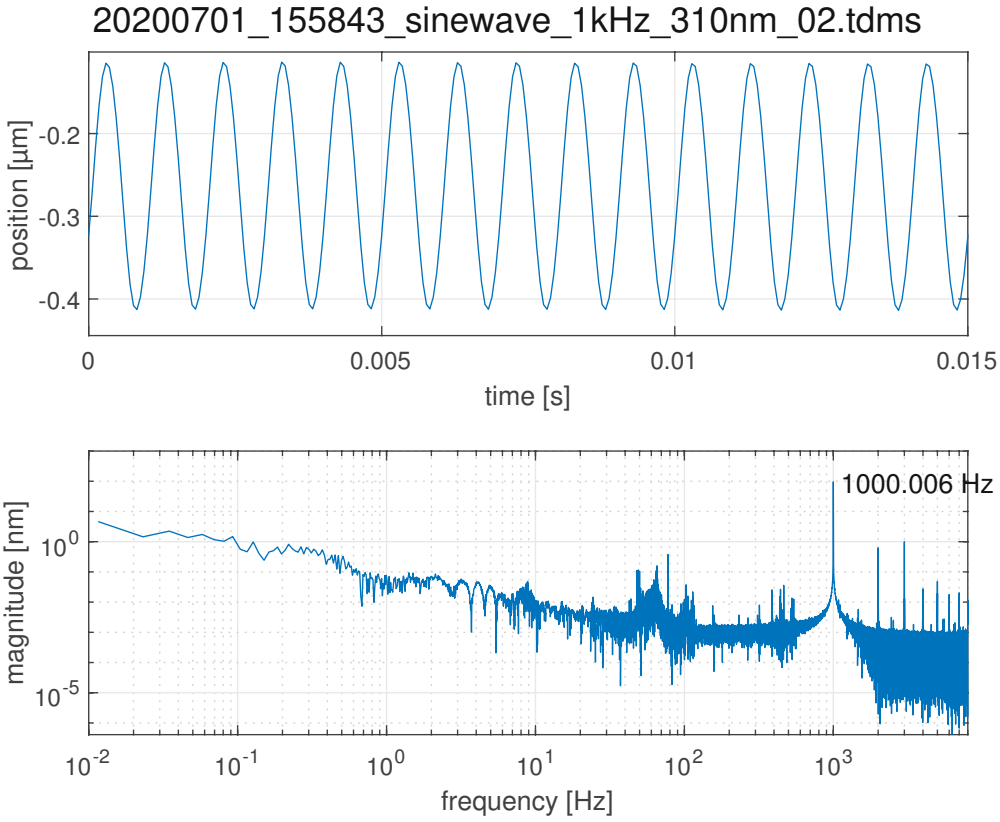

Figure 39: *This measurement shows a* 1 kHz *sine-wave tracked by the DeltaSens interferometer at a* 10 kHz *sample rate. The signal is produced by a piezo crystal oscillating with an amplitude of* 298 nm.

Die approbierte gedruckte Originalversion dieser Diplomarbeit ist an der TU Wien Bibliothek verfügbar
The approved original version of this thesis is available in print at TU Wien Bibliothek.

the reference until this condition is met.

Depending on the frequency of readjustment made to the reference mechanism, it can be prudent to automate this range check to save some time during setup. It is also advisable to perform checks at regular intervals (e.g. every week) in order to make sure that the reference laser remains properly aligned.

The adjustment of the geometric anti-spring (GAS) filter toward the desired minimum resonance frequency (see section 3.1.4) is also performed during setup. The GAS filter resonance frequency can be observed manually with a stopwatch or using a positional sensor with Fourier transform in order to obtain the precise frequency. Due to these frequencies being significantly below 1 Hz, any adjustments can be a time-consuming process. It must be kept in mind that the GAS filter is temperature and weight sensitive (see section 3.4.2). The adjustment should therefore be carried out while the temperature compensation is active and only after all constituents of the measurement sled have been put in place.

5.2 Rail Error

The large-area surface scanning system uses a linear stage to move the measurement platform across the surface-under-test (SUT). The linear stage is used in conjunction with the height feedback system and the piezo actuator to keep the surface measurement device at a uniform height. In order to achieve this, the deflection introduced by the linear stage must be less than the movement range of the piezo. In this work, early measurements of the rail deflection were made with the feedback only being able to correct the height of the measurement platform. In addition to this, the linear stage also causes the platform to tilt (rotation perpendicular to direction of travel) and roll (parallel to direction of travel). These deviations are characterized in section 4.2.

Rail error can be avoided by purchasing high-quality linear stages, but the overall construction of the measurement cube needs to be taken into consideration. Internal mounting stresses can lead to the deformation of the linear rails, thus creating additional error. The placement of additional structural supports can help minimize this error at the source.

5.3 The Reference Beam

There are several factors determining the reliability and quality of the reference laser beam, as discussed in the following sections. In addition to the frequency stability and light distribution, one has to consider the impact of geometrical optics and reference beam patterns. When the height feedback mechanism is used to stabilize the measurement sled at sub-micrometer precision, the thermal expansion and thus drift of the reference beam must be prevented through active and passive stabilization.

5.3.1 Laser Spot vs Laser Plane

The current prototype features only one-dimensional correction of height the measurement sled with respect to the reference beam. This cannot compensate for tilt and roll that the sled inevitably experiences as it travels along the linear rail. To be able to stabilize all three axes requires three separate quadrant sensor (quad.sens.)

Die approbierte gedruckte Originalversion dieser Diplomarbeit ist an der TU Wien Bibliothek verfügbar
The approved original version of this thesis is available in print at TU Wien Bibliothek.
TU Bibliothek Your knowledge hub WIEN

arrays distributed across the measurement platform, each with its own concave mirror. In the upcoming iteration, the measurement sled will also be able to travel sideways with the help of a second linear stage. With that in mind, a solution needs to be found to allow the reference beam to reach each quad.sens. across the width of the measurement range.

When using three sensors to stabilize the measurement platform, we are only interested in capturing the up-down movement at each quad.sens. in order to establish tilt, roll, and height deviation from the relative displacement of the sensors. Since the feedback sensitivity decreases with spot diameter and light intensity, beam divergence must be avoided both on the horizontal and vertical axes.

We have found two ways to solve this problem:

- An elegant solution would be to widen the laser spot to a laser line using beamforming optics. Two mirrors with specially calculated geometry [27] are used to create a constant intensity distribution along the horizontal axis and increase the vertical Gaussian beam to a usable diameter. A top-down diagram of this approach is shown in figure 40a.

  In order to avoid beam divergence along the travel axis of the linear stage, the last beam-forming lens also parallelizes the beam in horizontal and vertical direction. In theory, this allows to cover the entire travel space with a consistent, uninterrupted plane of reference. The concave mirrors simple reflect a small part of the light towards the quad.sens., where the height deviation can be measured.

  However, in order to achieve a parallel beam in the horizontal direction, the second beam-forming lens needs to cover the entire width of the measurement range, making it some 250 mm wide. On top of that, both lenses have a complex non-spherical geometry due to the conversion from Gaussian to equal intensity distribution.

- Another method of supplying the reference is to split the laser into three parallel beams, one for each quad.sens. array, as shown in figure 40b. However, since the each laser only covers one position of the sideways travel range, the reference platform needs to be shifted sideways in synchronization with the measurement platform. This makes it necessary to have another height reference and feedback mechanism to stabilize the reference platform (not shown in figure). Three additional quad.sens. arrays are used in order to compensate tilt, roll, and height offset of the reference platform.

  This approach increases the complexity of the feedback loop, because the height reference for the measurement sled is itself dependent on a height feedback mechanism. On the other hand, the requirements for the optical quality of the beam-forming optics are much lower in such a setup.

Since the quad.sens. array can only measure tilt and roll relative to the reference beams, initial calibration of the reference platform with respect to the desired reference plane becomes necessary. In addition, the reference beam may need to be aligned such that the vertical movement of the measurement sled can be covered across the entire length of travel.

Die approbierte gedruckte Originalversion dieser Diplomarbeit ist an der TU Wien Bibliothek verfügbar
The approved original version of this thesis is available in print at TU Wien Bibliothek.
TU Bibliothek Your knowledge hub WIEN

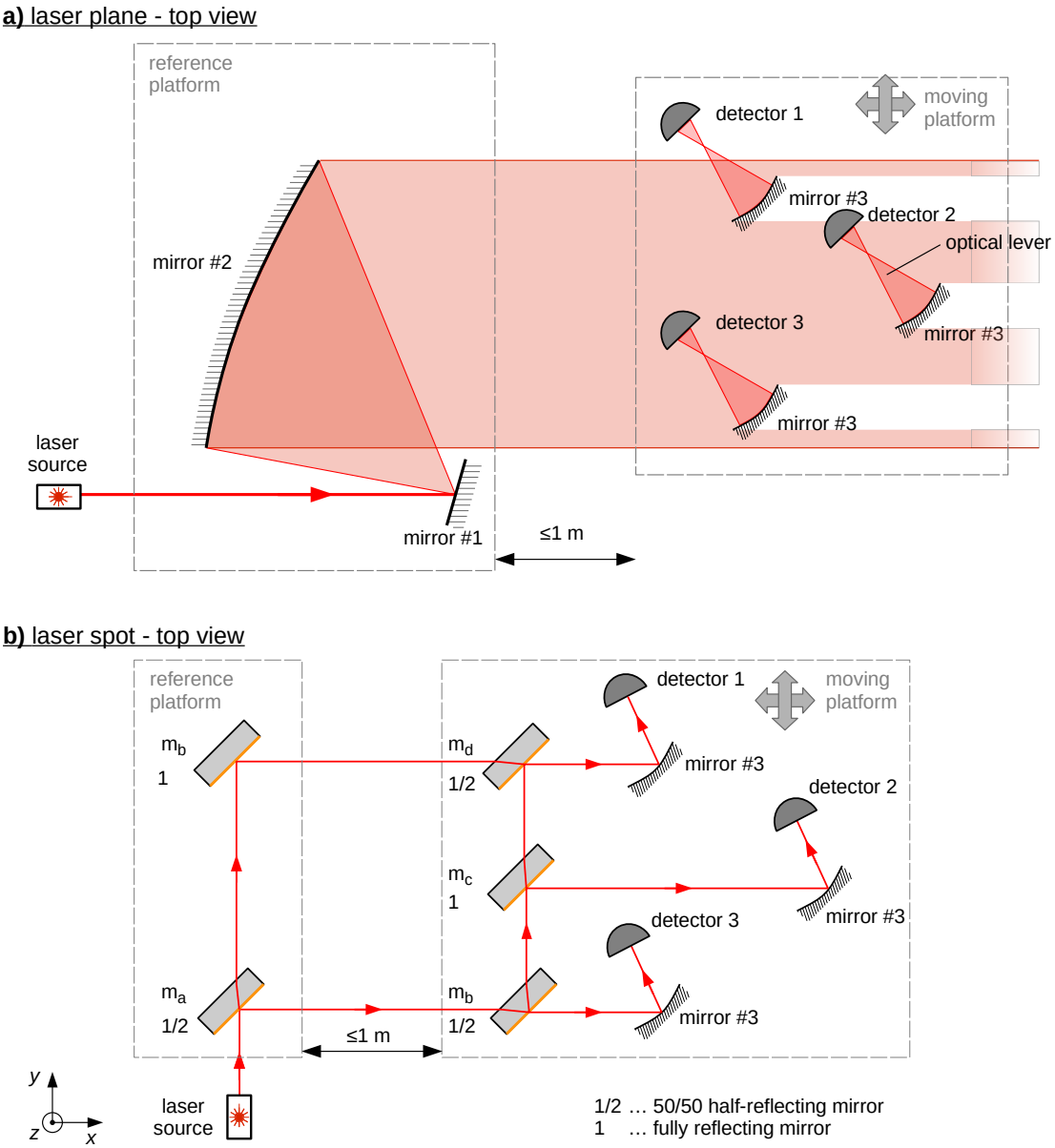

Figure 40: *Two different approaches of distributing the laser reference across three quad.sens. receivers.* (a) *Generating a plane of laser light has the advantage of covering the sideways movement of the measurement platform.* (b) *Splitting the beam into three parts using mirrors is less complex from a manufacturing standpoint, but requires the reference platform to shift sideways in synchronisation with the measurement platform.*

Die approbierte gedruckte Originalversion dieser Diplomarbeit ist an der TU Wien Bibliothek verfügbar
The approved original version of this thesis is available in print at TU Wien Bibliothek.

5.3.2 Thermal Expansion

Temperature changes have a large impact on the surface measurement system. As discussed in section 3.4.1, fluctuations that occur during normal operation in an air-conditioned lab can cause thermal expansion of the setup at a rate of $5.38 \times 10^{-6}\,\mathrm{m\,K^{-1}}$ in the prototype. The use of GAS filters, which are necessary to diminish seismic noise, further amplifies this dependency with a thermal response of $0.993 \times 10^{-3}\,\mathrm{m\,K^{-1}}$ (as seen in section 3.4.2).

For longer-term measurements, any temperature change results in a slow drifting movement in the height reference which directly enters into the measurement results. It is therefore necessary to passively and actively isolate the measurement device from temperature fluctuations. Passive isolation, in the form of EPS blocks, can be used to shield the entire qBOUNCE chamber. Active measures, like resistive heaters and peltier elements, are used to stabilize the temperature of single components by providing extra heating or cooling power. An assessment of temperature requirements shows a stability target of $\Delta T \leq 0.1 \times 10^{-3}\,\mathrm{K\,h^{-1}}$, depending on the measurement speed (see section 3.4.3). The measurement duration (averaging time on each measurement position) is chosen with a trade-off between accuracy and speed, where longer averaging periods usually increase accuracy. Considering the effects of thermal expansion, it cannot be extended indefinitely unless the drift of the reference source is eliminated.

5.3.3 Geometric Amplification

The sensitivity of the position-hold mechanism (feedback) is dependent on tilt and curvature of the concave reflector. In section 3.3.2, the dependency of sensitivity on multiple variables is discussed. For example, the optical lever L increases sensitivity the longer it is, however the real world places limitations on the physical dimensions of the sensor array. Likewise, minimizing the radius of the concave reflector mirror increases sensitivity, but is limited by manufacturing error and cost. Alternatively, the quad.sens. area could be increased to improve sensitivity, but that would in turn increase dark current.

With these considerations in mind, the physical design of the sensor array should be optimised for cost and performance. If the option of using two separate feedback loops for generating the feedback is chosen (see before), the cost factor would obviously increase further.

5.4 Noise Sources

One very important factor with respect to measurement accuracy is noise. Figure 41 shows all external and internal sources of noise in the signal chain of the surface measurement device. The goal of using height stabilization for the measurement platform is to compensate the errors introduced by the rail of the translator stage. This allows measurement of the SUT without unwanted or erroneous offsets. Several noise sources contribute to the position hold accuracy (Z-position accuracy) and ultimately enter into the measurement results, as described in the following sections.

Die approbierte gedruckte Originalversion dieser Diplomarbeit ist an der TU Wien Bibliothek verfügbar
The approved original version of this thesis is available in print at TU Wien Bibliothek.
TU Bibliothek Your knowledge hub WIEN

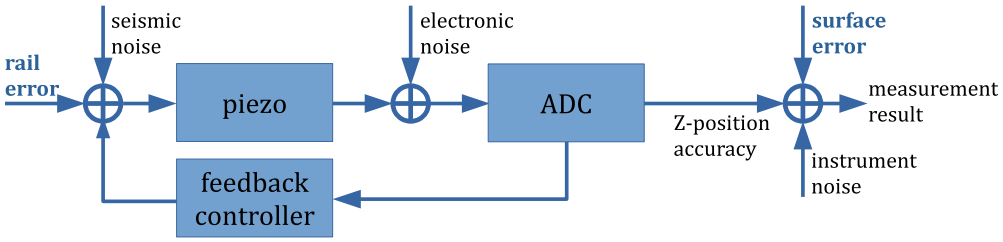

Figure 41: *Signal chain of the surface measurement device. The goal is to measure surface topology while avoiding systematic error introduced by the linear stage rail. Several noise sources contribute to the position hold accuracy (Z-position accuracy) and enter into the measurement results.*

5.4.1 Seismic Noise

The spectrum of seismic noise was measured on-site in Vienna with a geophone. For an estimation of noise at the Grenoble operational site, the New High-Noise Model (NHNM) and noise measurements from the prototype surface measurement device were compared. Overall, the noise models show that the amplitude of the unattenuated seismic noise exceeds the accuracy target of 10 nm by 20 to 30 dB depending on the scenario (see section 3.1.3).

Seismic noise is typically attenuated with the use of foam and rubber damping pads, and spring systems with low resonance frequency. The high-vacuum environment of *q*BOUNCE precludes the use of foam, leaving only rubber pads (more specifically elastomers with low out-gassing, such as DuPont Viton). On the other hand, spring dampers increase in size the lower their resonance frequency, and are limited by the internal size of the vacuum chamber. Considering this, the GAS filter (see section 2.7) is exceptionally well suited for this use-case because it offers high-performance attenuation while retaining a compact size, however at the cost of high temperature dependency (section 3.4.2). Using a simple transfer function model and making realistic assumptions about the properties of the GAS filter, it is shown that the attenuation is sufficient to reach the accuracy goal.

In order to avoid resonance peaks which could amplify seismic disturbances, the design of the measurement device must be checked for its possible geometry that could cause such acoustic resonances. Avoiding resonance peaks is important for the operation of the high-frequency feedback as a power excursion could cause damage to the equipment.

5.4.2 Electronic Noise

Electronic noise is generated by the components of the electrical circuit and by static noise that is picked up in analog signal paths. Investigation into the electronic noise at a junction point before the analog-to-digital converter (ADC) shows that the noise amplitude is equivalent to 167 nm RMS (see section 3.1.2).

The influence of electronic noise on the measurement scales with the conversion factor of the quad.sens. outputs (sensitivity, as discussed in section 3.3.1). As such it is desirable to keep analog noise as low as possible in order to facilitate high sensitivity of the sensor. This can be achieved through shielded cables, by keeping analog signal paths short, and by using specially designed low-noise power supply units (LNPSUs). The signal-to-noise ratio (SNR) should have a critical role in the

Die approbierte gedruckte Originalversion dieser Diplomarbeit ist an der TU Wien Bibliothek verfügbar
The approved original version of this thesis is available in print at TU Wien Bibliothek.
TU Bibliothek Your knowledge hub WIEN

choice of ADC, which again starts with the use of low-noise power supplies.

5.4.3 Instrument Noise

Another contributing factor to the overall result is the noise of the interferometric measurement device itself. As shown in section 3.2, the noise floor of the Optics11 DeltaSens device is well below the target of 10 nm in the relevant frequency range.

The noise measurement shows that the spectral noise is below $1\,\mathrm{nm\,Hz^{-1/2}}$ at 100 mHz, and gets lower with increasing frequency. Overall, this represents a value of −46 dB compared to the target accuracy. It would therefore seem sensible to first focus on other aspects of the prototype, where improvements can be made with lower effort.

5.5 Goals

At this point, it is possible to evaluate the goals set in section 1.2 and summarize the performance of the prototype. The following list covers all goals as set before, with a summary of the relevant findings from this work:

1. *Measure the height across the mirror surfaces while the experiment does not operate, covering an area of* 600×250 $\mathrm{mm^2}$*, within an absolute coordinate system.*

   The laser reference system has been shown to operate reliably and can cover the aforementioned area. In order to compensate all error modes that originate from the linear movement system, a three-dimensional positioning system needs to be used. This will be implemented in the upcoming iteration of the position hold system.

   Furthermore, the work area of the laser reference can be arbitrarily extended to cover large distances. The accuracy achievable with the laser reference source is only limited by the defocusing of the light beam and thus by the quality of optical components used within.

2. *Measure the vertical steps between the mirrors to provide for their alignment, better than with manual methods.*

   A proof-of-principle measurement was performed using the prototype setup. Even with many improvements to the mechanism still outstanding, the vertical step between two adjacent mirror surfaces can be measured to an accuracy of 18 nm (see section 4.4). This represents an improvement of at least two orders of magnitude in comparison to manual measurement methods.

3. *Provide a readout to check phase and amplitude of the oscillating stages while the experiment operates.*

   Another proof-of-principle measurement (section 4.5) shows that the DeltaSens interferometric measurement device is capable of tracking a SUT which is undergoing a sinusoidal up-down-movement with a frequency of 1 kHz and an amplitude of 298 nm. This movement is equivalent to the stage oscillations during operation of the *q*Bounce experiment.

Die approbierte gedruckte Originalversion dieser Diplomarbeit ist an der TU Wien Bibliothek verfügbar
The approved original version of this thesis is available in print at TU Wien Bibliothek.
TU Bibliothek Your knowledge hub WIEN

Due to the phase-synchronous readout provided by the split-sensor approach of DeltaSens, phase comparisons between multiple sensors can easily be performed in software.

4. *Reach an accuracy of* $\sigma \leq 10\,\text{nm}$ *when the mirror is static, within reasonable time of measurement (the shorter the better).*

   The prototype hardware setup presented in this work is capable of reaching a position-hold accuracy of 192 nm RMS. In order to pursue the accuracy target, extensive investigation of noise interference (among other factors) was undertaken. Combining these insights with practical experience gained from building the prototype and comprehensive re-designs of the structural components, we are optimistic to achieve the accuracy goal in the upcoming iteration of the measurement setup.

In summary, all of the set goals were achieved, with the exception of the accuracy target (goal 4). The close evaluation of the prototype performance helps with addressing this shortcoming in the next iteration of the prototype.

Die approbierte gedruckte Originalversion dieser Diplomarbeit ist an der TU Wien Bibliothek verfügbar
The approved original version of this thesis is available in print at TU Wien Bibliothek.
TU Bibliothek Your knowledge hub WIEN

6 Conclusion

In this work, a prototype of the large scale surface metrology device was constructed and evaluated. The device is designed for use as part of the *q*BOUNCE experiment, where several mirror surfaces need to be precisely aligned and mapped, enabling increased precision in the main experiment.

The prototype uses an innovative laser-guided approach to provide a height reference during the measurement, which eliminates the errors originating from physical references used in previous designs. The choice of a new interferometric measurement system (DeltaSens) also allows to capture absolute distances, which enables measuring height differences ("steps") between mirror stages.

A linear stage moves the measurement platform across the surface-under-test (SUT) while a piezo actuator compensates any occurring height deviations. The proof-of-concept measurements show that the prototype is capable of scanning the SUT and acquiring topology data. The measurement platform, which is height-stabilized by the laser feedback mechanism, reaches a position-hold accuracy of 192 nm RMS in the prototype. Since the prototype in this work is not able to detect pitch and roll movement of the measurement platform, only height deviation was compensated. Any future iterations of the surface measurement system will feature three-dimensional tracking, allowing for correction of height, tilt, and roll movements.

In order to improve the performance of the prototype, a detailed characterization of its system components was carried out. Seismic and electronic noise were measured at several points in the setup. An investigation into geometric anti-spring (GAS) filters shows that it is possible to attenuate seismic vibrations by at least 20 dB across the frequency spectrum relevant for the operation of the surface measurement device. Additionally, the sensitivity of the position tracking system with regard to different optical configurations was analyzed.

Using these findings, design recommendations for the upcoming iteration of the surface measurement device were formulated. This will facilitate reaching the accuracy goal of 10 nm for topology measurements. In the case of measuring steps between adjacent mirrors, the prototype is already capable of delivering 18 nm accuracy. This is at least one order of magnitude better than the manual measurement method that was used so far. The interferometric measurement device is shown capable of measuring the oscillations of a mirror surface at a frequency of 1000 Hz. On top of that, the design allows for theoretically unlimited extension of the linear rail while the laser reference maintains an absolute coordinate system. This can be used to obtain surface scans of much larger SUTs.

Overall, the prototype described in this work represents a first step toward increasing the precision of the *q*BOUNCE measurements. Another iteration of the surface measurement device, with consideration to the findings in this work, is already under construction, and will significantly improve position-hold performance through the use of high-performance noise isolation, temperature compensation, and a revised hardware design.

Die approbierte gedruckte Originalversion dieser Diplomarbeit ist an der TU Wien Bibliothek verfügbar
The approved original version of this thesis is available in print at TU Wien Bibliothek.
TU Bibliothek Your knowledge hub WIEN

x_1	x_2	Δx_1^{DS}	Δx_2^{DS}	$\Delta x_1^{\mathrm{SIOS_I}}$	$\Delta x_2^{\mathrm{SIOS_{II,III}}}$
60 mm	const.	+7 mm	+33 mm	−21 mm	+25 mm

Table 5: *Measurements that allow the correction data acquired with the laser reference to be translated to other sensor configurations. For an overview of sensor positions, see figure 35.*

A Measuring Tilt and Offset of the Linear Stage Using Two Mirror Positions

When using the surface-under-test (SUT) as an (assumed flat) plane of reference, information about its absolute shape is lost. Consequently, the corrected curves can only be interpreted as relative coordinates to the calibration curve. This can be overcome by using the laser beam as a plane of reference.

Upon cursory testing, the quadrant sensor (quad.sens.) has a detection range much larger than what is needed for operation of the position-hold feedback – about 700 µm. The idea is to use the quad.sens. to record the Z-deflection of the linear stage by turning off the height compensation of the piezo actuator.

Essentially, the procedure is equivalent to what is discussed in section 4.2. Important geometry and variables are described in figure 31. After proper calibration of the quad.sens. (see section 3.3.1), the piezo table is set to a fixed position ("servo mode") in an effort to eliminate any additional variables. Next, the deflection seen on the Y-axis of the quadrant sensor $z_i(x)$ is acquired at multiple positions along the linear stage and converted to µm. This step is repeated for two different mounting points of the concave reflector. The position called "mirror-back" is the usual position of the reflector, while "mirror-front" is shifted 60 mm toward the positive direction of the translator stage (see figure 35). The difference of the two measurements is then used to determine height offset $\Delta z(x)$ and tilt $\alpha(x)$ for all recorded positions x on the linear rail.

The length x_1 describes the fixed distance between the two mirror mounting points, while x_2 refers to the distance between the hindmost mounting point and the axis of rotation of the gantry. Equations 18 can be solved as shown in equations 19.

In order to apply the correction to SIOS or DeltaSens raw data, the coordinate shift described in equation 20c must be applied. The required set of variables is listed in table 5.

The calibration of the quad.sens. needs to be done separately for each position of the concave mirror. A value of $7\,\mathrm{mV\,\mu m^{-1}}$ was recorded for sensitivity in the "mirror-back" position, while in the "mirror-front" position sensitivity amounted to $-3.1\,\mathrm{mV\,\mu m^{-1}}$. The sign change is due to the detector being within the focal point of the concave reflector.

In practice, the method of measuring tilt and offset in the linear stage based on repositioning the concave mirror did not work out as expected:

- Solving the system of equations (18) requires that there is no change in the height offset or tilt of either laser or reflector. This condition was not met when the concave mirror was moved between its two positions. It would be necessary to have a precise mechanical keying system in order to avoid user

Die approbierte gedruckte Originalversion dieser Diplomarbeit ist an der TU Wien Bibliothek verfügbar
The approved original version of this thesis is available in print at TU Wien Bibliothek.
TU Bibliothek Your knowledge hub WIEN

error when re-attaching the mirror holder.

- Moving the mirror towards the laser while keeping the reflector tilt the same requires re-positioning of the quad.sens.. As the Z-plane of the sensor is required to be the same in both measurements, this was an additional point of failure.

- The positioning of the reference laser is delicately tuned to keep the light beam within the measurement range of the quad.sens.. Changing the position of the concave mirror would require realignment. Without it, only a portion of the range of the translator stage is available for measuring correction data, as the laser beam wanders out of the detector range when the measurement sled is moved.

As a result, while the raw data itself represents valid measurements, no usable correction can be derived since the two measurements do not have the same reference system.

Figure 42 shows that the laser reference was adjusted for the position "mirror-front". After changing the mirror position to "mirror-back" without changing the laser alignment, the reference beam drifts across the range at a steep rate. This immediately reduces coverage for the correction data to 92 to 216 mm.

The tilt and offset corrections (see figures 43 and 44) derived from these two measurements produce results that are off-the-chart in terms of the compensation capability of the piezo stage. In comparison with the correction measurement made with the DeltaSens (see section 4.2), tilt and offset figures appear to be two orders of magnitude too large.

The most substantial argument against the validity of these data is provided by the fact that, during initial testing, the feedback mechanism never reported an out-of-range condition while using the full range of the translator stage. This inevitably points toward a measurement error in the raw data shown in figure 42.

Measuring the linear stage tilt/offset using the laser reference promises to provide information about tilt and offset of the rail carrier independently from any mechanical reference surface. However, the technological hurdles described in this section will require further technological improvements. Alternatively, the problem of capturing a reference line can be avoided altogether through the use of a multi-axis positional feedback system.

Die approbierte gedruckte Originalversion dieser Diplomarbeit ist an der TU Wien Bibliothek verfügbar
The approved original version of this thesis is available in print at TU Wien Bibliothek.
TU Bibliothek Your knowledge hub WIEN

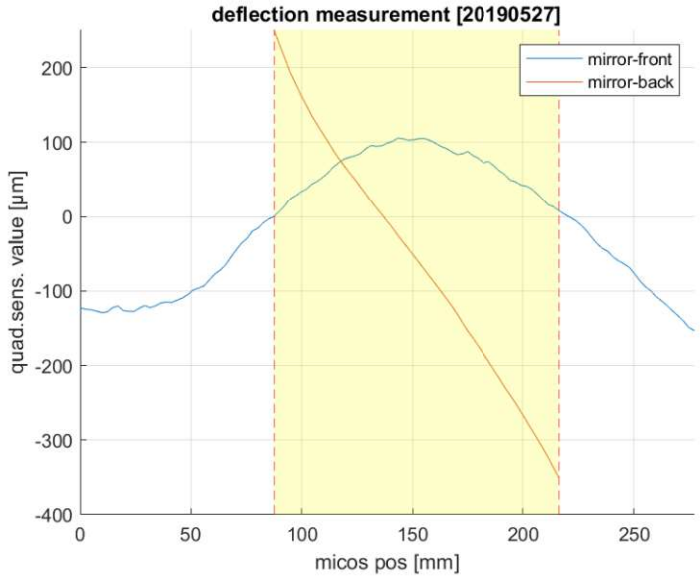

Figure 42: *Result of the tilt/offset correction measurement based on the concave mirror. The correctable range (yellow area) is limited to* 92 *to* 216 mm*, where "mirror-back" exceeds the quad.sens. range.*

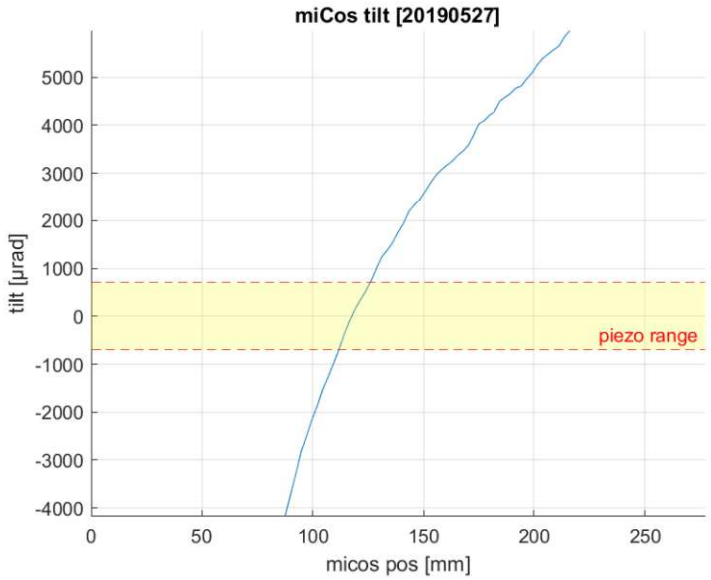

Figure 43: *Localized tilts of the linear stage ("miCos"). The tilts derived from figure 42 with equations 19 are on the order of* 9 mrad *and greatly exceed the range available for correction (yellow area).*

Die approbierte gedruckte Originalversion dieser Diplomarbeit ist an der TU Wien Bibliothek verfügbar
The approved original version of this thesis is available in print at TU Wien Bibliothek.
TU Bibliothek Your knowledge hub WIEN

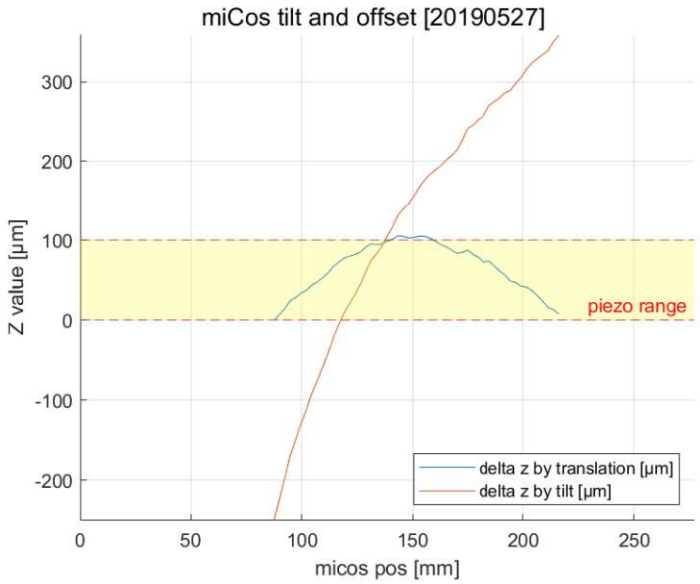

Figure 44: *Localized offset of the linear stage ("miCos"). These offsets are derived from the tilt data in figure 43 together with equations 19. The Z-offset introduced by the linear rail (blue) is is in the range of* 117 µm. *The red line shows tilts converted into the erroneous Z-offset seen by the feedback mechanism. Both curves exceed the compensation range available via the piezo actuator.*

Die approbierte gedruckte Originalversion dieser Diplomarbeit ist an der TU Wien Bibliothek verfügbar
The approved original version of this thesis is available in print at TU Wien Bibliothek.

References

[1] H. Abele et al. "QuBounce: The Dynamics of Ultra-Cold Neutrons Falling in the Gravity Potential of the Earth". In: *Nucl. Phys. A*. PANIC08 827.1 (Aug. 2009), pp. 593c–595c. ISSN: 0375-9474. DOI: 10.1016/j.nuclphysa.2009.05.131.

[2] H. Abele et al. "Ramsey's Method of Separated Oscillating Fields and Its Application to Gravitationally Induced Quantum Phase Shifts". In: *Phys. Rev. D* 81.6 (Mar. 2010), p. 065019. DOI: 10.1103/PhysRevD.81.065019.

[3] Mark G. Beker. "Low-Frequency Sensitivity of next Generation Gravitational Wave Detectors". PhD thesis. Vrije U., Amsterdam, 2013.

[4] A. Bertolini et al. "Seismic Noise Filters, Vertical Resonance Frequency Reduction with Geometric Anti-Springs: A Feasibility Study". In: *Nucl. Inst. Meth. Phys. Res.* A 435 (1999), p. 475. DOI: 10.1016/S0168-9002(99)00554-9.

[5] Blom and (Astro)-Particles Physics. "Seismic Attenuation for Advanced Virgo: Vibration Isolation for the External Injection Bench". EN. PhD thesis. Dec. 2015.

[6] J. H. Burge et al. "Optical Surface Measurements for Very Large Flat Mirrors". In: *SPIE Astronomical Telescopes + Instrumentation*. Ed. by Eli Atad-Ettedgui and Dietrich Lemke. Marseille, France, July 2008, p. 701817. DOI: 10.1117/12.790048.

[7] Gunther Cronenberg. "Frequency Measurements Testing Newton's Gravity Law with the Rabi-qBounce Experiment". Doctoral Thesis. Vienna, Austria: TU Wien, Feb. 2016.

[8] Gunther Cronenberg et al. "Acoustic Rabi Oscillations between Gravitational Quantum States and Impact on Symmetron Dark Energy". en. In: *Nature Physics* 14.10 (Oct. 2018), pp. 1022–1026. ISSN: 1745-2481. DOI: 10.1038/s41567-018-0205-x.

[9] Wolfgang Demtröder. *Experimentalphysik 1: Mechanik und Wärme*. ger. 6th ed. Springer-Lehrbuch. Berlin, Heidelberg: Springer, 2013. ISBN: 978-3-642-25466-6.

[10] Nico Einsidler. "Vibration Studies for the qBounce Experimental Platform". Bachelor Thesis. Vienna, Austria: TU Wien, July 2017.

[11] Paul Feichtinger. "Analyse der Stufenkontrolle des qBounce Experiments". ger. Bachelor Thesis. Vienna, Austria: TU Wien, Feb. 2018.

[12] SIOS Meßtechnik GmbH. *Dreistrahl-Interferometer Mit Planspiegelreflektor, Serie SP 120/2000 TR — Anwenderdokumentation*. Apr. 2012.

[13] Werner Hesse. *Aluminium-Werkstoff-Datenblätter: = Aluminium material data sheets*. ger;eng. 7. Auflage. Beuth Wissen. Berlin Wien Zürich: Beuth Verlag GmbH, 2016. ISBN: 978-3-410-26875-8.

[14] Zurich Instruments. *Principles of Lock-in Detection and the State of the Art*. https://www.zhinst.com/europe/resources/principles-of-lock-in-detection. Nov. 2016.

Die approbierte gedruckte Originalversion dieser Diplomarbeit ist an der TU Wien Bibliothek verfügbar
The approved original version of this thesis is available in print at TU Wien Bibliothek.
TU Bibliothek Your knowledge hub WIEN

[15] T. Jenke et al. “Gravity Resonance Spectroscopy Constrains Dark Energy and Dark Matter Scenarios”. In: *Phys. Rev. Lett.* 112.15 (Apr. 2014), p. 151105. DOI: 10.1103/PhysRevLett.112.151105.

[16] Carina Killian. “Analysis and Correction of the qBounce Step Control System”. Project Thesis. Vienna, Austria: TU Wien, 2019.

[17] Bastian L. Lindl and Frank Kemnitzer. “High Accurate Metrology on Large Surface Areas with Low Reflectivity”. In: *The 11th International Symposium Of Measurement Technology And Intelligent Instruments*. cyberTECHNOLOGIES GmbH, July 2013.

[18] Tobias Lins. “Quantenzustände im Gravitationsfeld der Erde”. ger. Master Thesis. Munich, Germany: TU München, Jan. 2011.

[19] Proteep C. V. Mallik et al. “Measurement of a 2-Meter Flat Using a Pentaprism Scanning System”. In: *Optical Manufacturing and Testing VI*. Vol. 5869. International Society for Optics and Photonics, Aug. 2005, 58691A. DOI: 10.1117/12.618468.

[20] Jakob Micko. *Eckdaten zu qBounce*. private communication. Aug. 2021. URL: micko@ill.eu.

[21] Vito Pecile. “Analysis and Correction of the qBounce Step Control System”. Project Thesis. Vienna, Austria: TU Wien, 2019.

[22] J. Peterson. “Observations and Modeling of Seismic Background Noise”. In: *U.S. Dept. Int. Geol. Surv., Open-File Rept.* 93-322 (1993).

[23] Norman F. Ramsey. “A Molecular Beam Resonance Method with Separated Oscillating Fields”. In: *Physical Review* 78.6 (1950), p. 695.

[24] Tobias Rechberger. “Ramsey Spectroscopy of Gravitationally Bound Quantum States of Ultracold Neutrons”. PhD Thesis. Vienna: TU Wien, 2018.

[25] M. S. Safronova et al. “Search for New Physics with Atoms and Molecules”. In: *Rev. Mod. Phys.* 90.2 (June 2018), p. 025008. DOI: 10.1103/RevModPhys.90.025008.

[26] Patrick Schmidt. “Studien zur Ramsey-Spektroskopie ultrakalter Neutronen im Rahmen des qBounce Experiments”. ger. Master Thesis. Vienna, Austria: TU Wien, Feb. 2017.

[27] David L. Shealy and Shao-Hua Chao. “Design and Analysis of an Elliptical Gaussian Laser Beam Shaping System”. In: *Laser Beam Shaping II*. Vol. 4443. International Society for Optics and Photonics, Oct. 2001, pp. 24–35. DOI: 10.1117/12.446751.

[28] M. Shinagawa et al. “Jitter Analysis of High-Speed Sampling Systems”. In: *IEEE Journal of Solid-State Circuits* 25.1 (Feb. 1990), pp. 220–224. ISSN: 1558-173X. DOI: 10.1109/4.50307.

Die approbierte gedruckte Originalversion dieser Diplomarbeit ist an der TU Wien Bibliothek verfügbar
The approved original version of this thesis is available in print at TU Wien Bibliothek.
TU Bibliothek Your knowledge hub WIEN